Gas-Phase Structural Analysis of Sulfated Glycans

Inaugural-Dissertation

to obtain the academic degree

Doctor rerum naturalium (Dr. rer. nat.)

submitted to the Department of Biology, Chemistry, Pharmacy

of Freie Universität Berlin

by

Łukasz Polewski

2024

I

This work was performed at the Freie Universität Berlin and the Fritz-Haber-Institute of the Max-Planck-Gesellschaft in Berlin from December 2019 to June 2024 under the supervision of Prof. Dr. Kevin Pagel.

1st reviewer: Prof. Dr. Kevin Pagel

2nd reviewer: Prof. Dr. Christoph A. Schalley

Date of defence: 10.10.2024

Statutory Declaration

I hereby declare that I alone am responsible for the content of my doctoral dissertation and that I have only used the sources or references cited in the dissertation.

Berlin, July 01, 2024 Łukasz Polewski

Abstract

Glycans are essential biomolecules in all living organisms. Most often, functionalising the surface of proteins ensuring their activity or bound to cell surfaces acting in cell recognition, adhesion, and microbial pathogenesis. Of special interest are the often-heavy sulfated glycans found in the extracellular matrix, the glycosaminoglycans. They are the first cellular contact point for many viruses or bacteria, but also therapeutical components and serum proteins. The selective binding of such diverse structures requires a diverse structure itself. This is reflected by the tremendous number of isomeric structures found in glycosaminoglycans. The challenges faced in the analysis of sulfated glycans diver substantially from classical glycan analysis, especially for mass spectrometry-based approaches which already struggle to retain sulfate groups.

This work investigates the use of ion mobility spectrometry and gas-phase infrared spectroscopy in combination with mass spectrometry for the structural analysis of isomeric sulfated glycans. Both methods have been successfully applied for the analysis of glycans before. Ion mobility spectrometry offers a structural dimension, missing in classical mass spectrometry for the differentiation of isomeric structures, while infrared spectroscopy can provide detailed structural information of even gas-phase conformations. These methods allowed for the investigation of the interaction of glycosaminoglycan with magnetic resonance imaging probes, revealing an intricate binding motive and a surprising dissociation behaviour. They allowed for the separation and quantification of twelve partially isomeric sulfated disaccharides, which previously were analyzed by tedious and time-consuming liquid chromatography methods. And finally, they revealed two unknown sulfated glycan-specific gas-phase rearrangement processes, which further consolidate the unique challenges faced in the structural analysis of sulfated glycans.

I Zusammenfassung

Glykane sind essenzielle Biomoleküle in allen lebenden Organismen. Meist funktionalisieren sie die Oberfläche von Proteinen, um deren Aktivität zu gewährleisten, oder sie sind an Zelloberflächen gebunden und spielen eine Rolle bei der Zellerkennung, der Adhäsion und der mikrobiellen Pathogenese. Von besonderem Interesse sind die oft schwer sulfatierten Glykane, die in der extrazellulären Matrix vorkommen, die Glykosaminoglykane. Sie sind die erste zelluläre Kontaktstelle für viele Viren oder Bakterien, aber auch für therapeutische Wirkstoffe und Serumproteine. Die selektive Bindung so vielfältiger Strukturen erfordert selbst eine vielfältige Struktur. Dies spiegelt sich in der enormen Anzahl von isomeren Strukturen wider, die in Glykosaminoglykanen zu finden sind. Die Herausforderungen bei der Analyse sulfatierter Glykane unterscheiden sich erheblich von der klassischen Glykananalyse, insbesondere bei massenspektrometriebasierten Ansätzen, die bereits Schwierigkeiten haben, die Sulfatgruppen zu erhalten.

In dieser Arbeit wird der Einsatz der Ionenmobilitätsspektrometrie und der Gasphasen-Infrarotspektroskopie in Kombination mit der Massenspektrometrie für die Strukturanalyse isomerer sulfatierter Glykane untersucht. Beide Methoden wurden bereits erfolgreich für die Analyse von Glykanen eingesetzt. Die Ionenmobilitätsspektrometrie bietet eine strukturelle Dimension, die in der klassischen Massenspektrometrie zur Unterscheidung isomerer Strukturen fehlt, während die Infrarotspektroskopie detaillierte strukturelle Informationen selbst über Gasphasenkonformationen liefern kann. Diese Methoden ermöglichten die Untersuchung der Wechselwirkung von Glykosaminoglykanen mit Sonden für die Magnetresonanztomographie, wobei ein kompliziertes Bindungsmotiv und ein überraschendes Dissoziationsverhalten festgestellt werden konnten. Sie ermöglichten die Trennung und Quantifizierung von zwölf teilweise isomeren sulfatierten Disacchariden, die zuvor mit mühsamen und zeitaufwendigen Flüssigchromatographiemethoden analysiert wurden. Und schließlich deckten sie zwei unbekannte sulfatierte Glykan-spezifische Gasphasen-Umlagerungsprozesse auf, die die einzigartigen Herausforderungen bei der Strukturanalyse von sulfatierten Glykanen weiter festigen.

I Abbreviations

ATD	Arrival time distribution
CCS	Collision cross-section
CID	Collision-induced dissociation
CS	Chondroitin sulfate
DS	Dermatan sulfate
DT-IMS	Drift tube-ion mobility spectrometry
EDD	Electron detachment dissociation
ESI	Electrospray ionization
FEL	Free electron laser
FHI	Fritz Haber Institute
FLD	Fluorescence detection
FPX	Fondaparinux
FTICR	Fourier-transform ion cyclotron resonance
GAG	Glycosaminoglycan
GalNAc6S	*N*-Acetyl-*D*-galactosamine 6-sulfate
GlcNAc3S	*N*-Acetyl-*D*-glucosamine 3-sulfate
GlcNAc4S	*N*-Acetyl-*D*-glucosamine 4-sulfate
GlcNAc6S	*N*-Acetyl-*D*-glucosamine 6-sulfate
HA	Hyaluronic acid
HS	Heparan sulfate
IM-MS	Ion mobility-mass spectrometry
IMS	Ion mobility spectrometry
IR	Infrared
IRMPD	Infrared multiple photon dissociation

ITC	Isothermal titration calorimetry
IVR	Intramolecular vibrational redistribution
LC	Liquide chromatography
MRI	Magnetic resonance imaging
MS	Mass spectrometry
MS/MS	Tandem mass spectrometry
m/*z*	Mass-to-charge
nESI	Nano electrospray ionization
NETD	Negative electron transfer dissociation
OPA	Optical parametric amplifier
OPO	Optical parametric oscillator
PAPS	3′-Phosphoadenosine-5′-phosphosulfate
PETG	Polyethylene terephthalate glycol
ProA	Procainamide
RF	Radiofrequency
RNA	Ribonucleic acid
SNFG	Symbol nomenclature for glycans
TIM-MS	Trapped ion mobility-mass spectrometry
TIMS	Trapped ion mobility spectrometry
TOF	Time of flight
TW-IMS	Traveling wave-ion mobility spectrometry
UV	Ultraviolet
UVPD	Ultraviolet photodissociation

Amino acids and monosaccharides are abbreviated by the common three-letter codes not further disclosed here.

Table of Content

1 | Introduction and Motivation

In recent years, glycan analysis developed tremendously with many methods finding their way into mainstream analysis. Especially with the rise of glycans in vaccine research, interest in their analysis spiked. Meanwhile, the translation of the techniques to the field of sulfated glycans is only slowly progressing; why is that?

Glycans are tremendously complex molecules. In contrast to other biopolymers, like peptides or nucleic acids, they are not strictly linear. Moreover, their convoluted biosynthetic pathways can make initial structural estimates unfeasible. Their structural analysis has troubled analytical scientists for decades. The sulfation of these glycan structures, which is a common occurrence, adds an additional layer of complexity to their analysis, which must be resolved. In principle, nuclear magnetic resonance techniques can resolve both the structure of glycans and the sulfation site,[1, 2] but they require large sample quantities, which are usually not present in extracts of natural materials. Mass spectrometry (MS) can measure samples in the femtomole range,[3, 4] but struggles with the differentiation of isomeric structures.

Hyphenation of MS to pre-ionization techniques such as liquid chromatography (LC) can solve this issue. While especially hydrophilic interaction and porous graphitic carbon chromatography are very successful in the separation of glycans, they struggle with reasonable separation for medium- to highly-sulfated glycans. Strong anion exchange chromatography, on the other hand, excels in the separation of heavily sulfated species, but due to the high salt content required in the eluent, it is not compatible with MS approaches.

Post-ionization techniques could help with the structural analysis of these sulfated glycans. Ion mobility spectrometry (IMS) already showed its ability to separate isomeric glycans in the gas phase.[5-7] In a similar manner, gas-phase infrared (IR) spectroscopy can distinguish between glycan isomers.[8, 9] The potential of both methods to advance sulfated glycan analysis

is tremendous and largely unexplored. Therefore, this thesis aims to improve and explore the structural analysis of sulfated glycans by the use of these sophisticated methods.

The fundamentals of the here-analyzed biomolecules, the applied methods, and backgrounds to existing sulfated glycan analytical workflows are introduced in **Chapter 2**, followed by a detailed description of the utilized mass spectrometers in **Chapter 3**. **Chapter 4** explores the interaction of sulfated glycans with a commonly applied pharmaceutical compound in magnetic resonance imaging. **Chapter 5** then shows how a widely employed sulfated glycan analytical method can be replaced by a considerably faster, purely gas-phase method. Finally, **Chapter 6** investigates specific rearrangement processes of sulfated glycans in the gas phase. The thesis then concludes in **Chapter 7** with an outlook and summary.

2| Fundamentals

This chapter provides basic fundamental knowledge about both the studied class of biomolecules and the applied methods to do so. It first starts with an introduction to glycans, their isomerisms and the therefore emerging complexity. It introduces their diversity, to go then deeper into the glycan class of the glycosaminoglycans. The second section gives insight into ion mobility spectrometry and describes the different approaches with their respective advantages and disadvantages. Afterwards, action spectroscopy will be discussed in a similar manner. The last section of this chapter then highlights the difficulties of gas-phase glycosaminoglycan analysis and how ion activation and the previously introduced methods have already been applied to study this complex field of glycosaminoglycomics.

2.1 Glycans – Structure, Complexity, and Diversity

Sugars, also known as glycans, saccharides or carbohydrates have often been painted as the evildoer in the public eye with many product lines offering "sugar-reduced" or even "sugar-free" alternatives. These alternatives often simply substitute one sugar for another, e.g. sorbitol or sucralose, and are therefore strictly speaking never really "sugar-free".[10] These days, we realize that sugars are much more than energy carriers. The biomolecular class of glycans, the glycome, is highly diverse and includes a tremendous number of structures, which fulfil equally diverse roles in all living organisms.[11] Glycans are often found as glycoconjugates attached to proteins to form glycoproteins or attached to lipids forming glycolipids.[12] As the names suggest, glycans are often seen as the minor partner in these conjugates but nevertheless fulfil an equally important role in ensuring a proper function, with many enzymes showing little to no activity if not properly glycosylated. At the same time, glycans act as immunoactive species with many surface proteins of viruses being heavily glycosylated.[13-15] The Human Immunodeficiency Virus is enveloped by the gp120 spike proteins with *N*-linked glycans compromising half of the protein mass.[16] The glycosylation of the cell surface also heavily impacts viral binding.[17-20] The cell infection by Herpes Simplex Virus 1 is known to be initiated by the binding of heparan sulfate (HS) proteoglycans to the virus.[21, 22] Removal of the heparan sulfate from the cell surface renders the cell immune to infection.

In contrast to other biomolecules, such as proteins or ribonucleic acid (RNA), the synthesis of glycans is not template-based, there is no direct "code" that defines the structure of any given glycan.[23] Nevertheless, glycans show specific structural motifs. The biosynthetic pathway of glycans can be compared to a more dynamic version of an assembly line in a factory. With iterative additions or modifications of saccharides to a variety of glycan core structures, with the quantity and quality of the performed modifications being environment-dependent. The resulting complexity of structures and common classifications of glycans will be described in the following section.

2.1.1 Glycan Isomerism

The complexity of the glycome already starts at its smallest member, the monosaccharide.[24] Monosaccharides are grouped by the number of carbon atoms they contain (trioses, tetroses, pentoses, hexoses etc.). These structures can be further divided by their functional groups, most notably aldoses for aldehyde-containing saccharides, ketoses for the ketones and alditols for reduced sugar alcohols. The carbon atoms along a monosaccharide chain are numbered to discuss structural differences between glycans more easily, as seen in the top left of Figure 2.1. The first primary carbon atom nearest to the functional group carries the number one, subsequent carbon atoms along the chain are numbered accordingly.

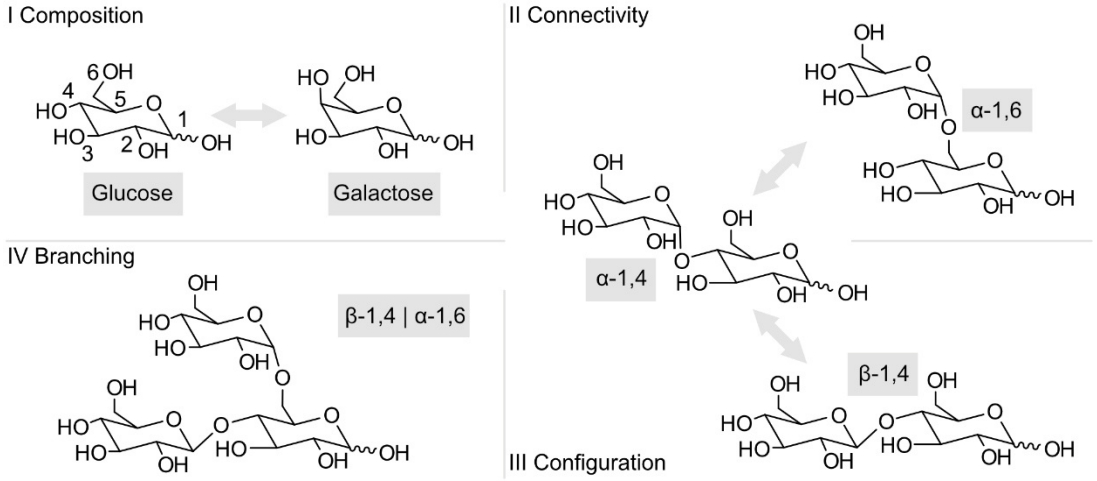

Figure 2.1: The different forms of isomerism commonly encountered in glycans. Composition, connectivity, configuration, and branching.

The isomerism in glycans can be reduced to four aspects of complexity (Figure 2.1).[5, 7] The first form are the compositional isomers. Glucose and galactose for example are isomeric to each other, differing only in the stereocenter on C4. Enantiomeric sugars carry the same name but are differentiated by a prefix, *D* or *L*. This prefix is often left out since most natural sugars exclusively occur as *D*- or *L*-sugars. Modification of sugars such as sulfation also play into the compositional isomers, e.g. *6O*-, or *4O*-sulfated glucose. When glycans are connected to each other to form polysaccharides they can differ in the position on which the glycosidic linkage is formed, their connectivity. The polysaccharides starch and dextran are for example

composed of 1,4 or 1,6 connected glucose monosaccharides respectively. Additionally, configurational isomers are present in polysaccharides due to the dynamic nature of the configuration of the functional group carrying carbon, the anomeric centre (Figure 2.2). Glycans usually occur as heterocycles but also exist in an open-chain form to a minor degree. Through a reversible hemiacetal formation, the heterocycle is formed which leads to the anomericity. The configuration of the anomeric centre is given by the prefixes α and β which depend on the relative configuration of the anomeric centre to the last stereo centre in the glycan chain. (*R*, *S*) and (*S*, *R*) are α configurations while (*R*, *R*) and (*S*, *S*) are β configurations. The open-chain form of aldohexoses cyclises preferably to a six-membered ring, the pyranose form. But to a small degree the furanose form, a five-membered ring, is also formed.[25]

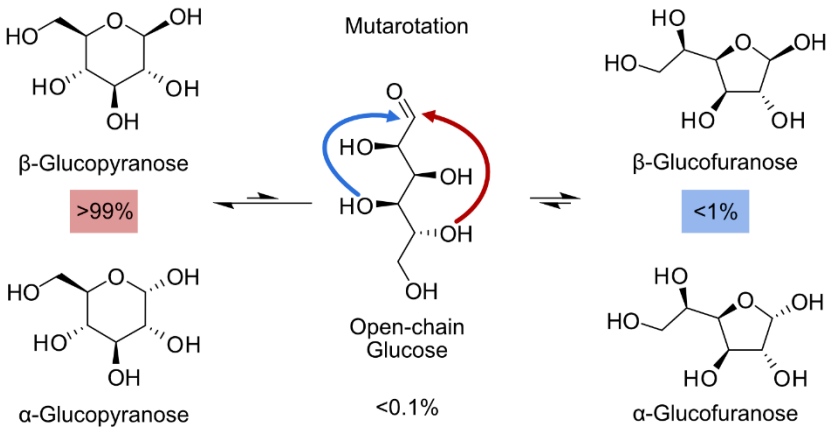

Figure 2.2: Basic principle of mutarotation on the example of glucose. The vast majority of glucose is in equilibrium as the six-membered pyranose-ring with only a fraction existing as open-chain or the five-membered furanose-ring.[25]

The last form of isomerism is the glycan branching. Glycan branching refers to the isomers where additional sugar molecules are attached to a central sugar molecule in a polysaccharide chain, creating a structure that resembles a tree branch in contrast to a simple linear chain.

Due to their intricate chemical structure, glycan structures are often abbreviated by the 'Symbol Nomenclature for Glycans' (SNFG).[26, 27] SNFG allows for a clearer representation of especially larger glycans structures (Figure 2.3a). It replaces monosaccharides with symbols, e.g. hexoses are shown as circles, aminohexoses and their derivatives as rectangles and

carboxylic acid containing monosaccharides as rhombuses. Different colours indicate compositional isomers, e.g. blue for glucose, and yellow for galactose derived glycans. The connectivity is given by the angle of the connection between building blocks while the configuration is represented as either a dotted line for α or a solid line for β bonds. Wavy lines indicate an unknown configuration. An overview of this can be found in Figure 2.3b. Adapted versions of this representation will be found throughout the thesis.

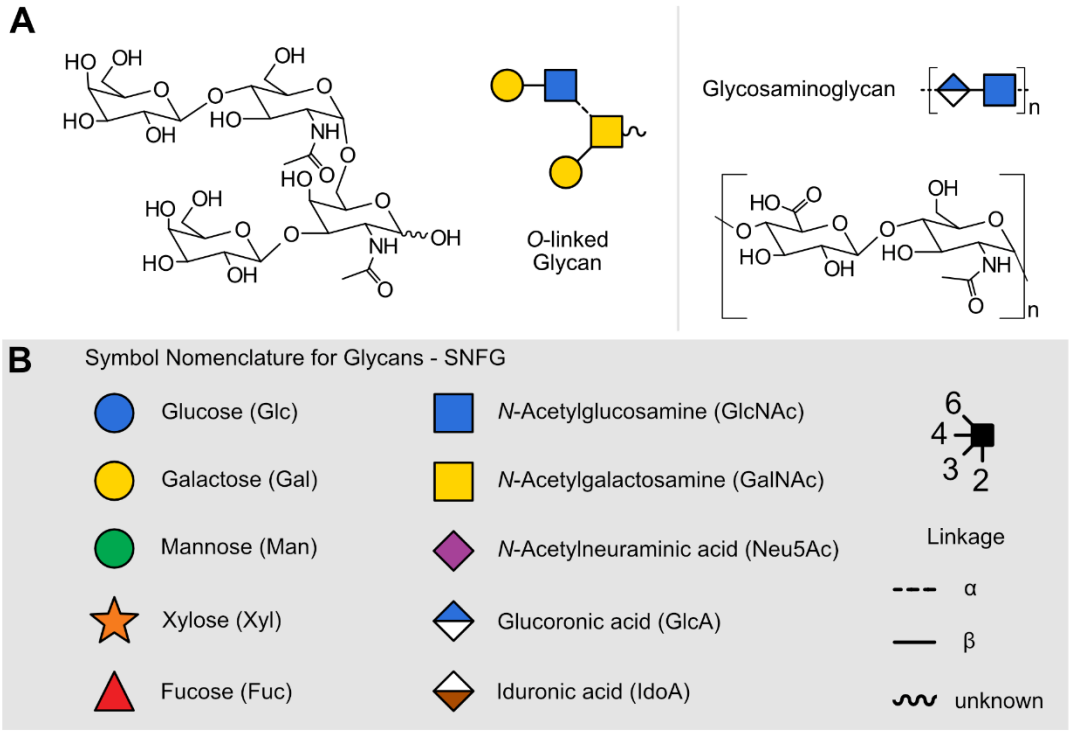

Figure 2.3: Symbol Nomenclature for Glycans (SNFG). **a)** An *O*-linked glycan (left) and a glycosaminoglycan (right) represented as chemical structures and the corresponding SNFG structures. **b)** Overview of different monosaccharide SNFG depictions and the linkage definition.

2.1.2 Glycan Types

The structural complexity of glycans is large, but they can be classified based on the type of biomolecule they are attached to. Glycans can be found attached to lipids as glycolipids[28] or,

controversial, on RNA as GlycoRNA,[29-32] the largest class of glycans is found as posttranslational modification on proteins. These glycosylated proteins are categorized as Glycoproteins.

Glycoproteins contain two major glycosylation types, *N*- and *O*-linked glycans.[33] *N*-Glycans are covalently attached to proteins through an asparagine (Asn) residue, which is bound to the glycan with an *N*-glycosidic bond. The minimal peptide sequence to receive an *N*-glycan is Asn-X-Ser in which X is any amino acid except proline.[34] All *N*-glycans possess a common core structure which is composed of two *N*-acetylglucosamine and three mannose units ($Man_3GlcNAc_2Asn$) with a fixed connectivity and configuration.[35] Depending on further modifications of the core structure the resulting *N*-glycans are categorized into three types, oligomannose, complex, and hybrid *N*-glycans. For the oligomannose type, the core structure is extended with exclusively Man units. In the complex type structures, an initial GlcNAc is present on the antennas of the core structure, which are then further extended. Hybrid *N*-glycans are a combination of both previous structural elements and contain oligomannose and GlcNAc extended antenna.[36] The general biosynthetic pathway for *N*-glycans in eucaryotes involves the synthesis of a $Glc_3Man_9GlcNAc_2$ precursor on the glycoprotein, which is then partly digested by glycosidases to be then built up again by glycosyltransferases.[37]

O-Glycans are also found on protein and are part of mucin glycoproteins, where a high density of *O*-glycans is found.[38, 39] They are covalently attached to either serine (Ser) or threonine (Thr) residues. In contrast to *N*-glycans, they are bound through an *O*-glycosidic bond and do not require a specific peptide sequence to be attached. *O*-Glycans do not share a single common core structure, instead, several core structures have been described. Based on the monosaccharide that is first attached to the protein, seven types of *O*-glycans can be defined: most prominently the *O*-GalNAc linked glycans, present in mucin.[40] *O*-GalNAc type structures alone contain four common and additional four rare core structures. These *O*-GalNAc type core structures are considerably smaller than the *N*-glycan core structure, being composed of two or three monosaccharides with some core structures being isomeric to each other. Each core structure follows a different biosynthetic pathway. Generally, the

common precursor for the biosynthesis of *O*-GalNAc type glycans is a single GalNAc monosaccharide which is then built up by an avalanche of glycosyltransferases.[41, 42]

Both *N*- and especially *O*-glycans are often found modified with sulfate groups.[43] They are introduced through sulfotransferases which use 3′-phosphoadenosine-5′-phosphosulfate (PAPS) to transfer sulfate groups to the glycan.[44] These sulfated glycan structures are known to be involved in a variety of physiological and pathophysiological processes,[45, 46] including the previously introduced binding of the herpes virus by HS. HS belongs to a class of glycans not yet introduced, which will be discussed extensively in the following.

2.1.3 Glycosaminoglycans

A class of *O*-linked glycoproteins that are seen as a separate entity due to their unique features are proteoglycans. Proteoglycans consist of a core protein, which consists of peptide repeats, and one or more covalently attached glycosaminoglycan (GAG) chains.[47, 48] GAGs are linear, acidic polysaccharides that consist of repeating disaccharide units that alternate between a hexuronic acid/galactose and a hexosamine. GAGs are often heavily sulfated and can be, based on their core structures, categorized into six distinct groups: hyaluronic acid (HA), keratan sulfate (KS), chondroitin sulfate (CS), dermatan sulfate (DS), heparin and heparan sulfate (HS).

HA is an outlier between the groups. It is neither covalently bound to a proteoglycan nor is it sulfated. Instead, it forms noncovalent complexes with GAG-carrying proteoglycans leading to huge proteoglycan aggregates.[49] Structurally, it is the simplest GAG, showing heterogeneity only in its size dispersity. HA is built from glucuronic acid and β-1,3 linked *N*-acetylglucosamine. The disaccharides are connected through β-1,4 glycosidic bonds (Figure 2.4a). The synthetic pathway for HA is also very unordinary for GAGs. It is synthesized by a single hyaluronan synthase membrane protein which stepwise adds glucuronic acid and *N*-acetylglucosamine units to the HA chain.[50-52]

KS is attached to proteoglycans through either a *N*- or *O*-glycan core structure.[53-55] It is unique among the GAGs due to the absence of a hexuronic acid in its disaccharide unit (Figure 2.4b). Instead, a galactose is β-1,4 linked to a *N*-acetylglucosamine. The disaccharide units are

connected through β-1,3 glycosidic bonds. KS can carry sulfates at two positions in its repeating sequence, the 6*O*-position at the galactose and the *6O*-position at the *N*-acetylglucosamine. The KS chains are composed of high, low and nonsulfated domains. Biosynthetically, the KS structure is built on existing *N*- or *O*-glycans by stepwise addition of galactose and *N*-acetylglucosamine. The resulting nonsulfated chain is then modified by sulfotransferases.[56]

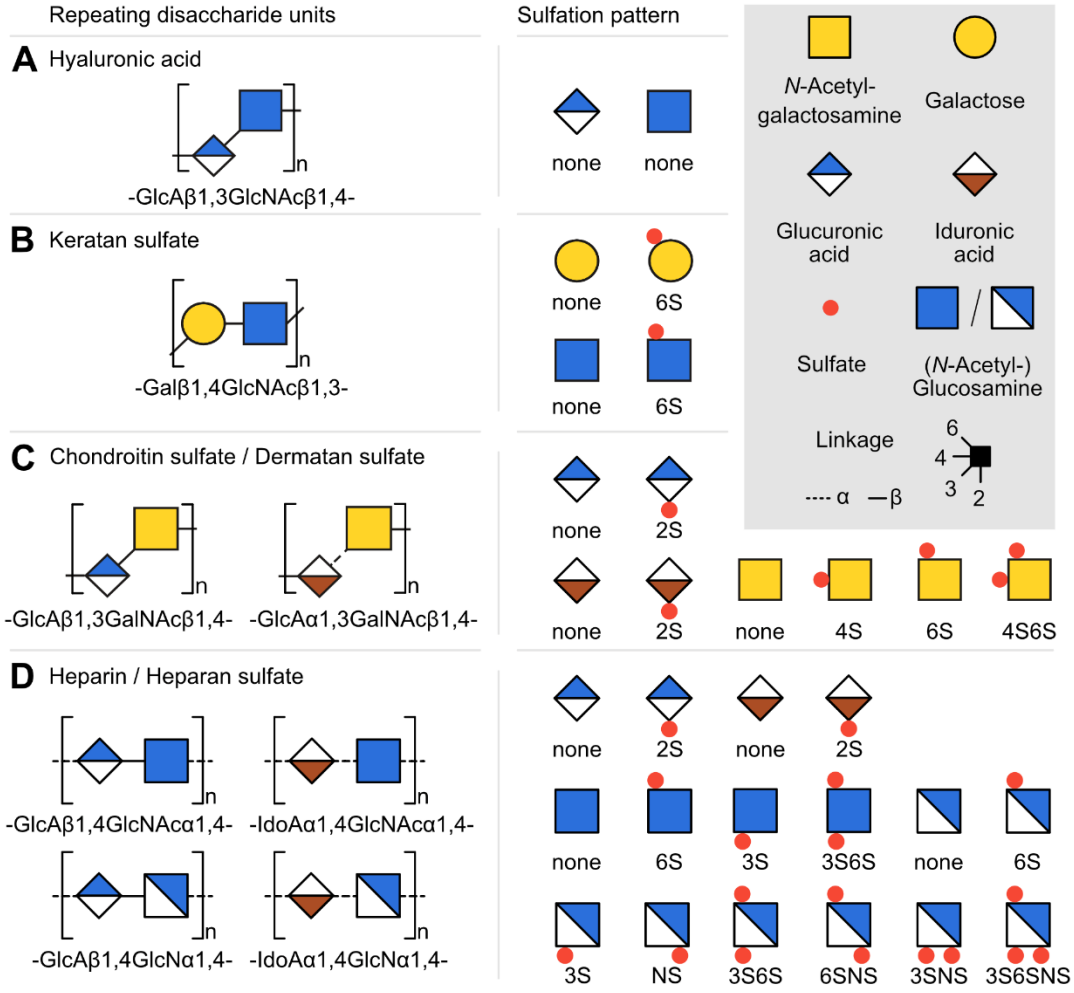

Figure 2.4: An overview of the glycosaminoglycan classification. **a)** Hyaluronic acid (HA), a homogenous and only size disperse glycan. **b)** Keratan sulfate (KS) contains galactose instead of uronic acid. **c)** Chondroitin sulfate (CS) contains glucuronic acid, while dermatan sulfate (DS) contains iduronic acid. **d)** Heparin and heparan sulfate (HS) are the most diverse group of glycosaminoglycans.

CS and DS are structurally and biosynthetically related to each other which is why they are often grouped into one class. CS consist of a glucuronic acid which is β-1,3 linked to an *N*-acetylgalactosamine, the disaccharides are then linked with β-1,4 glycosidic bonds to each other (Figure 2.4c). DS contains *L*-iduronic acid, the C5 epimer of *D*-glucuronic acid. Due to the definition of the glycosidic bond configuration, this formally also changes the bond between the saccharides from a β-1,3 to an α-1,3 bond. CS/ DS can carry sulfate groups at three positions, the *2O*-position of the hexuronic acid and the *4O*- and *6O*-position of the *N*-acetylgalactosamine. As with KS, they are built up with a domain structure consisting of non, low, and highly sulfated domains. CS/DS are connected to the proteoglycan through a linear GlcAGal$_2$Xyl linker which is attached to a serine of the protein core.[57, 58] During biosynthesis in the Golgi apparatus this linker is extended stepwise by addition *N*-acetylgalactosamine and glucuronic acid.[59] For DS the second step involves a C5-epimerase, which flips the C5 configuration of the glucuronic acid which results in the iduronic acid.[60] The last steps consist of a range of sulfotransferases which sulfate the resulting CS/DS chains.[61]

The last but arguably most complex class of GAGs is heparin and HS. The difference between heparin and HS is not of qualitative but quantitative nature. Both are composed of hexuronic acids which are either β-1,4 linked glucuronic acid or α-1,4 linked iduronic acid and both carry β-1,4 linked *N*-acetylglucosamines and glucosamines (Figure 2.4d). Sulfation occurs on the *2O*-position of the hexuronic acid and the *3O*-, *6O*-position of the *N*-acetylglucosamine/glucosamine, additionally, the glucosamine is *N*-sulfated, rarely occurring as a free amine. Heparin/HS utilise the same GlcAGal$_2$Xyl linker present in CS/DS biosynthesis.[62] This linker is extended by iterative addition of *N*-acetylglucosamine and glucuronic acid.[63, 64] The resulting chain is then modified by an *N*-deacetylase/*N*-sulfotransferase which partially cleaves the acetyl groups and replaces them with sulfates. Afterwards, a C5-epimerase produces the iduronic acids and the chain undergoes sulfation by sulfotransferases.[61] Heparin generally undergoes more extensive sulfation during biosynthesis and is mostly consisting of iduronic acid. While HS is produced by virtually all cells, heparin is most notably produced in mast cells.

2.2 Ion Mobility-Mass Spectrometry

While MS alone has proven to be extremely capable of analyzing complex mixtures for a wide range of biological[65-67] and synthetic[68, 69] molecules, it still struggles when dealing with mixtures of isobaric or even isomeric species. Ultra-high resolution mass spectrometers, such as Fourier transform ion cyclotron resonance (FTICR)[70] and high-end Orbitrap mass spectrometers,[71] are capable of separating isobaric species based on the minuscular mass shift due to the mass defect, but isomeric species remain out of reach even for these techniques.

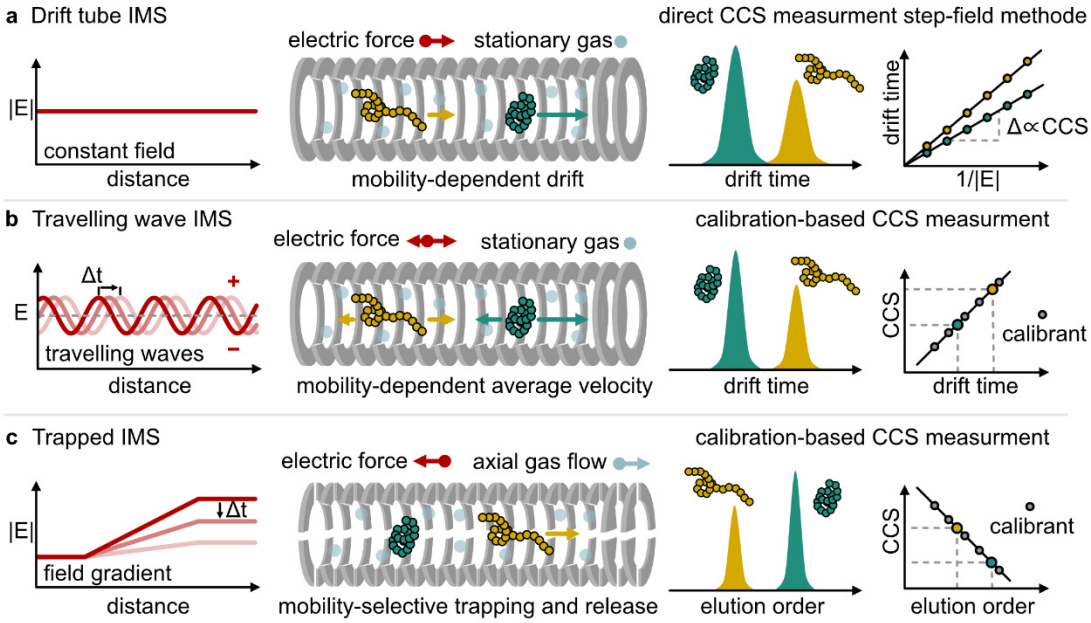

Figure 2.5: Overview of the most common types of ion mobility spectrometry (IMS) and their working principles. **a)** Drift tube IMS uses a linear electric field to drive ions through a gas-filled cell. The resulting drift times can be directly transformed to CCS values using the step-field method. **b)** Travelling wave IMS uses directional travelling electric waves to push ions through the IMS cell. The resulting drift times can be converted to CCS by a calibration procedure. **c)** Trapped IMS utilizes an electric field gradient which acts against the drift direction. Instead, ions are accelerated by an axial gas flow through the IMS cell. Similar as in traveling wave, a calibration procedure is required for CCS extraction.

IMS, often described as an orthogonal technique to MS, fills this gap. IMS separates ions based on their size and shape by colliding them with a neutral buffer gas. Large ions generally experience more collisions and are therefore retained more strongly during the IMS process than small ions. This results in a spatial separation of even isomeric ions. Recently, enantiomers were also successfully separated by an IMS-based technique.[72, 73] Due to the timescale of only a few milliseconds, this technique has excellent compatibility with common types of mass spectrometry and is most commonly found in the research environment in the form of Ion Mobility-Mass Spectrometry (IM-MS).[74]

2.2.1 Drift Tube Ion Mobility

In principle, IMS is an electrophoretic technique that studies how ions under a weak electric field transverse a gas-filled cell with a known path length. In its simplest form, a linear time-independent electric field is applied. This is known as drift tube-ion mobility spectrometry (DT-IMS; Figure 2.5a). First experiments started already in the 19th century performed by Thomson and Rutherford measuring an electric current after applying an electric field to an x-ray-exposed gas-filled tube.[75] Even though DT-IMS is seen as the simplest form of IMS, it also provides the most complete theoretical understanding of the separation principle.

A benefit of DT-IMS compared to other MS-compatible techniques, such as liquid or gas chromatography, is not only the timescale of the experiment but also the ability to directly extract an instrument-independent molecular descriptor, the ion-neutral collision cross section (CCS; Ω). This CCS value can be seen as a rotationally averaged surface area of the measured ion and is usually given in Angstrom square. CCS values can be incorporated into databases giving the ability for a standard free component identification.[76-78] Besides that, there are also several approaches for quantum chemical calculation of CCS values of components with unknown CCS values, omitting the need for even a compound database.[79]

CCS values can be derived from the ion mobility K which in turn is linked to the instrument-dependent drift velocity v_d. The drift velocity of a given compound is described by

equation 2.1, where L is the fixed length of the drift tube while t_d is the average drift time, so the time the ions need to transverse the cell, of the compound.

$$v_d = \frac{L}{t_d} \tag{2.1}$$

The ion mobility K is seen as the electric field E dependent drift velocity v_d of any given compound which is simply described by equation 2.2.

$$K = \frac{v_d}{E} \tag{2.2}$$

Usually, this value is found in databases in the form of the reduced ion mobility K_0, which is the normalized ion mobility K to standard pressure p and temperature T conditions (T_0 = 273.16 K and p_0 = 760 Torr; equation 2.3). This allows for easy comparison between different instrumentations.

$$K_0 = K \cdot \frac{T_0}{T} \cdot \frac{p}{p_0} \tag{2.3}$$

The relation between reduced ion mobility K_0 and the ion-neutral CCS Ω is then described through the Mason-Schamp equation 2.4 for low-field conditions,[80] where μ is the reduced mass of the ion-neutral pair, k_b is the Boltzmann constant, z the charge of the analyte and N the number density of the drift gas.

$$K_0 = \frac{3z}{16N}\sqrt{\frac{2\pi}{\mu \cdot k_b \cdot T}} \cdot \frac{1}{\Omega} \tag{2.4}$$

CCS values in DT-IMS are usually measured through the so-called step-field method. Hereby the drift time of an analyte is measured at several electric field strengths and through the linearized version of equation 2.2 the ion mobility is derived. For correction of the drift time, an additional t_0 time offset is added which simply describes the time from the end of the drift tube to the detector.[81]

$$t_d = \frac{L}{K} \cdot \frac{1}{E} + t_0 \tag{2.5}$$

The effect of alternate drift gases on the ion mobility is not directly obvious from the given equations. Ion mobilities measured in nitrogen are usually considerably larger (>30 %) than when measured with helium. This can be explained by additional long-range dipole

interaction of the drift gas with the ions. Since most of the commonly used drift gases (He, N_2, Ar, SF_6) possess no permanent dipole, the strength of the long-range interactions mostly depends on the polarizability α of the drift gas and the therefore resulting induced dipole through interaction with the charged analyte.[82-84] These dispersion interactions are therefore not very pronounced in the case of helium drift gas (α_{He} = 0.205*10^{-24} cm^3) when compared to diatomic nitrogen (α_{N2} = 1.740*10^{-24} cm^3).[85] Therefore, charge exposure to the drift gas can have tremendous effects on the measured drift time and CCS when measured out of more polarisable drift gasses.

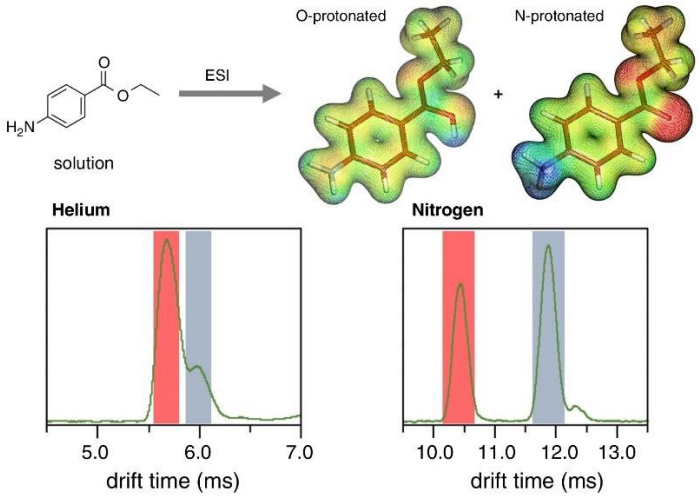

Figure 2.6: Benzocaine and its protomers. The *O*-protonated (red) and *N*-protonated (blue) forms are readily separated when using nitrogen drift gas but show only minor separation in helium. Figure adapted from Gabelica *et al*.[86]

The influence of this effect is particularly evident in the case of benzocaine. Positive electrospray ionization (ESI) of benzocaine leads to the formation of two charge position isomers with the proton attached to either the amine or the carbonyl group. Since the tautomerization of these protomers is kinetically retarded in the gas phase, they can be readily separated by IMS, but only when nitrogen is used as drift gas (Figure 2.6).[87]

2.2.2 Traveling Wave Ion Mobility

Even though DT-IMS instruments started to emerge in the 30s, the commercialization of IM-MS was first achieved in the 21st century. In 2006 Waters introduced the Synapt G1 an IMS-qTOF type instrument.[88-90] But the used ion mobility was not the DT-IMS introduced prior. A major barrier for the use of DT-IMS is a drastically reduced ion transmission efficiency and low duty cycle which results in a drastic loss of MS sensitivity. Only with the introduction of the patent-protected ion funnels developed by the Smith group,[91, 92] a DT-IMS design with a reasonable ion transmission efficiency and duty cycle was achieved.[93] To overcome this issue traveling wave-ion mobility spectrometry (TW-IMS) was developed (Figure 2.5b). TW-IMS utilizes directional travelling voltage waves to pass ions through the IMS cell. During this process the ions experience both pushing and pulling electric forces which increases the total path length that the ions travel through the IMS cell, resulting in increased IMS resolution (Figure 2.7).

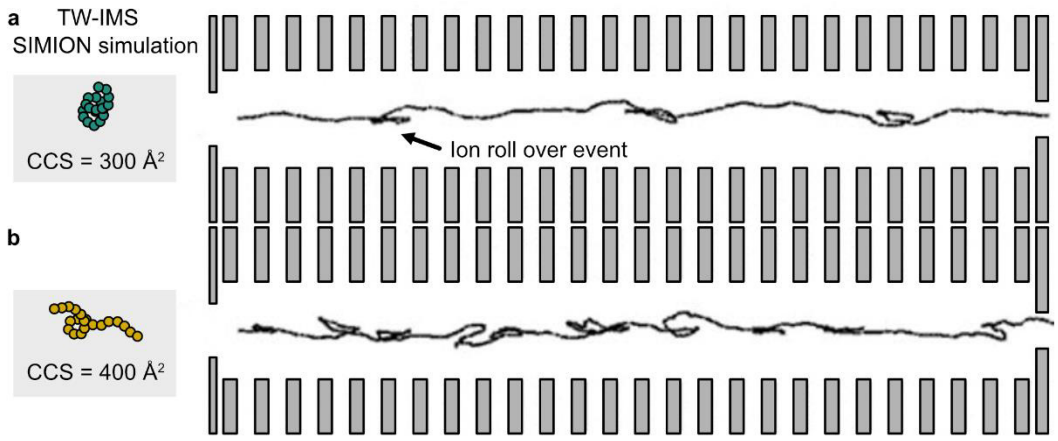

Figure 2.7: Ion trajectories in TW-IMS simulated with SIMION. Through the traveling waves, the ions experience ion roll over events when a voltage wave overtakes the ion cloud. **a)** Ion trajectory of an ion with a CCS of 300 Å² is depicted. **b)** Under the same conditions, the trajectory of an ion with a CCS of 400 Å² is depicted. The larger ion experiences more roll over events resulting in a larger path length. Figure adapted from Giles *et al*.[88]

TW-IMS usually operates at considerably higher electric field strengths and lower pressure to increase the IMS resolution and ion transmission efficiency. With this, a major issue arises.

The ion mobility *K,* described through equation 2.2, is only independent of the electric field strength as long as it is measured under low-field conditions. High-field conditions and the resulting change in ion mobility *K* lead to the breakdown of the Mason-Schamp equation 2.4 since it is derived from the first Chapman-Enskog approximation and the equilibrium Nernst-Einstein relation (equation 2.6) which links the ion mobility to the Brownian motion through the diffusion constant *D*.[80]

$$K = \frac{D \cdot z}{k_b \cdot T} \tag{2.6}$$

However, the equilibrium Nernst-Einstein relation for the ion mobility is only true of vanishing electric fields, so the effect of an electric force on ions is derived from a case where there is no electric field. Strictly, the Mason-Schamp equation is only valid in the absence of an electric field, which is impossible in IMS. Nevertheless, the Mason-Schamp equation is still seen as valid as long as the drift velocity v_d is small compared to the average unidirectional thermal velocity v_T at zero field given by equation 2.7. This is generally true at low-field conditions.

$$v_T = \sqrt{\frac{8k_b \cdot T}{\pi \cdot \mu}} \tag{2.7}$$

At room temperature the low field condition can be defined through equation 2.8 for rigid spheres, where *m* is the ion mass, *M* the mass of the drift gas and N_0 the Loschmidt constant, which is the number density at standard conditions.[94]

$$\frac{E}{N} < \frac{1}{5N_o \cdot K_0}\sqrt{\frac{3k_b \cdot T}{m + M}} \sim 10\ Td \tag{2.8}$$

For atomic ions the low-field limit is in the range of 10^{-20} V*m² or 10 Td;[86] (Townsends; 1 Td = 10^{-21} V*m²) which is considerably lower than the usually in TW-IMS instruments found E/N range of up to ~155 Td.[95]

This issue combined with the time-dependent nature of the electrical field strength makes the direct extraction of CCS values from TW-IMS measurements challenging.[96] CCS values can still be extracted when using a non-direct empirical calibration approach.[97] Hereby, several

ions with known CCS values are measured under the same conditions as the analyte of interest. By simply comparing the drift time of the analyte to the drift time of the calibrants an approximation for the CCS value of the analyte can be made. This approach solves the issue of the time-dependent electric field but the effect of high-field conditions on an analyte is completely dependent on the analyte itself. Similar analytes show a similar change in CCS. Therefore, the effect of the high-field condition on the analyte can be approximated by using calibrants that are similar to the analyte, e.g. glycans are commonly measured in TW-IMS using dextran, a linear size-disperse polysaccharide, as calibrant.[98]

2.2.3 Trapped Ion Mobility

An alternate way of separating ions in the gas phase based on their ion mobility is the trapped ion mobility spectrometry (TIMS).[99] TIMS twists the general approach of IMS by dragging ions through the IMS cell not with an electric field but instead with a constant drift gas flow. The electric field in TIMS acts against the drift gas flow direction (Figure 2.5c). TIMS utilizes a linear electric field gradient which in combination with the gas flow leads to a spatial trapping of the charged analytes along the gradient where the dragging force of the drift gas equals the opposing electric force of the field. By lowering the electric field gradually, the ions elute from the TIMS cell in a size-dependent manner, from larger ions first to smaller last (Figure 2.8a). The high drift gas velocities in the tunnel (~150 m/s) result in ions covering a very high effective path length during the elution that surpasses the physical dimensions of the TIMS tunnel by orders of magnitude. This enables an outstanding resolution in a compact device. Due to the laminar flow effects of the drift gas, the ions need to be radially focused near the centre of the drift channel. Therefore, the stacked lenses, the TIMS cell is constructed of, are split into four parts on which a radio-frequency (RF) is applied (Figure 2.8b).

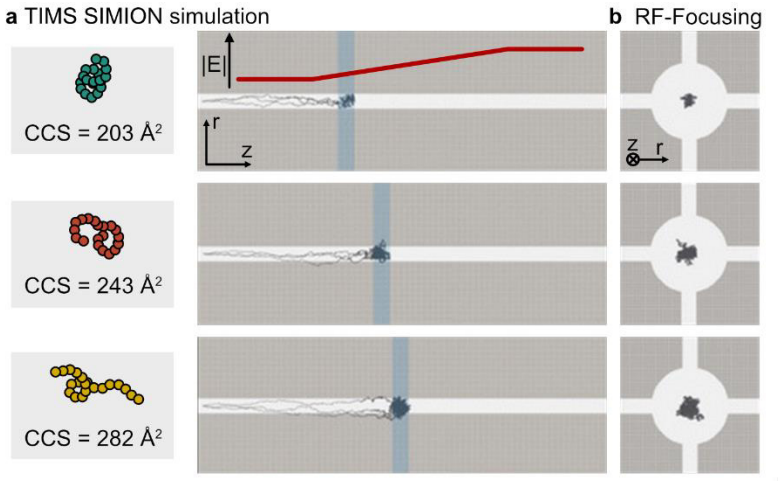

Figure 2.8: Ion trajectories during the trapping stage of TIMS, simulated in SIMION. **a)** Ion trajectories of three calibrant ions, larger ions experience a higher dragging force which spatially separates different sized ions along the electric field gradient. **b)** RF focusing of the ions through the split ion lenses. Figure adapted from Michelmann *et al*.[100]

The strength of this quadrupolar RF-focusing is essential for the achieved resolution. Too low RF-focusing voltages lead to an axial broadening of the trapped ion cloud due to the laminar flow, while too high RF voltages also lead to an axial broadening but instead due to charge repulsion effects in the ion cloud.[101] Besides its effect on resolution, the RF also has a considerable contribution to ion activation during the TIMS process, which lead to a quite vigorous discussion in the field.[102-104]

The question of CCS measurements in TIMS is complicated at best.[105] Several issues are playing into that. First, the strong RF focusing field means the ions are not thermalized in the drift gas, which is usually seen as a prerequisite for low-field conditions.[106] Second, the non-constant pressure, temperature, and axial drift gas velocity along the TIMS cell.[107] And third, during the TIMS process the low-field limit can be overstepped quite significantly reaching up to ~150 Td dependent on the size of the analyte.[107] A calibrations procedure, similar to TW-IMS, can account for these issues and is also applied in TIMS. The chosen calibrant for this procedure is often the Agilent calibration mixture, a common *m*/*z*-calibrant consisting of phosphazenes,[108] which solves the first two issues but ignores the last. Most publication

utilizing TIMS nevertheless use this calibration approach, therefore CCS extracted from TIMS should only be critically compared to CCS from DT-IMS measurements.

2.3 Action Spectroscopy

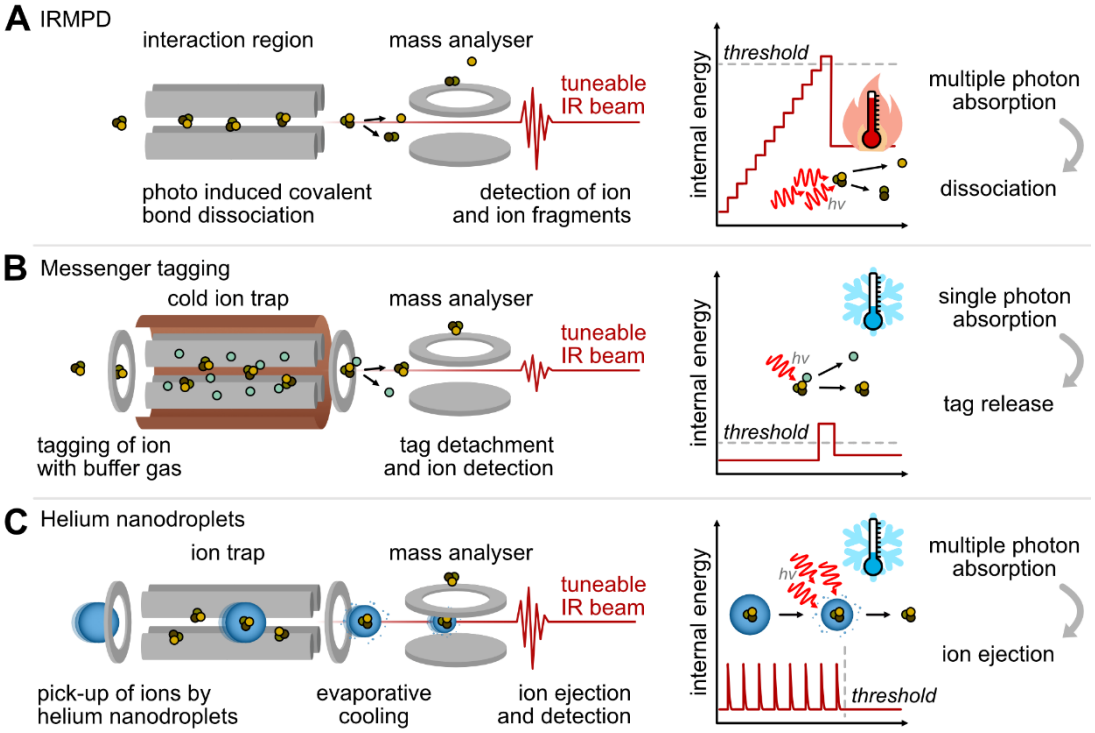

Figure 2.9: Instrumental setup and schematic ion energy diagram comparison of types of infrared (IR) action spectroscopy. **a)** Infrared multiple photon dissociation (IRMPD) spectroscopy. Resonant photons excite the parent ion, and after multiple photon absorptions, the internal energy of the ion reaches a threshold leading to fragmentation and subsequent detection of the fragment ions. **b)** Messenger tagging spectroscopy. Ions form Van der Waals complexes with a tagging gas in a cold ion trap. Irradiation of these complexes by a single resonant photon leads to dissociation of the complex. **c)** Helium nanodroplet spectroscopy. The ions are picked up by helium nanodroplets from an ion trap and cooled to 0.4 K. Resonant photons excite the ion in the droplet. Subsequently, the energy is dissipated to the helium droplet. Evaporative cooling leads to the shrinking of the droplet until the ion is released and detected.

In absorption spectroscopy, the difference between the light intensity before and after the interaction with the analyte is measured. This approach requires a high analyte concentration as is usually the case in solid-state or liquid-phase analysis. In gas-phase ion spectroscopy, the concentration of analytes is too low to directly measure a difference in the light intensity.

The ion density is limited by the repulsion of equal charges, the so-called space charge limit, which is usually orders of magnitudes lower than the concentration that is required to measure absorption.[109] Instead, the influence of the light on the analyte has to be probed to obtain a spectrum, which is often referred to as action spectroscopy. Irradiation of ions with powerful laser beams in the gas phase can for example induce dissociation of analyte molecules. This action can be monitored as a function of the wavelength to generate a spectrum.[110]

2.3.1 Infrared Multiple Photon Dissociation Spectroscopy

Infrared Multiple Photon Dissociation (IRMPD) spectroscopy is one of the most straightforward approaches for gas-phase ion spectroscopy (Figure 2.9a). Here, resonant photons from a tuneable IR laser are absorbed by the ion, which leads to ion heating and subsequent fragmentation of the parent ion. Since the energy of a single IR photon is not enough to dissociate a covalent bond, multiple photons need to be absorbed sequentially. However, IR light induces the cleavage of the weakest bond rather than specific bonds. Energetically, this phenomenon can be explained by the intramolecular vibrational redistribution (IVR).[110] Immediately after the absorption of a photon, the ion relaxes to the ground state by IVR. As the energy cannot be dissipated, in the time frame of the experiment, it will be stored in the vibrational background states of the ion. This process is usually much faster than the time interval between two-photon absorption events and therefore leads to slow heating of the ions. As a result, the ion becomes thermally activated till fragmentation, with the weakest bonds dissociating first. By plotting the fragmentation yield against the wavelength of the laser beam an absorption-like IR spectrum can be derived.[111, 112] Especially in IRMPD spectroscopy, the anharmonicity of the populated vibrational modes, leads to an

internal energy-dependent redshift and band broadening of the observed absorptions.[110] Spectra obtained for ions with bonds that can be readily broken show a closer resemblance to the calculated (linear) spectra.

2.3.2 Messenger-Tagging Spectroscopy

The inherent drawback of IRMPD is an increased width of the absorption bands, which usually leads to rather congested, poorly resolved spectra. A strategy to circumvent this is messenger-tagging spectroscopy. Here, the ions are trapped and thermalized in a cold ion trap into which an inert neutral tagging gas is pulsed. The ions form weakly bound Van der Waals complexes with ideally a single molecule of the tagging gas. Irradiating these complexes with resonant photons leads to dissociation of the tag (Figure 2.9b).[113-115] Tagging efficiencies in the ion trap are highly dependent on the type of tagging gas, the temperature, and the charge state of the ion.[116] Plotting the ratio of untagged/tagged ions against the wavelength of the IR beam again yields an IR spectrum. As photofragmentation occurs ideally after the absorption of one single photon and due to the intrinsically low temperature of the ions a well-resolved IR spectrum with narrow absorption bands is obtained. Therefore, it can be compared to computed IR spectra more reliably and with higher confidence. Another advantage of this single-photon process is that it allows for the use of comparatively low-power laser systems, such as Optical Parametric Oscillators (OPOs), allowing for broad use in laboratories in a tabletop format. While tagging spectroscopy produces comparatively sharp spectra it also has its disadvantages. Ion activation through e.g. collision with residual gas in the high vacuum can lead to dissociation of the tag without irradiation leading to a source of background signal. Experimentally it is also challenging to condense only a signal tag onto the ion, leading to the formation of multiply tagged ions, which causes recorded signal intensities to be less certain.

2.3.3 Helium Droplet Spectroscopy

Another approach to acquire cold-ion IR spectra is based on the encapsulation of ions in cryogenic superfluid helium nanodroplets, which have an equilibrium temperature of 0.4 K. Irradiating the embedded ions with multiple resonant photons leads to gradual evaporation of helium atoms and eventually the release of the ions from the matrix, which in turn is detected as action by a mass analyzer.[117-119] Technically, this experiment is performed by capturing the ions in an ion trap through which a pulsed beam of helium nanodroplets is guided. The nanodroplets are generated by free jet expansion of pressurized helium through a pulsed valve into the vacuum. The helium droplets pick up the trapped ions and guide them to the detection region, as the elevated kinetic energy of the droplets allows the encapsulated ions to overcome the endcap potential of the ion trap. Subsequently, the ions are irradiated by IR photons. When an ion absorbs a resonant photon, it dissipates the thermal energy to the helium matrix. Through evaporative cooling, the helium droplet retains a temperature of 0.4 K but shrinks in size. After several absorption/evaporation cycles, bare ions are released following a mechanism that is not completely understood to date (Figure 2.9c). Spectra obtained by this method are completely background-free, as only ions released from the droplets are detected. The low temperatures, and therefore a lower number of populated vibrational states, lead to remarkedly sharp absorption bands.

2.4 Mass Spectrometry-based Glycosaminoglycomics

The study of the glycome is known as glycomics. Glycosaminoglycomics, therefore, studies the structure, interaction, and function of GAGs. While glycomics, especially of *N*-glycans, is comparatively well-established, glycosaminoglycomics remains in its infancy. There are no well-established techniques to study GAGs, often structure elucidation is already the first challenge. Since the core structure of GAGs is usually known, most of the structure elucidation techniques focus on the identification of the heterogeneous sulfation pattern. Over the years a multitude of proof-of-concept methods have been developed to sequence GAGs, which will be discussed in the following chapter.

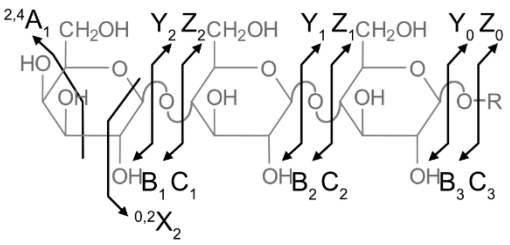

Figure 2.10: Overview of the Domon-Castello nomenclature for the annotation of glycan fragments. A linear trisaccharide is shown.

A common language to describe fragmentation of glycans is the Domon-Castello nomenclature[120] which works analogues to its peptide counterpart. A_i, B_i, and C_i labeled structures indicate fragments containing the terminal, nonreducing, glycan unit, while X_i, Y_i, and Z_i labeled structures mark glycan fragments containing the reducing-end. A_i and X_i mark cross-ring cleavages while B_i, C_i, and Y_i, Z_i indicate cleavages at either side of the glycosidic bond. The i index gives the number of monosaccharides contained in the fragment ion. A short example of the Domon-Castello nomenclature is found in Figure 2.10.

2.4.1 General Approach

The heterogeneity of GAGs originates from their sulfation pattern. Therefore, most structural elucidation techniques focus on determining the sulfate positions. A major difficulty for all MS-based GAG analysis approaches is the labile nature of the sulfate groups.[121, 122] During ion activation the sulfates easily cleave off as neutral sulfur trioxides, leaving their position unknown.[123] This occurs at much lower energies than the wanted glycosidic bond or cross-ring cleavages, which carry structural information. Neutral loss of sulfates can already occur during ionization. Therefore, to transfer the ions into the gas phase, a suitable soft ionization method is required.

ESI mostly fulfils these requirements and is already found in most commercial setups. During the ESI process dissolved analytes are sprayed from a capillary under the influence of an electric field at ambient pressures. The resulting charged solvent droplets evaporate and leave the charge with the analyte.[124] With this process mostly quasimolecular ions are formed, meaning the charge is introduced into the molecule by either a bound ionic species (e.g. metal ions) or, by attaching or detaching a positive hydrogen ion (proton).[125] This process occurs

with near-to-non ion activation, but residual gas pressure in the source region nevertheless often leads to unwanted fragmentation.

The neutral loss of sulfates can also be mostly prevented by deprotonating them, this is achieved by either measuring in ion negative mode or making use of the extensive adduct formation that commonly is associated with the ESI process. A combination of both approaches is usually the case.

2.4.2 Fragmentation-based Structure Elucidation

The most common MS fragmentation method is collision-induced dissociation (CID), which is attributable to its comparatively easy instrumental implementation and its tremendous success in the field of proteomics.[126, 127] In CID the analyte collides with thousands of neutral buffer gas molecules which thermally excites it. Through an unimolecular dissociation process, similar to IRMPD, the analyte fragments at its weakest bonds first.[128]

There are several approaches for CID-based GAG sequencing. Kailemia *et al.*[129] were able to sequence a highly sulfated synthetic heparin pentasaccharide using only CID. For this, all ten acidic protons in the structure had to be deprotonated or exchanged against sodium ions. The resulting $[M\text{-}10H+7Na]^{3-}$ ion was then able to provide diagnostic fragments after CID. Structures still containing acidic protons did not. The needed high salt concentrations in the solvent usually lead to very convoluted mass spectra and poor ionization efficiency. Therefore, several approaches have been developed to circumvent the need for fully deprotonated structures. Permethylation is usually performed on glycan structures to enhance ionization efficiency and structure coverage during fragmentation.[130-132] A similar approach has been applied by Huang *et al.*[133-135] They first permethylated sulfated GAG structures, desulfated them and lastly blocked the resulting free hydroxyl groups by acylation with trideuteroacetic acid. The resulting structures were able to effectively be sequenced using CID in the ion-positive mode without the need for high salt concentrations utilizing mostly the $[M+Na]^{+}$ and $[M+2Na]^{2+}$ species. The main drawback is the needed long derivatization time of up to three days and the use of the highly toxic methyl iodide. An

alternate version of this workflow was developed by Liu *et al.*[136] Instead of the classical permethylation they peracylated their structure using propionic acid anhydride to then desulfate them. Sequencing was then achieved through fragmentation of $[M+H]^+$ and $[M+2H]^{2+}$ species. This method omits the need for methyl iodide but increases derivatization time to five days. Both methods also increase the hydrophobicity of the analyzed GAGs, giving the possibility to utilize common reverse phase LC-MS workflows for prior purification before analysis.[135] While both glycosidic bond and cross-ring fragments carry structural information, cross-ring fragments are usually preferred since they allow for the assignment of sulfate positions on a monosaccharide level. For a cross-ring fragment, two covalent bonds need to be broken in contrast to the single bond for a glycosidic bond fragment. Therefore, CID mostly results in fragments along the glycosidic bond. Miller *et al.*[137] developed a CID-IMS-based method to make use of this apparent weakness. By comparing Y and B fragment ion CCS values to CCS values of standards from a developed database, a larger HS structure was able to be sequenced. This also included the ability to distinguish the often-neglected C5-isomers, glucuronic and iduronic acid, which have no obvious difference in their respective CID fragmentation pattern[138] and were not resolved in the previously discussed sequencing approaches.

The inherent disadvantages of CID to not distinguish between the uronic acids and the lack of cross-ring cleavages lead to the rise of sequencing approaches utilizing alternate fragmentation methods, including the electron-based dissociation methods. These methods usually attach or detach an electron from the analyte ion which often then leads to a radical-induced dissociation.

Electron detachment dissociation (EDD) was widely studied for GAG sequencing purposes.[139-148] Its ability to produce an abundance of cross-ring cleavages, while retaining the sulfo-functionality is very advantageous for a high GAG sequence coverage. Especially in focus of EDD research is the ability to distinguish the C5-isomeric uronic acids. Wolff *et al.*[142] were able to distinguish a set of isomeric HS tetrasaccharides differing only in their second uronic acids. The assignment was carried out based on the signal intensity of diagnostic fragments. In a similar manner, Agyekum *et al.*[139] were able to distinguish HS tetrasaccharides

with both uronic acids varying in their stereochemistry. While EDD is powerful for structure elucidation purposes, it also requires a costly FTICR-MS and high activation times, which prevents its use in LC-MS workflows. Negative electron transfer dissociation (NETD) shows none of these weaknesses. NETD utilizes an electron transfer reagent, that through an ion-ion reaction detaches an electron from a negatively multiply charged ion precursor. NETD can be implemented in common ion trap mass spectrometers and can be performed in a timescale compatible with LC. Leach *et al.*[149] were able to sequence a CS decasaccharide utilizing NETD and proved its general applicability. Wolff *et al.*[150] also confirmed the epimer differentiation seen in EDD to be present in NETD. Stickney *et al.*[151] successfully coupled capillary electrophoresis to NETD-MS and successfully sequenced HS polysaccharides out of a mixture.

Recently, ultraviolet photodissociation (UVPD) was used for GAG sequencing. UVPD utilizes ultraviolet light to electronically excite the targeted analyte which then can lead to a dissociation. In contrast to IRMPD, UVPD is a single photon process, leading to fragmentation of the analyte after a single photo absorption. In a proof-of-concept study, Racaud *et al.*[152] utilized UVPD to determine the sulfate position in HS disaccharides. Similar to the electron-based fragmentation approaches, a high degree of diagnostic cross-ring cleavages was achieved. Klein *et al.*[153] then used UVPD to sequence larger GAG structures up to a DS decasaccharide and even a highly sulfated HS pentasaccharide.

While IRMPD has also been used for fragmentation-based structure elucidation of GAGs,[140, 141, 143, 144] IRMPD action spectroscopy opens the way for spectroscopy-based structure elucidation methods which will be discussed in the following.

2.4.3 Infrared Spectroscopy-based Structure Elucidation

During ionization, when several possible charge sites are present, charge position isomers can form. Usually, these charge position isomers are interconvertible in the time scale of an MS experiment and therefore irrelevant for fragmentation-based elucidation techniques. Since spectroscopic sequencing techniques mostly focus on matching of recorded spectra to

library spectra, charge isomers pose a tremendous hindrance. Every charge isomers possess a unique spectroscopic fingerprint; an abundance of these charge isomers therefore leads to an overcrowded spectrum. IR spectroscopy is usually performed on fully deprotonated ions in MS negative mode to prevent the formation of charge isomers. An exception is often seen in IRMPD experiments, where the existence of a low energy fragmentation channel (desulfation) is seen with a higher benefit than the negative side effects of charge isomers on the spectral quality.

Early work on gas-phase GAGs spectroscopy started with the analysis of mono- and disaccharide units with the greater goal of developing a tandem MS (MS/MS)-IR sequencing approach.[154, 155] IRMPD experiments by Schindler *et al.*[156] showed promising results for the differentiation of both sulfated monosaccharides and GAG disaccharides. Interestingly, major spectral differences were observed in the 2700–3700 cm^{-1} range. Here, it was possible to distinguish 2*O*-/6*O*-sulfated HS and 4*O*-/6*O*-sulfated CS disaccharides from each other. An increasing number of spectral differences can be observed in the ammonium adducts that are formed in positive ion mode. Further studies by Renois-Predelus *et al.*[157] showed a proof of principle for MS^n-IR sequencing of smaller GAG oligosaccharides. By comparing IR spectra of Y and B fragments from a larger GAG oligosaccharide to library spectra obtained from standards, a sulfated DS tetrasaccharide was sequenced.

Khanal *et al.*[158] obtained cold-IR spectra of GAG disaccharides by combining IMS with messenger-tagging spectroscopy. The probed samples consisted of three isomeric singly sulfated CS and two singly sulfated HS disaccharides. The experiments were performed on the $[M-H+2Na]^+$ species in positive mode. While IMS struggled to separate most of the isomers, cold IR spectroscopy, in the range of 3200 – 3700 cm^{-1}, was able to unambiguously identify the GAGs.

Furthermore, cold IR spectroscopy in helium droplets of all CS disaccharides including the bare backbone structure and the higher sulfated disaccharides was conducted on deprotonated negative ions in the 900 – 1800 cm^{-1} range by Lettow *et al.*[159] The charge state was chosen so that it equals the number of sulfate groups on the ion, except for the non-sulfated disaccharide, which was measured singly negatively charged. The different

positional sulfated isomers could be unambiguously differentiated from each other. They show diagnostic features in the region of the symmetric and antisymmetric SO_3^- stretching vibrations. Interestingly, the spectra of the doubly sulfated disaccharides were much less congested, with many absorption bands nearly reaching the bandwidth of the laser. These data can be explained by the reduced number of low-energy conformers in higher-charged species. Charge-charge repulsion forces the ions into only a few conformers, resulting in fewer absorption bands and a clearer spectrum.

Using DFT calculations, ca. 250 conformers were generated for each disaccharide. Structures from this pool with relative energies up to 50 kJ mol^{-1} were selected and characterized using two criteria: (1) the intramolecular distances of charged sulfates toward the hydrogens of the carboxyl and amide groups and (2) the dihedral angles Ψ(C1-O-C3-C4) and Φ(C2-C1-O-C3). Structures that are close to each other in the plot will likely converge into the same low-energy conformer. The results confirmed the growing conformational heterogeneity in CS disaccharides with a decreasing number of charged sulfate groups.

Cold-ion IR spectroscopy experiments using helium droplets were conducted on larger GAG oligosaccharides by Lettow *et al.*[160] The highly sulfated pentasaccharide served as a model system. Spectra of the positively charged doubly protonated and the doubly sodiated species were recorded in the range of 1000 – 1800 cm^{-1}. Additionally, IRMPD spectra of the same species were recorded, leading to a drastic decrease in the resolution. The effect of sulfate groups was studied by comparing the IR pattern of a HA tetrasaccharide to a 6*O*-sulfated HA tetrasaccharide. The spectra show that the charge for the sulfated species is only located at the sulfates indicated by the missing antisymmetric carboxylate stretching vibration. Also, the sulfate groups showed two very well-resolved bands at 1200 and 1350 cm^{-1}, a wavenumber region that is void for the non-sulfated species.

Lettow *et al.*[161] also studied the effect of the uronic acid epimers on the recorded spectra. Spectra of GAG tetrasaccharides bearing different glucuronic/iduronic acid combinations were recorded between 1000 – 1800 cm^{-1}. All isomeric species were differentiable based on their IR patterns. Interestingly, the linear combination of the IR spectra of GlcA-GlcA and IdoA-IdoA looks remarkably similar to that of IdoA-GlcA and GlcA-IdoA. To investigate the

structural motifs that lead to different IR signatures in this system DFT calculation on the native disaccharides IdoA-GlcNAc6S and GlcA-GlcNAc6S were performed. Structures with two dominant motifs were identified. In the GlcA-GlcNAc6S disaccharide, the carboxylic acid of the GlcA likely forms a hydrogen bond to the N-acetyl group of the GlcNAc6S. In the IdoA-GlcNAc6S disaccharide, on the other hand, the carboxylic acid forms a hydrogen bond with the deprotonated 6*O*-sulfate group.

3| Experimental Overview

In this chapter, the instruments used for this thesis are described in detail. First, the two extensively used commercial setups are described, focussing not only on their respective working principles but also on their limitations and possible pitfalls. The second half of this chapter gives insight into the fully home-built gas-phase IR instruments developed by the group of Gert von Helden at the Fritz-Haber Institute. The laser setups used for the instruments are also briefly described at the end of each respective sub-chapter. Further experimental details can be found at the end of chapters 4-6.

3.1 Synapt G2-S

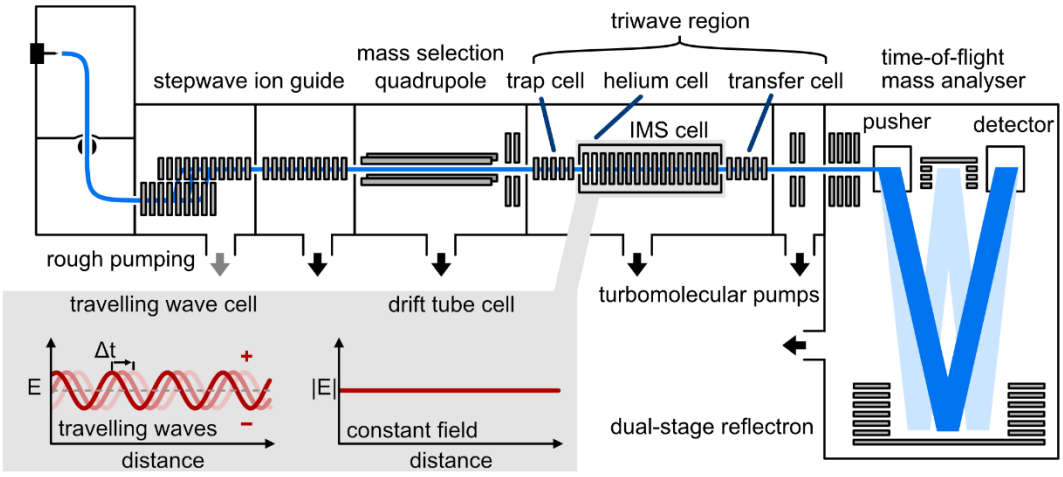

Figure 3.1: Schematic overview of the Synapt G2-S HDMS ion mobility instrument. Ions are generated by atmospheric pressure ESI and introduced into the MS via the sample cone. The stepwave ion guide acts as a desolvation stage and transfers the ions into the quadrupole for *m*/*z*-selection. The *m*/*z*-selected ions then enter the trap cell where they can be fragmented using CID. Afterwards, the ions are transferred into the buffer-gas-filled IMS cell. Two instruments were used with either a TW-IMS or DT-IMS cell in the case of the modified Synapt (grey box). After IMS separation the ions are transferred into the time-of-flight analyzer and subsequently detected.

For mobility analysis of fragment ions, the Synapt G2-S HDMS (Waters Corporation, Manchester, UK; see Figure 3.1), a second-generation TW-IM-MS instrument,[96] was utilized. The instrument can be equipped with either an atmospheric pressure Z-spray ESI or nano-electrospray ionization (nESI) source on which a voltage between 0.8 - 1.2 kV is applied. The nESI source is equipped with an XYZ-translation stage used to position the emitter ~1 cm from the MS inlet which is held at ground potential. The MS inlet leads directly to the segmented stepwave ion guide with superimposed DC, RF, and a travelling wave voltage. The stepwave mostly acts as a desolvation stage and filters out solvent droplets that did not evaporate completely, it also acts as an ion guide which leads the ions into the quadrupole. The quadrupole can be used for *m*/*z*-selection and otherwise just acts as an ion guide to transfer ions into the triwave region. The triwave region consists of stacked ring-electrodes

and is composed of four segments, the trap cell, the helium cell, the IMS cell, and the transfer cell. A travelling wave voltage is transversing through all four segments of the triwave region.[162] The trap cell can act as a CID cell for the activation and fragmentation of ions. It also acts as an ion trap to store ions from the, till then, continues ion flux. Most unwanted ion activation originates from the trap cell. The most influential voltages that impact ion activation are the trap bias, which influences the speed with which the ions enter the gas-filled cell; the travelling wave voltage height, which influences the peak voltage of the travelling wave through the trap cell and the trap collision energy which gives the DC voltage across the trap cell. Lower voltages across these described values generally lead to softer, but considerably lower ion transmission through the trap cell. From the trap cell, the ions are pulsed into the helium cell which is often seen as part of the IMS cell. As the name suggests, the cell is filled with helium to soften the impact of the injection from the trap cell and prevent further unwanted ion activation. In the case of the commercial TW-IMS instrument, the travelling wave voltage is dragging the ions through the gas-filled IMS cell separating the ion as described in section 2.2.2. In most cases, nitrogen is used as drift gas, but it is important to note that due to leakages from the helium cell, a nitrogen/helium mixture is present in the IMS cell. The calibration approach described in section 2.2.2 can only partially account for this since the CCS values from calibrants are generally measured in pure gases only.

After the ion mobility separation, the ions enter the transfer cell which can act as a CID cell and otherwise just transfer the ions into the time-of-flight (TOF) mass analyzer. The TOF mass analyzer can operate either in sensitivity or resolution mode (V- or W-mode). Since the repetition rate of the TOF is much faster than the IMS separation the detector at the end of the TOF analyzer acts both as a detector for the m/z determination and the drift time determination. The TOF repetition rate is fixed at 54.0 μs (~18.5 kHz) and a full IMS scan is fixed to 200 TOF pulses (bins). Combined, a maximum drift time of 10.8 ms is recorded. The advantage of coupling m/z and drift time measurements is the ability to extract multiple drift times, or so-called arrival time distributions (ATDs), from a single IMS scan which proves especially powerful when measuring complex sample mixtures.

A modified DT-IMS Synapt G2-S is used for direct CCS value measurements.[98, 163] The ion optics and control software in this Synapt are identical to the non-modified version described above. The only difference is that the 250.5 mm long TW-IMS cell including the helium cell was exchanged for a DT-IMS cell. This modification enables direct CCS measurement with the step-field method described in section 2.2.1 but decreases the ion mobility resolution considerably (~3-fold). CCS values were recorded in helium drift gas at a pressure of 2.2 Torr (~2.9 mbar). The temperature of the drift cell is measured with a Pt100 resistance thermometer which is attached to the outside of the vacuum housing of the drift cell. Drift times for CCS calculations were recorded at eight different drift voltages.

3.2 timsTOF Pro

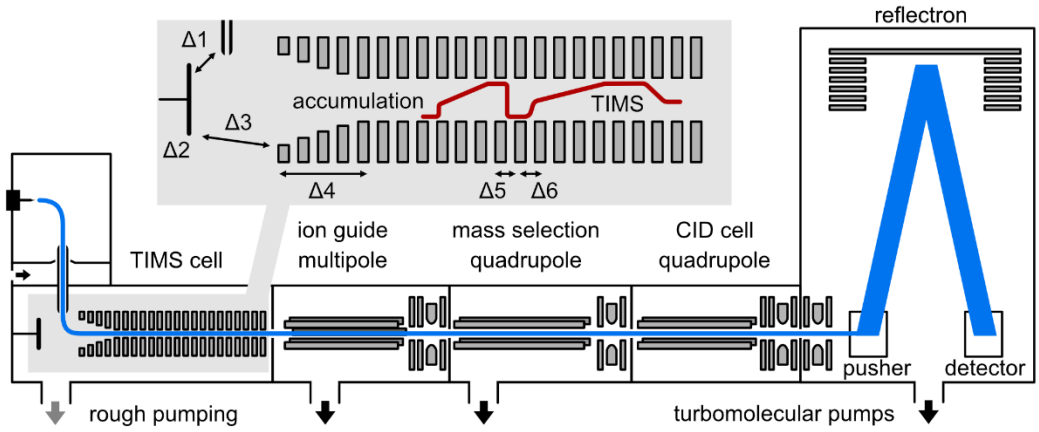

Figure 3.2: Schematic overview of the timsTOF Pro ion mobility instrument. Ions are generated by atmospheric pressure ESI and are introduced into the MS through a metal-coated glass capillary. They enter the TIMS cell (grey box) which separates the ions by size and leads them into a multipole which acts as an ion guide for the transfer into the quadrupole. The quadrupole can be used for *m*/*z*-selection and guides the ions into the CID cell. Afterwards, the ions are transferred into the time-of-flight analyzer and subsequently detected.

The TIMS instrument utilized in this thesis is the timsTOF Pro (Bruker Daltonics, Bremen, D; Figure 3.2) a third-generation IM-MS instrument. Ions are generated either via an

atmospheric pressure ESI source or a home-built nESI source described in detail in chapter 3.2.1. In contrast to the Synapt the ESI, the emitter is held at ground potential while at the MS inlet, a voltage between 1-3 kV is applied at a metal-coated glass capillary. The source chamber is flooded by a constant flow of heated nitrogen drying gas which aids the desolvation of the formed ions. Through the MS inlet, a constant ~3 L/min gas is introduced into the comparatively high-pressure chamber (~3 mbar) of the TIMS cell. Through a pressure gradient, the gas flow is directed to the end of the TIMS cell, which results in a dry gas flow (~150 m/s) acting as drift gas in the TIMS process.[100, 107]

This approach is efficient, reusing the drying gas as a drift gas, but it comes with several drawbacks. (1) The necessary high flow of gas makes the use of other alternate drift gasses, such as helium gas, difficult. (2) The drying gas temperature, which can be varied, has tremendous effects on the mobility separation since it is also heating the TIMS chamber.[105] Since the temperature of the TIMS chamber is not monitored it is hard to correct for these shifts. In constant operation such as for automated proteomics workflows, these shifts can be considered constant as the temperature will equilibrate. (3) The ESI solvent will also act as part of the drift gas. At usual ESI conditions of 100 µL/min acetonitrile injection and a drying gas flow of 3 L/min this results in ~1.5 vol% acetonitrile in the drift gas assuming all the solvent evaporates and enters the instrument. The solvent content in the drift gas can lead to transient ion-solvent clusters which shift the observed ion mobility.[105, 164, 165] Although the timsTOF is the highest resolving IM-MS instrument used in this work, no CCS values will be derived from it.

The timsTOF Pro utilizes a dual-stage TIMS cell: in the first stage ions are accumulated and after a set time they are released to the second stage, the TIMS analyzer where the ion mobility separation described in chapter 2.2.3 occurs. While the TIMS analyzer separates the ions the accumulation stage collects ions again for the next TIMS scan resulting in a higher duty cycle. The ion mobility resolution achieved in the timsTOF is dependent on several instrumental settings. These are the mobility range, which defines the start and end voltage of the voltage ramp, and the ramp time, which sets the total ramp scanning time. A low mobility range with a high ramp time leads to the high ion mobility resolution while reversely a high mobility

range with a low ramp time leads to a low resolution. The voltages in the TIMS cell are defined by six additional values which have no influence on the ion mobility resolution but affect ion activation and transmission. These voltages are given as Δ1-6 (Figure 3.2). Δ1 represents the voltage difference between the end of the inlet capillary to the deflector plate, and Δ2 is the difference between the deflector plate voltage during ion accumulation and ion deflection in case the ion accumulation time is not equal to the TIMS scan time. Δ3 gives the difference between the deflector plate voltage during accumulation and the entrance to the TIMS funnel, and Δ4 is the voltage difference between the entrance and exit of the funnel. Δ5 and Δ6 define the voltages between the accumulation cell and the TIMS analyzer. Generally lower values across all Δ-voltages lead to a softer ion transmission, but especially the Δ3, Δ4, and Δ6 voltages have a strong impact on activation which can also be used for fragmentation of ions before the TIMS analyzer, the so-called in-source fragmentation. Δ5 is usually kept at 0 V, an increase in the voltage can lead to a mobility-dependent partial transfer of ions from the accumulation cell into the TIMS analyzer. After the TIMS cell, the ions enter a multipole ion guide which leads into the quadrupole in which an *m*/*z*-selection can be performed. After the quadrupole, the ions enter the CID cell which can be used for ion activation and/or fragmentation.

Under soft TIMS conditions, the CID cell is the most activating region in the instrument, even when disabled. Unwanted fragmentation after the TIMS separation can lead to TIMS artefacts, e.g. a non-covalent dimer can be separated in the TIMS cell but fragments in the CID cell into its monomers, the recorded mobilogram of the monomer will then show two peaks, one for the intrinsic monomer and one for the dimer, which could be misinterpreted as an isomer or conformer.

After the CID cell, the ions enter the TOF analyzer for mass detection. Similar to the Synapt system the TOF analyzer also acts as a detector for the TIMS. The sampling rate per IMS scan depends on the used ramp time, with longer TIMS ramp times consisting of more TOF pulses and therefore a higher sampling rate.

3.2.1 3D-Printend Offline nESI Source

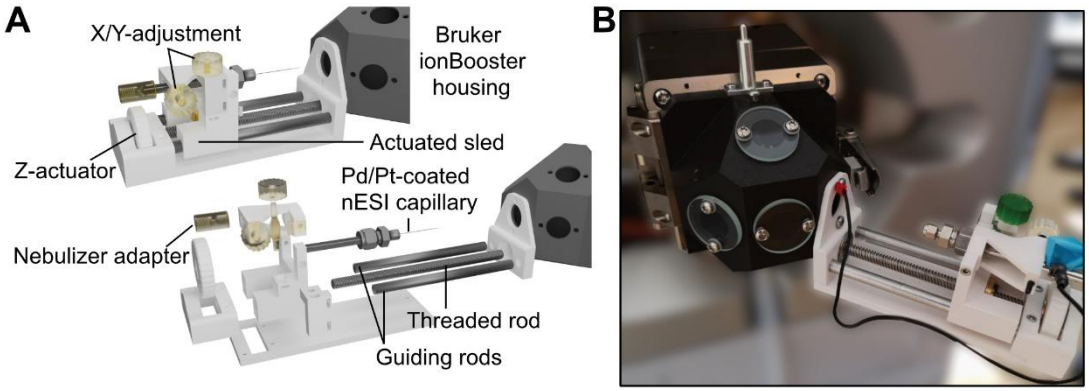

Figure 3.3: 3D-printed direct infusion nano-ESI source for Bruker instruments. a) 3D model of the source that can be built into a commercial Bruker ionBooster source block. b) The source is built into a Bruker timsTOF Pro. The emitter holder is held by the ionBooster housing. Figure adapted from Götze *et al.*[166]

For nESI direct injection on Bruker mass spectrometers such as the timsTOF, an nESI emitter must be placed near the instrument inlet and electrically connected to provide a stable voltage for the ionisation process. Regardless of the intended ion polarity, the standard ESI emitter in the Bruker ionBooster ESI source is held at ground potential by direct contact with the metal housing of the ion source. nESI emitters therefore only require contact with the instrument housing. The ionBooster source has three glass-covered windows that can be used to monitor the ESI spray. Each of these three windows provides access to the entrance of the mass spectrometer. We have developed a simple mechanism to guide an emitter close to the entrance capillary by replacing one of these windows (see Figure 3.3). The device consists of a manually operated carriage that carries an emitter adapter that can be rotated around a fixed point to position the emitter tip in the x and y dimension in front of the mass spectrometer inlet and that is connected to the source block via a grounding cable with one of the mounting screws. The parts for the device were either 3D printed from a polyethylene terephthalate glycol (PETG) filament using a filament-based printer or from a UV-curable resin using a stereolithography printer.[166]

The resulting spray is stable without additional heating and does not require a nebulising gas flow around the emitter, as is common with conventional ESI sources. Instead, the nebulising gas is used to pressurise the sample in the nESI emitter and to assist in the transport of the analyte solution in the tip. To achieve a stable spray, 1.0 - 1.8 kV capillary voltage, 400 - 700 V end plate offset and 0.0 - 1.5 bar back pressure are applied. The resulting sample output volume is in the range of nL/min.

3.3 Drift Tube IRMPD Instrument

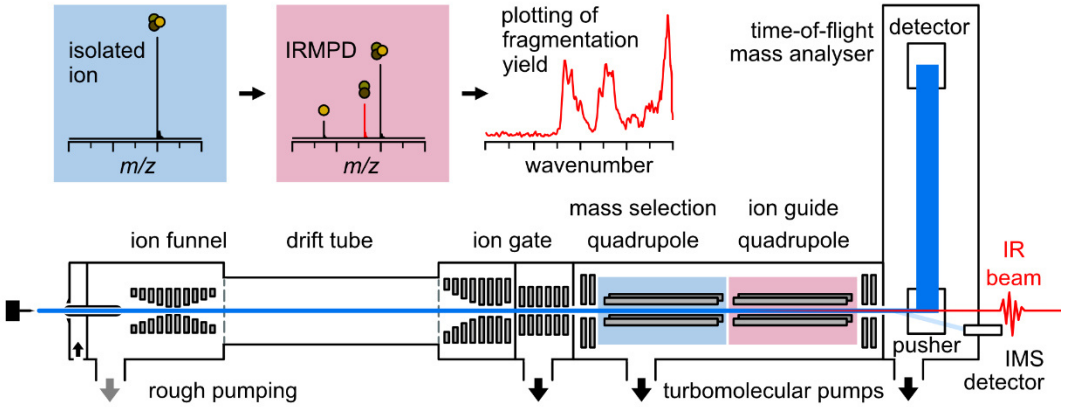

Figure 3.4: Schematic overview of the home-build drift tube IRMPD instrument. Ions are generated by atmospheric pressure nESI and enter the instrument through a metal capillary. Through the ion funnel, the ions are pulsed into the drift tube and separated by size, a quadrupole can be used for *m*/*z*-selection (blue box) and guides the ions further into the interaction region (red box) for IR irradiation. The ions and ion fragments are transferred into the time-of-flight analyzer and subsequently detected. Plotting of the IR-induced ion dissociation yields an absorption-like IR spectrum.

For the spectroscopy of metal-biomolecule complexes, a home-built DT-IMS-IRMPD mass spectrometer was used (Figure 3.4).[167] The instrument was constructed and maintained by the von Helden group at Fritz Haber Institute (FHI) of the Max Plank Society and has been updated to a more complex configuration by now (Chapter 3.4). Ions are generated by nESI and introduced into the mass spectrometer through a metal capillary. The capillary guides

the ions into the ion funnel where they are accumulated and pulsed into the 805.5 mm long drift tube. The ion funnel can be used for in-source ion activation and fragmentation. The drift tube is filled with either helium or nitrogen drift gas. Drift gas pressures are in the range of 2-3 mbar for nitrogen and 3-6 mbar for helium. IMS is performed within low-field limit conditions. Typical field strengths are in the range of 5-18 $V*cm^{-1}$. The temperature of the drift tube is monitored by a Pt100 resistance thermometer. The size-separated ions are collected by a funnel after the drift tube and guided through the ion gate to the *m*/*z*-selection quadrupole. The ion gate can be used to select ions of a particular drift time for further investigation. The selected ions are guided to the interaction region, where during IRMPD experiments, the laser is focused. Given a high enough laser intensity and oscillator strength of the ions, fragmentation will occur and an IRMPD spectrum can be recorded as described in section 2.3.1. The ions are then guided further into either the TOF mass analyzer or a separate off-axis detector to record IM-spectra without *m*/*z* information. Drift time and *m*/*z*-detection are not coupled as is the case in the previously described commercial instrumentations. To record drift times of single components, out of a mixture of signals, they must be isolated by the quadrupole first.

The tuneable laser light for the IRMPD experiment is provided by the FHI-Free Electron Laser (FEL)[168] which can be operated in the wavenumber range of ~200 - 3000 cm^{-1}. Pulse energies can reach up to 150 mJ, dependent on the operated wavenumber and FEL tune settings. The FHI-FEL operates at a frequency of 10 Hz while the drift tube of the instrument operates at frequencies of 20 Hz. Therefore, for every IM-MS scan of irradiated ions, a scan of non-irradiated ions is recorded which is used as background measurement to account for fluctuations in the ion signal intensity.

3.4 Drift Tube Cryogenic Tagging Instrument

Cryogenic IR spectroscopy of glycans was performed using a DT-IMS-Cryo-IR mass spectrometer (Figure 3.5). The instrument is the successor of the IRMPD instrument described in Chapter 3.3. The first half of the setup is almost identical to the IRMPD instrument differing

only in the length of the drift tube. For this setup, the drift tube was extended to 1612 mm. After the interaction region (ion guide quadrupole), instead of being guided into the TOF mass analyzer, the ions enter a quadrupole beam bender which guides the ions either to the on-axis detector to record IM-spectra or bends the ions 90° into a cold ion trap which is cooled to a temperature between 26 – 150 K.

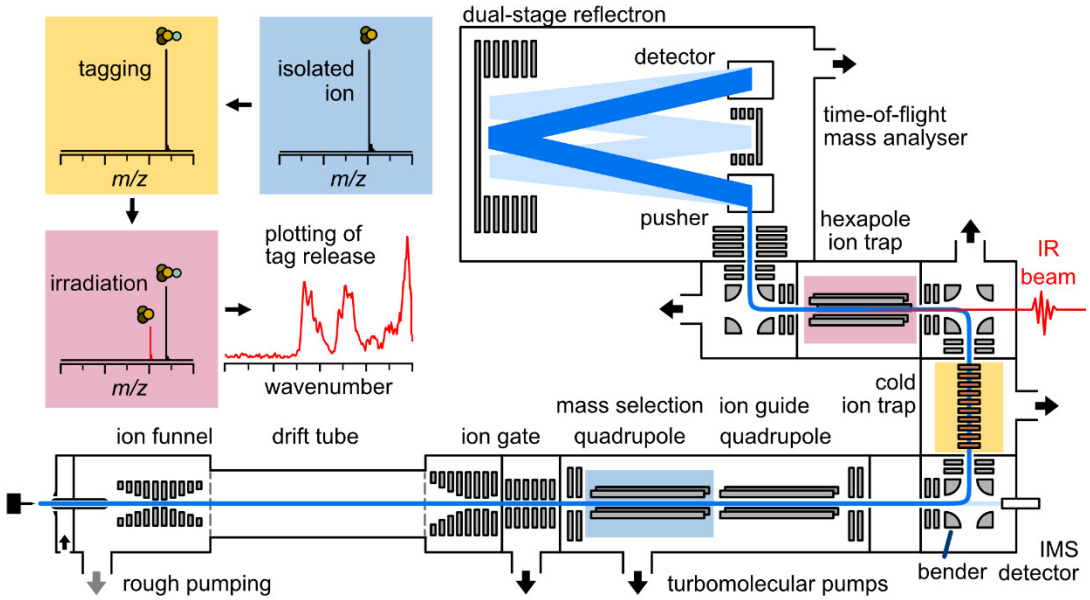

Figure 3.5: Schematic overview of the home-built drift tube cryogenic tagging IR instrument. The front end of the instrument equals the IRMPD instrument. After *m/z*-selection (blue box) ions are guided by a bender into the cold ion trap and tagged with nitrogen (yellow box). Afterwards, the tagged ions enter the hexapole ion trap for IR irradiation (red box). The ions are transferred into the time-of-flight analyzer and subsequently detected. Plotting the intensity of IR-induced tag release yields an absorption-like IR spectrum.

The cold ion trap is composed of two chambers: the tagging and ejection chamber. The ions first enter the buffer gas-filled tagging chamber and are cooled down to the temperature of the copper housing. During this process, the ions lose all excess kinetic energy and are trapped in the chamber for up to several seconds. The buffer gas is a mixture of helium and nitrogen. While nitrogen condenses onto the ions, acting as an ion tag, the helium remains in its gaseous form acting as carrier gas. After being transferred to the ejection chamber the ions

are accelerated and guided through a second bender into a hexapole ion trap. The hexapole ion trap acts as an interaction region for the tagged ions and the IR laser beam. After being guided by a third bender into the TOF mass analyzer a mass spectrum is recorded for the tagged and tag-released species. By plotting tag release against the IR wavenumber an absorption-like spectrum is derived.

Since the tag release requires considerably lower energy and therefore lower laser power, a tabletop laser system is utilized for the cryogenic IR measurements. The utilized laser is a LaserVision (Bellevue, WA, USA) OPO-OPA system. It can operate in a wavenumber range between ~833 and 2000 cm^{-1}. Pulse energies are in the range of ~1.2 mJ. The repetition rate of the laser is 10 Hz and of the experimental setup 20 Hz. As in the case of the IRMPD device, the tagging instrument measures a background mass spectrum for every laser-activated mass spectrum.

4 | Glycan-Induced Release of Gadolinium from MRI Contrast Agents

GAGs are linear highly acidic polysaccharides that serve as essential components of the extracellular matrix. There has been increasing evidence that GAGs can transchelate gadolinium ions from magnetic resonance imaging contrast agents. This unintended release of gadolinium is the leading cause of nephrogenic systemic fibrosis. However, the molecular details of the release remain poorly understood. This chapter provides direct evidence for gadolinium-GAG binding using the synthetic model substance Fondaparinux, a heparin mimetic. An FPX-gadolinium complex is observed in mass spectrometry experiments and the binding is characterized by isothermal titration calorimetry and IRMPD. Finally, the transchelation process is investigated on a molecular level utilizing CID experiments.

This chapter is based on the following reference:

L. Polewski, D. Dymnikova, W. Malicka, M. Lettow, G. Helden, C. Teutloff, M. Ballauff, M. Taupitz, R. Bittl, K. Pagel, *Angew. Chem. Int. Ed.* **2024**, submitted.

4.1 Introduction

Gadolinium-based contrast agents are frequently used in magnetic resonance imaging (MRI) where they drastically enhance the recorded signal intensity.[169, 170] Due to the high toxicity of free gadolinium ions, they are commonly applied as a complex with strong chelating agents, which reduces negative side effects of the free gadolinium. However, it is known that depending on the patient and the used contrast agent, a varying fraction of the injected gadolinium remains in the body.[171, 172] Linear contrast agents generally show more gadolinium retention than their macrocyclic analogues.[173, 174] This can be attributed to the higher binding affinity of gadolinium to the ligand and the drastically increased kinetic stability of macrocyclic contrast agents.[175] The most severe outcome of contrast agent retention is nephrogenic systemic fibrosis, a condition directly linked to contrast agent injection.[176, 177]

The chemical nature and the environment of the gadolinium that is retained in the body remains largely unknown.[178, 179] It has been proposed that gadolinium cations are initially released from the contrast agent via transchelation with a competing metal ion such as Zn^{2+}, Cu^{2+}, or Fe^{3+}.[180, 181] This mechanism has been shown for linear contrast agents; the release from macrocyclic contrast agents, on the other hand, remains poorly understood. Interestingly, MRI measurements revealed a delayed increase of T_1-relaxivity after injection of linear contrast agents, which is often referred to as late gadolinium enhancement. A possible explanation is the binding of gadolinium to an unknown macromolecular species.

GAGs, as a major component of the extracellular matrix, have recently been identified as one of the likely binding partners.[182, 183] GAGs are linear, highly acidic polysaccharides, which are pharmaco- and physiologically highly relevant.[184] As polyelectrolytes GAGs are known to bind to a variety of metal ions,[185-188] which can lead to conformational changes in both the monosaccharides[189] and the higher-order structure.[186, 190] In some cases the metal ion can also mediate interactions with otherwise unfavorable binding partners.[191-193]

Here the binding of gadolinium to Fondaparinux (FPX), a heparin-derived oligosaccharide is investigated. The experiments reveal the binding of Gd ions to FPX with μM affinity and their release from the chelating complex in the presence of FPX.

4.2 Results and Discussion

FPX is a synthetically derived pentasaccharide that is clinically used for anticoagulation.[194] Its structure (Figure 4.1a) closely resembles that of the active pentasaccharide present in heparin.[195] With a total of eight sulfate groups and two carboxylic acids, FPX possesses an abundance of possible gadolinium binding sites, which makes it an ideal model substance. After the addition of a gadolinium solution to FPX, an FPX-gadolinium complex can be observed using negative ESI-MS. The complex is visible in multiple charge states between -2 to -5. Deconvolution of the mass spectrum provides a clearer picture (Figure 4.1b). The FPX-gadolinium species can be readily identified based on the unique isotopic pattern of gadolinium. Given the tendency of the ESI process to induce nonspecific ionic adduct formation, particularly affecting the quantity of FPX bound to gadolinium, solvent data is essential for confirming the observed gadolinium binding.

4.2.1 Quantitative Gadolinium Binding Analysis

To access thermodynamic parameters, isothermal titration calorimetry (ITC) was performed on the FPX-gadolinium model system by Weronicka Malicka from the Haag Group. Figure 4.1c and d depict the ITC thermogram and the respective fit for heat injection amounts plotted against the molar ratio of the two reactants. From this data, the binding energy and affinity of the complex can be determined. A pronounced interaction between gadolinium ions and FPX is evident, with a binding energy (ΔG) of -29.4 kJ/mol and a significant binding affinity with a K_D measured at 6.9 μM. Despite an unfavourable enthalpy change (ΔH = 3.2 kJ/mol) associated with the binding of gadolinium ions to FPX, this thermodynamic imbalance is counteracted by a robust entropic contribution ($T\Delta S$ = 32.6 kJ/mol). The stoichiometry of the binding complex N = 1.3, suggests the presence of multiple binding sites for gadolinium ions

on a FPX molecule. The binding affinity of the gadolinium-FPX complex with a dissociation constant of 6.9 µM, is low compared to contrast agent complexes, which exhibit affinities more than ten orders of magnitude higher. Longer GAG chains are highly multivalent and are therefore expected to exhibit a considerably higher binding affinity towards gadolinium than FPX.[196] However, the binding affinity alone is likely not to be the major driving force for gadolinium retention in treated patients. Instead, it is expected to be a combination between the affinity and the high local concentration of GAGs in the involved tissues.

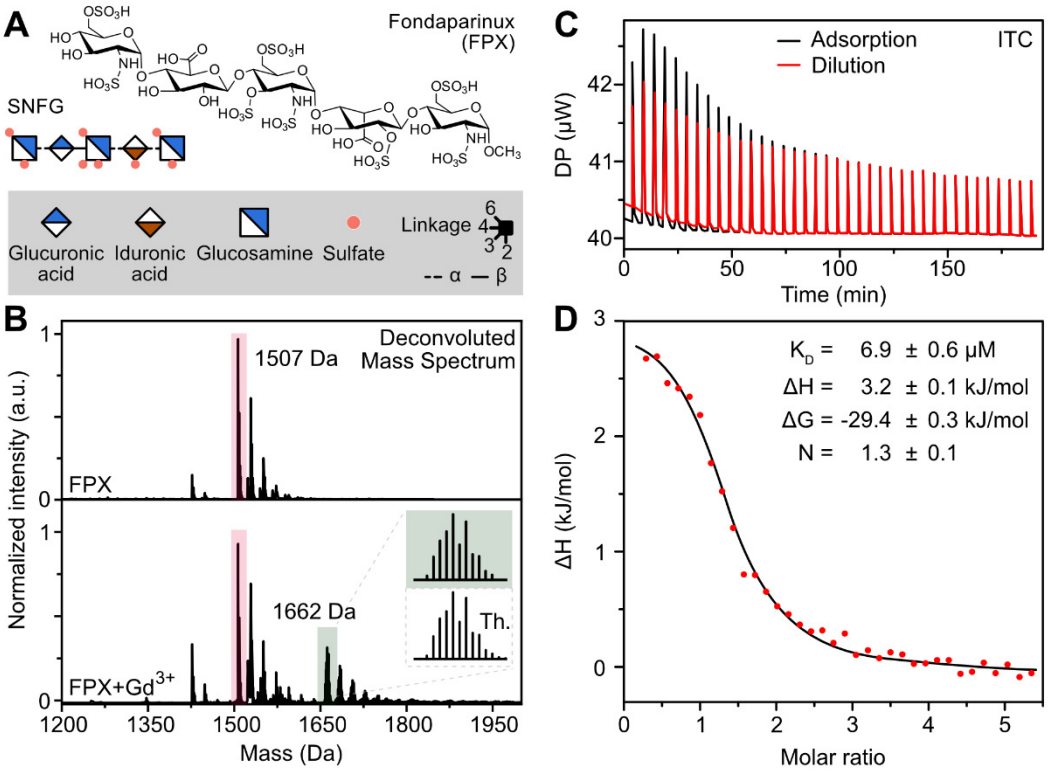

Figure 4.1: **a)** Fondaparinux (FPX), a synthetically derived highly sulfated pentasaccharide, is shown as a chemical structure and depicted using the SNFG.[26] **b)** Deconvoluted mass spectrum of FPX (highlighted red) and an equimolar FPX-$GdCl_3$ mixture. Both mass and the characteristic isotope pattern of gadolinium confirm the complex formation (highlighted green). **c)** Endothermic raw data of the gadolinium-FPX ITC experiments. Both adsorption (black) and dilution (red) are shown. d) Integrated amount of heat released from the titration plotted against the molar ratio of the components (Gd^{3+}/FPX).

4.2.2 Qualitative Gadolinium Binding Analysis

To investigate the binding of gadolinium to FPX on a molecular level, IMS-coupled IRMPD spectroscopy was performed. Both, IRMPD[197, 198] and IMS,[199] have been successfully applied to probe non-covalent interactions of biomolecules and their structures in the gas phase. The binding of gadolinium to FPX is likely mediated through the eight possible negatively charged sulfates and the two uronic acids. The $[FPX+Gd]^{4-}$ complex and a $[FPX+3Na]^{4-}$ complex are analyzed as a control. The IMS ATD of the gadolinium complex shows two conformational features (Figure 4.2a) with the compact conformer as a major component. The triple sodium complex shows a qualitatively similar ATD but instead with the extended rather than the compact conformer as a major component. This difference is likely due to the chelation of gadolinium by FPX, which stabilizes the compact conformers. In sodium adducts, on the other hand, the cations are evenly distributed along the saccharide chain, leading to an overall more extended arrangement. The compact and extended conformers of the sodium and gadolinium complexes were isolated as highlighted in Figure 4b and IRMPD spectroscopy between 1600-1850 cm^{-1} was performed on the selected species. The vibration of the carboxylic acid and its conjugated base, the carboxylate, from the two uronic acids of FPX, are easily distinguishable (Figure 4.2b). Carboxylic acids can be readily identified by their stretching vibration (v(C=O)) which most commonly appears between 1700-1800 cm^{-1}. In contrast, the carboxylate is characterized by an asymmetric stretching vibration ($v_{as}(COO^-)$) between 1600-1700 cm^{-1}.[200-202] Previous reports showed that charges on GAGs preferably reside at the sulfate groups, likely due to their higher acidity.[202, 203] Therefore, the presence of a carboxylate might indicate the participation of the group in the binding of gadolinium. A charge on the carboxylic acid could also result from an unfavourable charge position on the sulfates due to an increasing Coulomb repulsion from the additionally introduced negative charges. As the charges of the used control sodium complex mimics the number of charges in the gadolinium complex, with the difference that sodium is known to bind non-specifically, a possible influence of Coulomb repulsion can be probed.

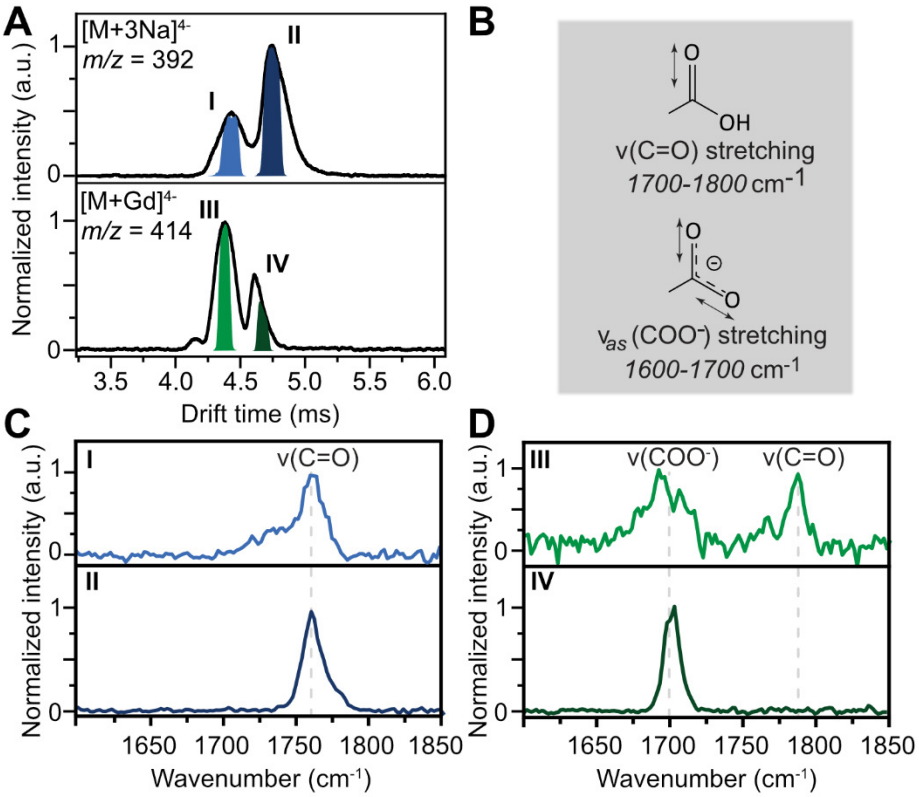

Figure 4.2: IMS-IRMPD experiments of FPX-cation complexes. **a)** ATD of the triple sodium (top) and the gadolinium (bottom) complex of FPX. The highlighted areas were isolated to perform mobility and *m/z*-selected IRMPD spectroscopy. **b)** Characteristic stretching vibrations of carboxylic acids and carboxylates, commonly visible between 1700-1800 cm^{-1} and 1600-1700 cm^{-1}, respectively. **c)** IRMPD spectra of the triple sodium adduct. Both isolated conformational groups, I and II, show a clear signal corresponding to carboxylic acid stretching vibration indicating no direct participation of the carboxylic acid in FPX-binding. **d)** IRMPD spectra of the FPX-gadolinium complex. The compact conformer group III showed two absorption bands corresponding to an asymmetric carboxylate stretching vibration at 1715 cm^{-1} and a carboxylic acid stretching vibration at 1790 cm^{-1}. The extended conformer IV showed only a stretching vibration corresponding to the carboxylate, indicating the binding participation of both carboxylic acids.

Both the compact and the extended conformers of the sodium complex (I and II) yield very similar spectra with an absorption maximum at 1760 cm^{-1} matching that of a carboxylic acid

(Figure 4.2c). This confirms the assumption that the sodium binding site is mainly governed by the charges positioned on the sulfates. For the compact conformer of the gadolinium complex (III), two absorption bands can be observed at 1700 cm^{-1} and 1780 cm^{-1} matching stretching frequencies of a carboxylate and a carboxylic acid, respectively (Figure 4.2d). Previous NMR experiments with calcium on FPX showed similar behaviour, where calcium preferably binds to iduronic acid.[204] The extended conformer of the gadolinium complex (IV) on the other hand, only shows a single absorption band at 1700 cm^{-1}, indicating a binding on both carboxylic acids, once again showing the specificity, with the gadolinium position determining the charge site.

4.2.3 Monitoring of Gas-Phase Transchelation

ESI-MS of GAGs in the presence of gadolinium-containing contrast agents yields noticeable signals of GAG-contrast agent complexes, which exhibit a very intriguing fragmentation behaviour. For gadopentetic acid (Figure 4.3a), commonly known as Magnevist, and FPX the complex appears at triply negatively charged ion at *m*/*z* 684. Activating the complex via CID results in two major fragments at *m*/*z* 392 and 830 (Figure 4b). Surprisingly, a transchelation in which the gadolinium remains bound to FPX (*m*/*z* 830) while the ligand of Magnevist (pentetic acid, *m*/*z* 392) is released. Minor fragments can also be observed at *m*/*z* 663 and 790 resulting from neutral loss of sulfate from the intact FPX-contrast agent and the FPX-gadolinium complexes respectively (Figure 4.3b). Similar transchelation processes can be observed with other contrast agents, such as gadodiamide and the macrocyclic contrast agent gadobuterol, albeit to a lower extent. As an alternate fragmentation path to the transchelation, the FPX-contrast agent complexes can undergo dissociation into the intact contrast agent and FPX (Figure 4.3c and d). The observed difference in dissociation behaviours is likely not connected to the kinetic stability of the contrast agents given that CID is a thermal fragmentation method. Before dissociation or transchelation, stable FPX-contrast agent complexes such as the gadodiamide complex tend to lose one or more sulfates, which likely influences the fragmentation behaviour. The loss of sulfates has two major effects on the system a) the loss of an additional binding partner for the gadolinium ion and b) the loss of

an additional acidic proton. Considering the previous results, which revealed a contribution of carboxylic acids to gadolinium binding and a considerable difference between the binding affinities of the contrast agent and the FPX-gadolinium complex (log K_D -20 for Magnevist, -5 for FPX-gadolinium), the loss of an acidic proton is likely the main driving force.

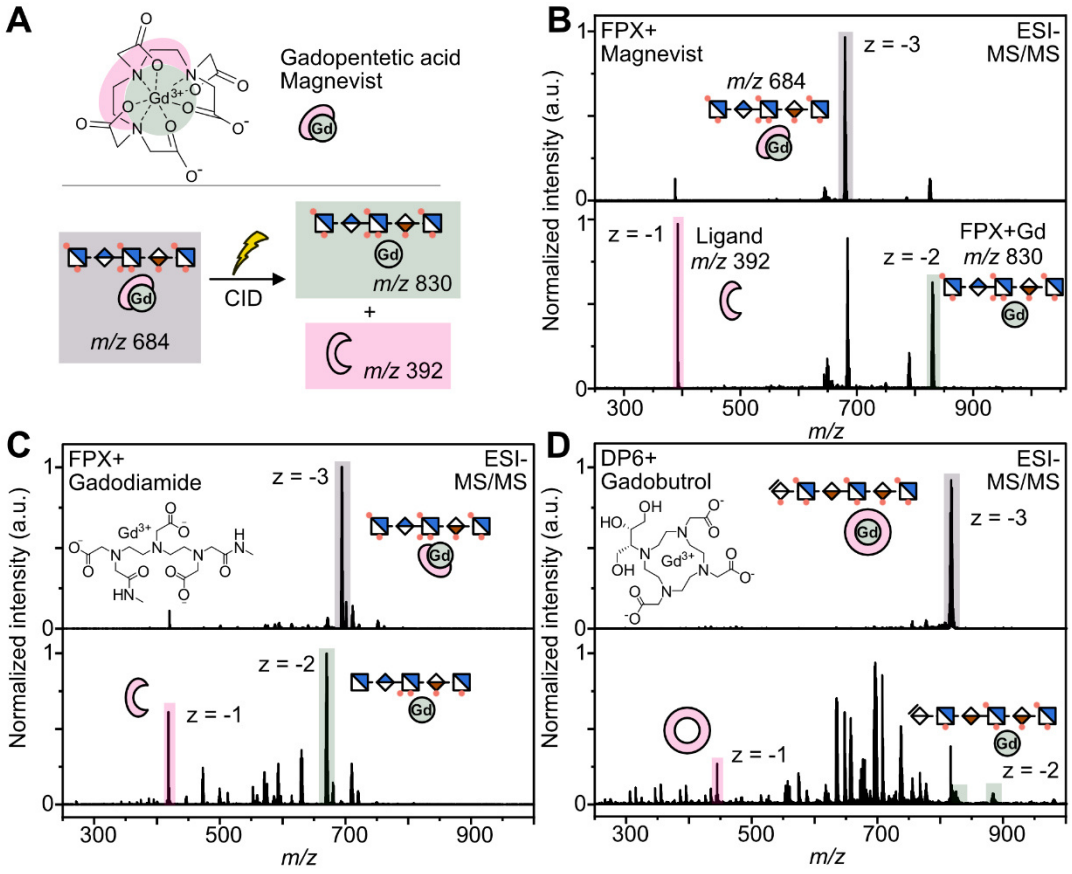

Figure 4.3: a) Gadopentetic acid a common linear ionic MRI contrast agent known as Magnevist and schematic fragmentation of the FPX-contrast agent complex (grey) to the free ligand (red) and the FPX-gadolinium complex (green). **b)** Isolated mass spectrum of the FPX-Magnevist complex (grey) and its CID-MS/MS-spectrum. Dissociation yields nearly exclusively transchelation products in the form of the gadolinium bond FPX (green) and the empty chelate ligand of Magnevist (red). **c)** Mass spectrum and CID-MS/MS of the FPX-Gadodiamide complex. **d)** Mass spectrum and CID-MS/MS of the FPX-Gadobutrol complex.

Even though it is unclear to which extent these complexes occur in solution, the influence of acidic protons will have a similar effect on the relative stability of contrast agent and GAG-gadolinium complexes. This suggests that the transchelation of contrast agents to GAGs may be more favourable in acidic environments, such as those found in inflamed tissues,[205] where late gadolinium enhancement is known to be more prevalent and even frequently utilized for diagnostic purposes.[206-208]

4.3 Conclusion

Gadolinium binding to the heparin-mimetic FPX was observed. With a variety of condensed- and gas-phase methods the binding was characterized. ITC measurements showed a low micromolar dissociation constant and a stoichiometry of the binding complex of N = ~1.3. Transchelation in tissue is therefore likely governed by a combination of the rather moderate affinity and a high local concentration of GAGs in the involved tissue. Gas-phase infrared spectroscopy experiments provided further molecular insights and revealed a preferable binding of gadolinium to the carboxylic groups. A high degree of sulfation is therefore not the only driving force for gadolinium binding to GAGs. Finally, the formation and dissociation of complexes between contrast agent and GAGs were observed using mass spectrometry. The dissociation of these complexes in the mass spectrometer was found to be largely determined by the availability of acidic protons. A complex with a high number of acidic protons favourably transchelates leading to the formation of gadolinium-bound GAG ions. In combination with the previous results, this provides a first molecular explanation for why the late gadolinium enhancement commonly observed in MRI is more prevalent in acidic tissue.

4.4 Experimental Section

Sample Preparation

Commercially available fondaparinux-sodium, solvents, and chemicals were purchased from Sigma-Aldrich (St Louis, USA). For MS applications fondaparinux-sodium was desalted using a 5 mL Cytiva (Washington D.C., USA) HiTrap desalting column at a 1 mL/min flow rate (water) with a Knauer (Berlin, Germany) FPLC system. For MS analysis Aqueous fondaparinux stock solution (1 mM) was further diluted before use with 100 mM ammonium acetate in water to yield 10-50 μM analyte solutions. For the IRMPD measurements, fondaparinux was diluted in water/methanol. (1/1; v/v). Commercially available GdCl3 (Gadolinium chloride hexahydrate, Sigma Aldrich) and FPX (Fondaparinux sodium salt, Sigma Aldrich) were used for stock solutions.

ITC Measurements

Experiments were performed on MicroCal VP-ITC (Malvern Panalytical GmbH, Germany). Each sample was degassed at the temperature of the respective experiment (25 °C) before the measurement. A total of 290 μL of 2 mM GdCl3 was titrated into the 1043 μL sample cell with 0.05 mM polysaccharide solution, with 56 or 46 successive injections in 5 or 6 μL steps, with a stirring rate of 307 rpm and a time interval of 300 s between each injection. For all experiments the instrument software (MicroCal PEAQ-ITC Analysis) was used for baseline adjustment, peak integration, and normalization of the reaction heats with respect to the molar amount of injected ligand, as well as for data fitting and binding parameter evaluation. The binding experiments were corrected for the heat of $GdCl_3$ dilution which had been determined separately ($GdCl_3$ titration into 20 mM sodium acetate buffer, pH 5.6).

Mobility-selected IR Spectroscopy

For the IRMPD spectroscopy, the in-house constructed drift-tube ion mobility-mass spectrometer was used. Ions are produced by nESI from a Pd/Pt-coated borosilicate capillary

and are transferred and stored in an entrance funnel. Afterwards, the ions are released by 150 μs long pulses into a drift tube filled with helium buffer gas (~5 mbar) and travel through the drift tube under the influence of a weak electric field (10-20 V/cm).

IRMPD spectra are recorded by selecting a drift time window using electrostatic deflection prior to mass selection in the quadrupole. The ion mobility and m/z selected ion cloud is then further irradiated by a 60 - 100 mJ 10 μs pulse of IR photons. The scanning was performed by wavenumber steps of 2 cm^{-1} and 25-75 averages were used per recorded point.

The tuneable light in the mid-IR range is supplied by the free-electron laser of the Fritz Haber Institute and transported to the instrument via an evacuated beamline. The last two meters of the beamline are purged with dry nitrogen to avoid water absorption.

MS Measurements

MS measurements were performed on a Bruker timsTOF Pro using the MS-only mode. Settings were optimized to prevent unwanted fragmentation with a quadrupole ion energy of 2.5 V, CID voltage of 7 V, collision gas flow rate of 65%, prepulse storage time of 9 μs, and transfer time of 100 μs. MS-CID measurements were performed on a Waters Synapt G2-S. Deconvolution of MS data was performed with an in-house developed program.

5| Ion Mobility Mass Spectrometry-based Disaccharide Analysis

Due to the complexity of GAG sequencing approaches the standard analysis of all GAGs is the "disaccharide analysis." This involves enzymatically breaking down GAGs into disaccharides, tagging them with a fluorescent label, and analyzing them using LC. However, LC is time-consuming, limiting the high-throughput analysis of GAG disaccharides. To overcome this, trapped ion mobility-mass spectrometry (TIM-MS) for the separation of isomeric GAG disaccharides is introduced here, reducing measurement time from hours to minutes. The complete set of HS/heparin disaccharides includes twelve structures, with eight having isomers. Since most disaccharides cannot be distinguished by TIM-MS in their unmodified form, chemical modifications were developed to simplify samples and improve differentiation. Quantification is done using stable isotope-labelled standards, which are readily available due to the modifications performed.

This chapter is based on the following reference:

L. Polewski, E. Moon, A. Zappe, M. Götze, G. P. Szekeres, C. Roth, K. Pagel, *Chem. Eur. J.* **2024**, e202400783.

5.1 Introduction

Glycans are crucial components of cell membranes, act as energy storage molecules, and mediate cellular communication.[209-211] Among them, GAGs stand out due to their therapeutic applications, making their analysis a priority in glycomics. GAGs are linear, often heavily sulfated polysaccharides made up of repeating disaccharide units, typically consisting of a uronic acid and a hexosamine[212] are ubiquitous in mammalian tissues and fluids, playing essential roles in processes such as inflammation, blood coagulation, and cell signaling.[213, 214] Heparin and HS form the most prominent group of GAGs. Heparin, mainly located in mast cells and basophils, is well-known for its anticoagulant properties.[215] In contrast, HS is found on cell surfaces and bound to proteoglycans in the extracellular matrix, where it is involved in biological activities such as cell adhesion, signalling, growth, and morphogenesis.[213, 214, 216] However, the direct relationships between the structure of Heparin/HS and their biological activity remain elusive due to their structural complexity. Despite their relatively simple composition, the complexity arises from diverse patterns of sulfation, backbone isomerization, and *N*-acetylation.[217] This structural complexity poses significant challenges for analysis. Because their biological activity is intricately tied to their structural features, understanding the fine structural details of heparin/HS is crucial for elucidating their functions and advancing glycan-based therapeutic interventions. Therefore, analytical methods that can precisely and sensitively characterize heparin/HS structures are essential in glycomics research.

Due to the intricate nature of GAG sequencing, a simpler approach is compositional disaccharide analysis, which can serve as a biomarker in disease progression. The usual workflow for heparin/HS disaccharide analysis involves enzymatic depolymerization followed by chromatographic separation and detection. Enzymatic depolymerization using specific GAG lyases such as heparinase I, II, and III generates disaccharide fragments from heparin/HS chains. (Figure 5.1a).[218] During depolymerization, the stereocenter at C5 of the uronic acid is lost, resulting in the formation of a 4-5-unsaturated 4-deoxy-hex-4-

enopyranuronic acid. This unsaturated uronic acid can be detected via UV absorption at 232 nm due to its conjugated 1-4 Michael system. However, UV absorption is typically very low, especially since samples are usually in the sub-microgram region. Therefore, a fluorophore is commonly attached to the reducing end of the disaccharides to enhance their detection.

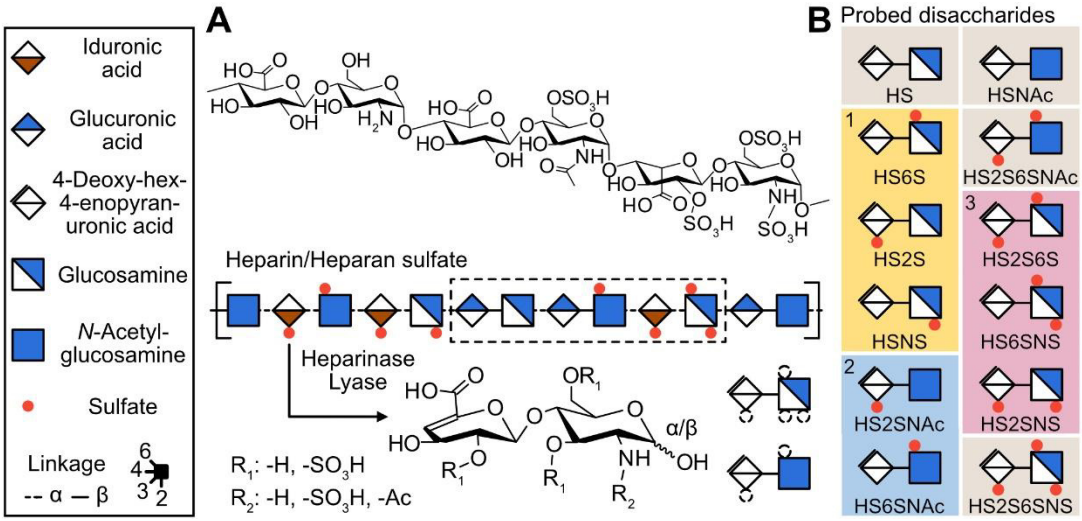

Figure 5.1: HS/heparin structure. **a)** Example of an HS structure and its simplified form based on SNFG.[26] The chemical structure (top) can be seen depicted as an SNFG in the dotted box. **b)** Probed disaccharides and the used nomenclature. Three isomeric disaccharide groups are present: group 1, monosulfated and non-acetylated (yellow); group 2, monosulfated and acetylated (blue); and group 3, disulfated and non-acetylated (red).

Various LC techniques have been utilized for the separation of GAG disaccharides, including hydrophilic interaction,[219] reversed phase,[220] ion pairing,[221] size exclusion, and strong anion exchange chromatography.[222] However, achieving a complete LC separation of HS disaccharides usually requires between half an hour to an hour, depending on the method and the range of disaccharides being analyzed. Furthermore, calibration, regeneration, and blank runs are necessary between sample injections to maintain column performance, although these are often not included in the total run time. Despite the relatively short LC analysis time compared to the total sample preparation time, the sequential nature of LC

separation contrasts with the capacity to process large batches of hundreds of samples at once during sample preparation, making it the time-limiting step. IMS has emerged as a powerful technique for separating glycans in the gas phase. Several studies have shown similarities between LC and IMS in terms of resolution and resolving power.[223, 224] IMS separation time is decreased compared to LC by a factor of >1000 with most IMS instruments operating in the sub-second region.[86] While IMS resolution is still lower than most LC methods, IMS instrumentation has drastically improved in recent years. With increasing IMS resolving power, the potential for the replacement of common LC-MS workflows with faster and more sample-efficient IM-MS workflows become increasingly enticing.

In this Chapter, a TIM-MS-based method is introduced to separate and characterize isomeric heparin/HS disaccharides from mixtures and biological samples. The entire analytical workflow takes only a few minutes, making it an attractive alternative to the comparatively slow established LC-MS/fluorescence detection (FLD) methods.

5.2 Results and Discussion

The standards for the twelve most common GAG-disaccharides are readily available. Among these, eight have isomeric structures that cannot be distinguished by mass spectrometry alone. These eight disaccharides form three distinct isomeric groups (Figure 5.1b): the first group includes three different monosulfated non-acetylated structures (yellow, 417 Da), the second group comprises three different monosulfated acetylated structures (blue, 459 Da), and the third group consists of three disulfated non-acetylated structures (red, 597 Da). Other non-isomeric structures include the unmodified HS-disaccharide, the acetylated non-sulfated disaccharide, a disulfated acetylated species, and the fully sulfated disaccharide variant.

5.2.1 Chemical Derivatization and Qualitative Isomer Separation

TIMS analysis with direct infusion of the isomeric disaccharide groups 1 and 3 show very complex mobilograms (Figure 5.2a) which do not allow a clear distinction of the components. The presence of reducing-end anomers (α/β) further complicates the analysis leading to the presence of at least six structures for each isomeric group.[225, 226] Propionylation was performed to simplify the sample. Both isomeric groups contain at least one structure with a primary amine group at the C2-position of the glucosamine, so selective *N*-propionylation of the amine reduces the number of isomers in each group from three to two (Figure 5.2b). The mobilograms of these isomeric groups show a significant reduction in complexity compared to the non-modified variants (Figure 5.2c). However, clear annotation of structures from a mixture remains challenging, especially for HS-2SNS and HS-6SNS (red). If a study focuses on structures with free amines, the propionylation step should be included to avoid ambiguity in the sulfation positions.

Further reduction of complexity and enhanced separation in TIMS is achieved by labelling the reducing-end of the disaccharides. Labelling through reductive amination removes the stereocenter at the anomeric carbon C1, reducing complexity. However, the choice of the reducing-end label is crucial, as different labels have been shown to either improve or worsen the separation of glycans using IMS.[6] Procainamide (ProA) is a suitable label for the separation of GAG disaccharides. It is commonly used as a fluorescence label for LC-FLD glycan analysis and also serves as a charge tag to improve the ionization efficiency of glycans in positive ion mode MS.[227, 228] However, due to their negative charge and the generally labile nature of sulfate groups in positively charged ions, TIMS analysis is conducted in negative ion polarity, here. The use of procainamide as a label significantly enhances the separation of certain isomers, particularly when compared to the structurally related label procaine (Appendix A, Figure A1), which consists of an ester bond instead of an amide.

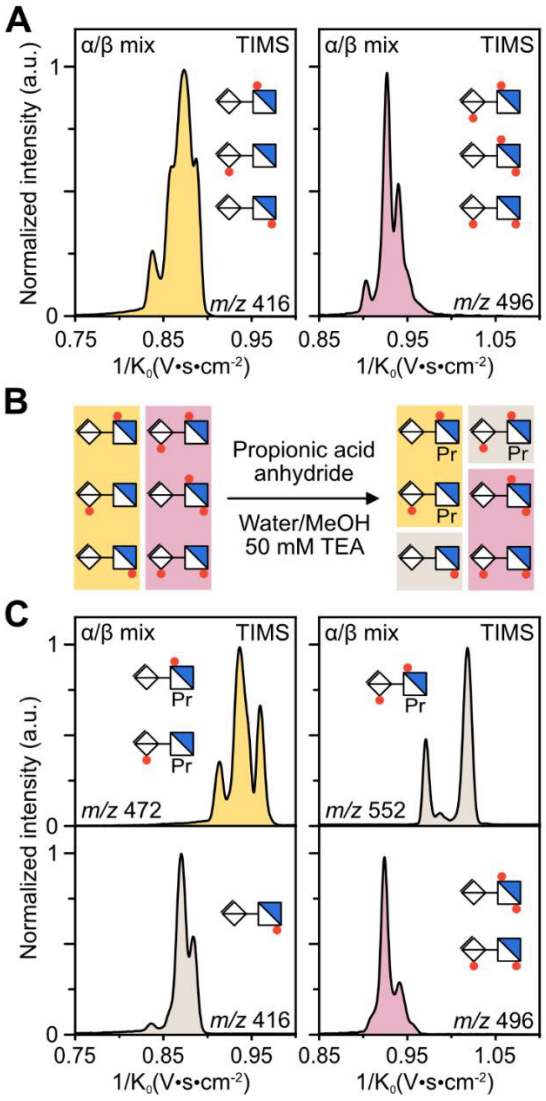

Figure 5.2: Modifications of the disaccharides to reduce complexity. **a)** Equimolar isomeric mixtures of monosulfated (HS-6S, HS-2S, and HS-NS in yellow) and disulfated species (HS-2S6S, HS-6SNS, and HS-2SNS in red) analyzed by TIM-MS. **b)** Selective modifications of primary amines of HS-2S, HS-6S, and HS-2S6S resulting in a 56 Da shift by *N*-propionylation which removes one of each isomer from the mixtures. **c)** TIMS mobilograms of the propionylated mixtures. Multiple peaks are still visible due to the presence of α/β anomers at the reducing-end. However, the modification led to slightly improved separation.

A model mixture containing all twelve standards was generated, to evaluate the separation of a complete set of disaccharides. After *N*-propionylation and reducing-end labelling with procainamide, the mixture was then analyzed by direct infusion TIM-MS. The constituents of the mixture can be readily identified by TIM-MS qualitatively, with all disaccharides ionized as singly charged species. Doubly charged species are only formed by the di- and trisulfated disaccharides. The singly charged species are used for the TIM-MS analysis, due to their better isomer separation. MS analysis of the modified disaccharide mixture reveals nine singly charged signals. Six of these correspond to distinct disaccharides (*m/z* 597, 611, 635, 711, 757,

and 795), while three peaks (*m*/*z* 677, 691, and 715) correspond to pairs of sulfation isomers (Figure 5.3a).

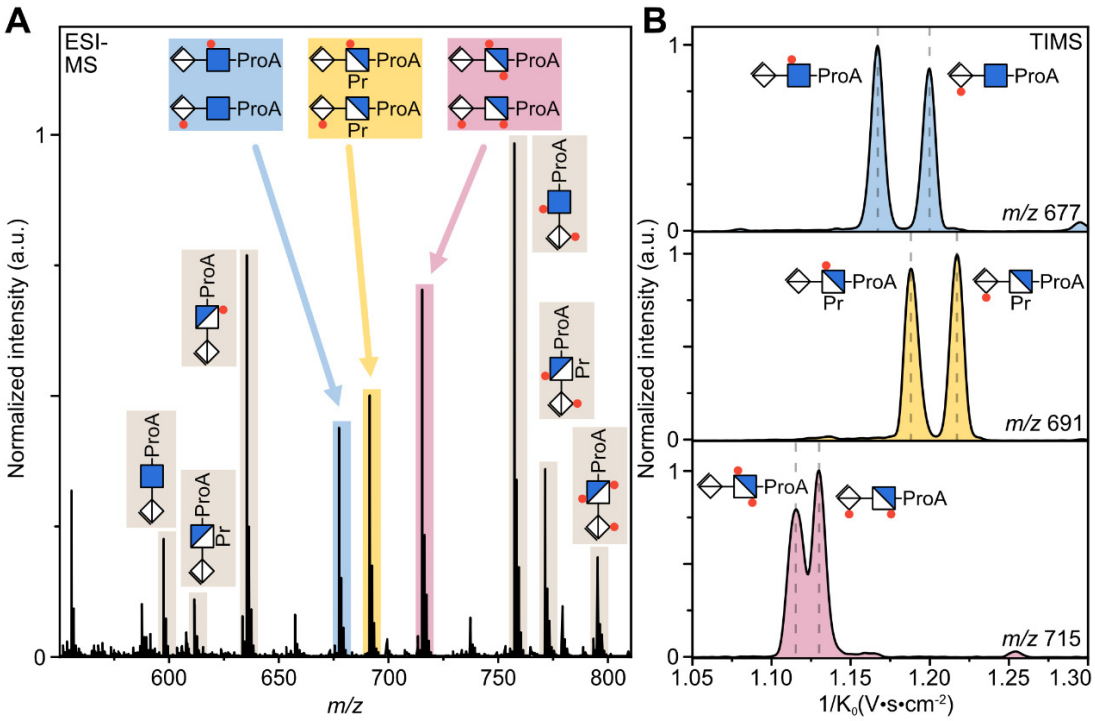

Figure 5.3: Separation of equimolar disaccharide standard mixture. **a)** Negative ion ESI mass spectrum of *N*-propionylated, procainamide labelled disaccharide mixture. The Six non-isomeric disaccharides are labelled in grey and can be distinguished by their *m*/*z* alone. Isomers are present in the coloured peaks. Blue corresponds to HS-2SNAc and HS-6SNAc (*m*/*z* 677), yellow to HS-2SN and HS-6SN (*m*/*z* 691); and red to HS-2SNS and HS-6SNS (*m*/*z* 715). **b)** TIMS mobilograms of the three isomeric disaccharide pairs.

The ion mobilities of the disaccharides in mixture were compared to the ion mobilities of single standards. HS-2SNAc and HS-6SNAc at *m*/*z* 677 show a baseline separation of the species in the extracted TIMS mobilogram (Figure 5.3b, blue). The *N*-propionylated HS-2SN and HS-6SN isomer pair also show a baseline separation, with a slight shift towards lower ion mobilities (Figure 5.3b, yellow). The disulfated isomers HS-2SNS and HS-6SNS can still be separated sufficiently, although no baseline separation is achieved (Figure 5.3b, red). A

common trend in all the isomer separations is that *2O*-sulfated species generally have higher ion mobility than their *6O*-sulfated counterparts, likely due to an interaction of the *6O*-sulfate with the procainamide label which leads to a more compact conformation.

5.2.2 Quantification of TIMS Separated Disaccharides

Reducing-end labelling of the GAG disaccharides provides options for relative quantification during analysis. By utilizing a stable isotope-labelled version of procainamide, a heavy-labelled standard mixture (Appendix A, Figure A2) with known concentrations for each disaccharide can be spiked into a sample and be used for relative quantification of the twelve disaccharides by simple comparison of ion count. Absolute quantification could in principle also be achieved by this method. ^{13}C-labelled disaccharides are also commercially available, but they are very expensive, especially when considering that standards have to be spiked into each sample. Therefore, an advantage is taken of the introduced reducing-end label. To avoid overlapping of isotopic peaks of the internal standard with the sample, especially for the more heavily sulfated species, it's important to choose a label with at least a 5 Da difference. ProA-d10, which is easy to synthesize, was chosen as the heavy label. Figure 5.4a shows a mass spectrum of a ProA labelled HS disaccharide mixture spiked with a ProA-d10 mixture. By comparing the intensity of the ProA labelled sample with the 10 Da shifted ProA-d10 labelled internal standard, we can achieve relative quantification of the sample. For isomeric disaccharides, the TIMS separation discussed earlier is used (Figure 5.4b). Similar to liquid chromatography, the introduction of a heavy label results in a slight shift of mobilities. However, since this shift is significantly smaller than the peak width (<1% shift in mobility), it does not affect the analysis. It's recommended to compare the TIMS $1/K_0$-area of sample and internal standard for all disaccharides, not only for the isomeric structures. The TIMS separation helps accuracy by removing unrelated isobaric species, such as ions with higher charge states, from interfering with the quantification.

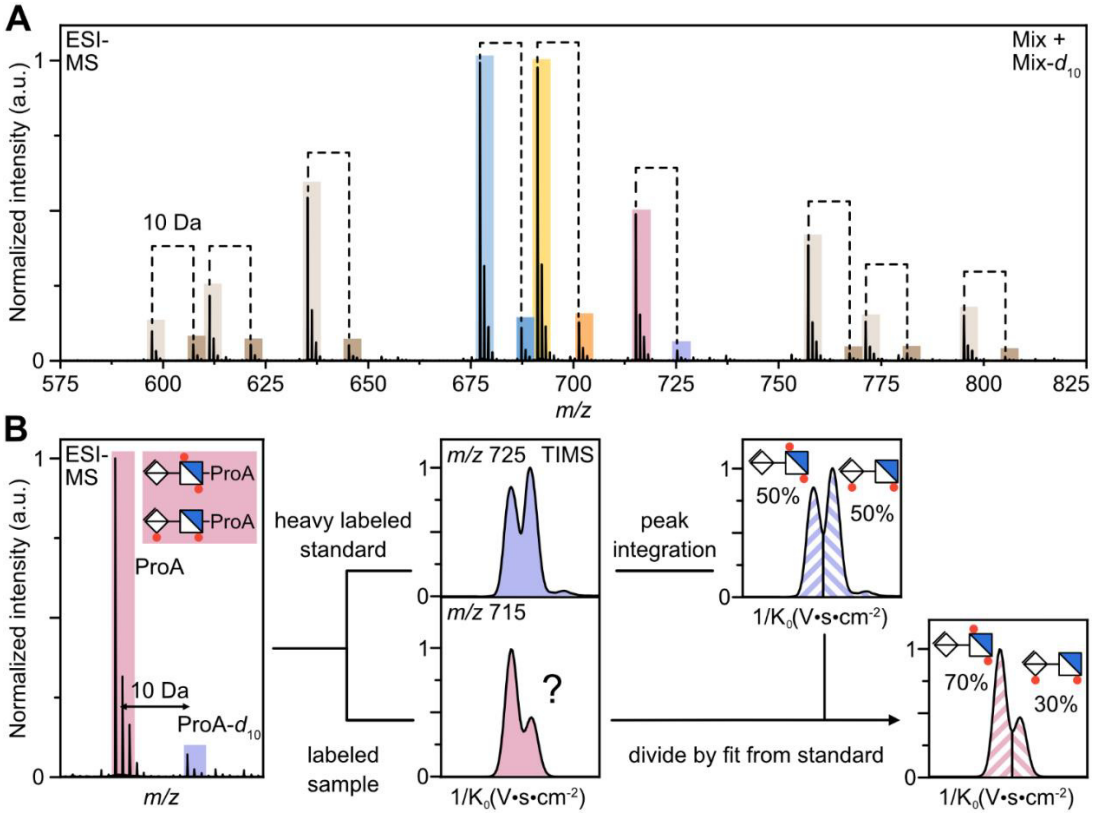

Figure 5.4: Stable isotope labelling for the quantification of isomeric disaccharides using TIM-MS. **a)** Mass spectrum of a disaccharide mixture labelled with ProA, spiked with a ProA-d_{10} labelled disaccharide standard mixture. Dotted lines indicate the 10 Da shifts between the sample and the corresponding internal standard. **b)** Quantification approach for the three isomeric disaccharide pairs based on TIMS. Comparing the integrals of the heavy-labelled standard to those of the sample results in the relative abundance of the respective disaccharide isomers.

Four mixtures were prepared to benchmark the method, representing different HS disaccharide ratios (Figure 5.5, raw data Appendix A, Figure A3-7). The relative abundance of the HS disaccharides ranged from 4.2 to 12.5 %. Propionylation and reducing end labelling were performed as described above, but on the complete mixtures and not on the individual components. After the modifications, the sample was dissolved in an ammonium acetate solution and an equimolar standard disaccharide mixture labelled with ProA-d_{10} was spiked

into the sample. The use of an ammonium-based additive is recommended, as it leads to a more favourable charge distribution towards lower charge states, especially for highly sulphated disaccharides. The quantification of all four mixtures showed a very good agreement between the theoretical and measured relative HS disaccharide content with an average relative error of 5.3 %. A single outlier was observed in mixture 2 for HS-2SN with a relative deviation of 33%. A systematic error in the propionylation or labelling reaction can be excluded since the quantification of HS-2SN in the other three mixtures agrees very well with the expected values. If this value is omitted, the average relative error is 4.7%. The remaining error can be attributed to non-linear detector response rates during MS and the co-elution of unrelated isobaric species.

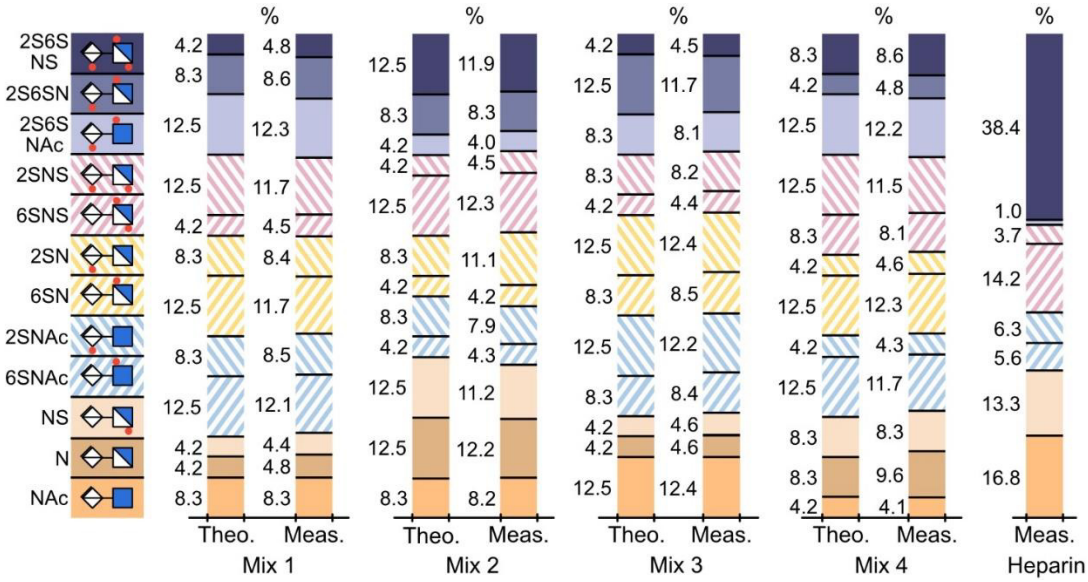

Figure 5.5: Relative quantification of four HS disaccharide mixtures and a heparin sample from porcine intestinal mucosa using ProA-d_{10} labelling of disaccharides. For each mixture, stacked bars are shown for theoretical (left) and measured (right) values; the numbers correspond to the relative content in per cent. The twelve HS disaccharide structures are labelled by their respective colour. Isomeric species are distinguished by the direction of the diagonal stripes. The results of a heparin sample from the intestinal mucosa of pigs, in which a high degree of sulfation was detected, are shown on the far right.

Finally, the TIM-MS quantification method based on direct infusion was applied to a natural heparin sample from the intestinal mucosa of pigs. The heparin was digested with a heparinase I/II/III mixture, freeze-dried and then derivatised according to the protocol described above.

The isomer separation of the mobilograms for the heparin disaccharides is consistent with the mobilograms derived from the standard mixtures. The composition shows a high degree of sulfation, with over 50% of the disaccharides carrying at least two sulfate groups (Figure 5.5 - right). Non- and monosulfated structures are also observed, in particular HS-NAc with a high proportion of 16.8 %. Free amine structures were not identified or only in very small quantities. These results are consistent with other disaccharide studies of heparin.[219]

5.3 Conclusion

The composition and sequence of the GAGs, in particular of heparin and HS, varies from person to person and changes significantly during diseases..[229] A reliable high-throughput method for analysing the heparin/HS composition could enable the creation of profiles of these glycosaminoglycans as potential biomarkers for various diseases. Furthermore, analysing the composition of heparin is crucial for the quality control of heparin-based drugs and would benefit from a reliable high-throughput method.

The analysis of the composition of HS and heparin disaccharides currently involves enzymatic depolymerisation, reducing-end labelling, subsequent LC separation and detection by FLD or MS. Here, a TIM-MS-based method for the rapid separation and characterisation of twelve partially isomeric heparin/HS disaccharides from complex mixtures and biological samples was presented. The analytical workflow, which takes only a few minutes, is a compelling alternative to conventional LC approaches and offers faster and more efficient sample analysis. Compared to conventional LC workflows, the method

involves only a single additional chemical modification step, namely propionylation in combination with reducing-end labelling with procainamide. This significantly reduces the complexity of the mixture, enabling the isomeric structures to be clearly identified and separated during TIM-MS analysis.

The developed method allows the quantification of disaccharides by the addition of an easily accessible stable isotope-labelled internal standard and provides a reliable approach for the evaluation of relative abundances. Benchmarking with spiked mixtures showed excellent agreement between theoretical and measured values. The application of the method to a natural heparin sample from the intestinal mucosa of pigs also emphasises its usefulness for analysing real biological samples. The method developed here is probably also applicable to other high-resolution IMS techniques and instruments, although care should be taken to avoid unwanted ion activation and the resulting fragmentation of the sulfate groups.

5.4 Experimental Section

Chemicals

All chemicals and solvents were purchased from Sigma-Aldrich (St. Louis, USA) and used without further purification. Heparinase enzymes were expressed in-house by Christian Roth. HPLC-grade solvents were used throughout. Heparin sodium from porcine intestinal mucosa was purchased from ABCR (Karlsruhe, Germany); glycan disaccharide standards from Iduron (Cheshire, UK).

Heparin digestion

Heparin digestion was performed by Andreas Zappe. Heparin sodium (100 µg) was suspended in 20 mM Tris / 5 mM $CaCl_2$ / 200 mM NaCl pH 7.0 and incubated at 37 °C. A

Heparinase mixture (10 mU for each Heparinase I, II and III) was added in a total volume of 40 µL and incubated overnight. After incubation, the sample was freeze-dried, dissolved in 500 µL MilliQ water and used without further purification.

Selective amine propionylation

For the propionylation of the mock mixtures and standards, 2 µL of a 1 mM glycan solution was mixed with 8 µL of a freshly prepared 5 vol% propionic acid anhydride in water:methanol:triethylamine (1:1:50 v:v:mM) solution. After one minute reaction time at room temperature, the mixture was frozen in liquid nitrogen and freeze-dried. For the heparin digest 5 µL stock solution (~ 1 µg heparin disaccharides) was used.

Glycan labelling

Glycans were labelled with procainamide according to established protocols (as per Ludger ProA labelling kit).[227, 228] The freeze-dried samples were redissolved in 10 µL water and 20 µL of labelling solution consisting of 16 mg procainamide and 16.4 mg 2-picoline borane reductant dissolved in 150 µL AcOH:DMSO (3:7 v:v) was added. After 3 hours at 50 °C, 250 µL water was added and the samples were freeze-dried and used without further purification. Labelling for the d_{10} standard was carried out in a similar manner but with procainamide-d_{10}.

IM-MS Measurements

For IM-MS analysis samples were dissolved prior to use with water:methanol:ammoniumacetate (1:1:50 v:v:mM) to yield 5-10 µM analyte solutions. The measurements were performed on a Bruker timsTOF Pro in MS negative mode. For ionisation, an in-house build nESI source was used, which was described in detail in chapter 3.2.1[166] per sample ~5 µL were infused. Settings were optimized to prevent unwanted fragmentation with a capillary voltage of 1300 V, end plate offset of -500 V, quadrupole ion

energy of 2.5 V, CID voltage of 7 V, collision gas flow rate of 65%, prepulse storage time 10 µs, transfer time 100 µs. The TIMS parameters are D1: 20 V, D2: 30 V, D3: -100 V, D4: -130 V, D5: 0 V, D6: 50 V. An accumulation time of 20 ms was used. IMS ramping was performed between 0.47-1.61 V*s/cm² with a ramping time of 1000 ms. For $1/K_0$ measurements the instrument was calibrated using the Agilent ESI tune mix. For quantification, Bruker DataAnalysis 5.3 was used to extract $1/K_0$ area values of the given disaccharides and heavy labelled disaccharide standard.

Preparation of procainamide-d_{10}

N-Boc-ethylenediamine (100 mg, 0.62 mmol, 1 eq.) was dissolved in 2 mL of acetonitrile. After addition of DIPEA (272 µL, 1.56 mmol, 2.5 eq.), bromoethane-d_5 (103 µL, 1.4 mmol, 2.2 eq.) was added. The reaction was left to stir at room temperature overnight. After evaporation of the solvents, 1 mL of 30% TFA in DCM was added to the crude product at 0 °C. After addition, the mixture was allowed to warm up to room temperature and subsequently stirred for two hours. The solvent was evaporated, and the product redissolved in 6 mL methanol. *N*-Boc-4-aminobenzoic acid (150 mg, 0.63 mmol, 1.1 eq.) and DMT-MM (250 mg, 0.90 mmol, 1.43 eq.) were added and the reaction was stirred at room temperature overnight. The solvent was evaporated and the Boc-deprotection was carried out again in 1 mL of 30% TFA in DCM at 0 °C and stirred at room temperature for 2 hours. The crude product then was dried and purified a with Biogel P2 gel column (yield ~12%).

6| Intramolecular Rearrangement of Sulfated Glycans

Most MS-based sequencing approaches prerequisite retention of the structure during activation. Isomerisation during activation can therefore hinder an effective elucidation of structure or structural motives. While uncommon in classical glycan analysis, sulfated glycans show two very unexpected rearrangements during thermal activation. Similar to the phosphate migration in peptides, sulfates can shift position during activation. In addition, the anomeric configuration of sulfated glycans is more dynamic than in non-sulfated glycans. In this chapter these rearrangement processes are investigated in depth, utilizing IMS and cold IR-tagging spectroscopy to provide insights into their respective products and mechanisms.

6.1 Introduction

Intramolecular rearrangement or isomerisation processes are common in classical mass spectrometry. Examples are the often-taught McLafferty rearrangement or simple double bond shifts.[230] Since the advent of non-radical ionisation and activation methods they are apparently encountered less frequently. Conversely, a recent study by van Tetering *et al.*[231] showed that rearrangements, even in non-radical ions, might be more common than initially thought. They revealed that many fragments assigned in MS/MS databases are annotated incorrectly, and in reality, are the product of isomerisation, especially cyclisation. Rearrangement processes are also encountered in biopolymers. Peptides can undergo sequence-scrambling through a cyclisation mechanism during fragmentation, making sequencing approaches more difficult.[232-234] A further prominent example is the phosphate migration during analysis of phosphopeptides. Phosphorylation is one of the most common posttranslational modifications of proteins.[235] During CID activation, which is very commonly applied in peptide analysis, phosphate groups can change position along the peptide chain, leaving the original site of modification ambiguous.[236, 237]

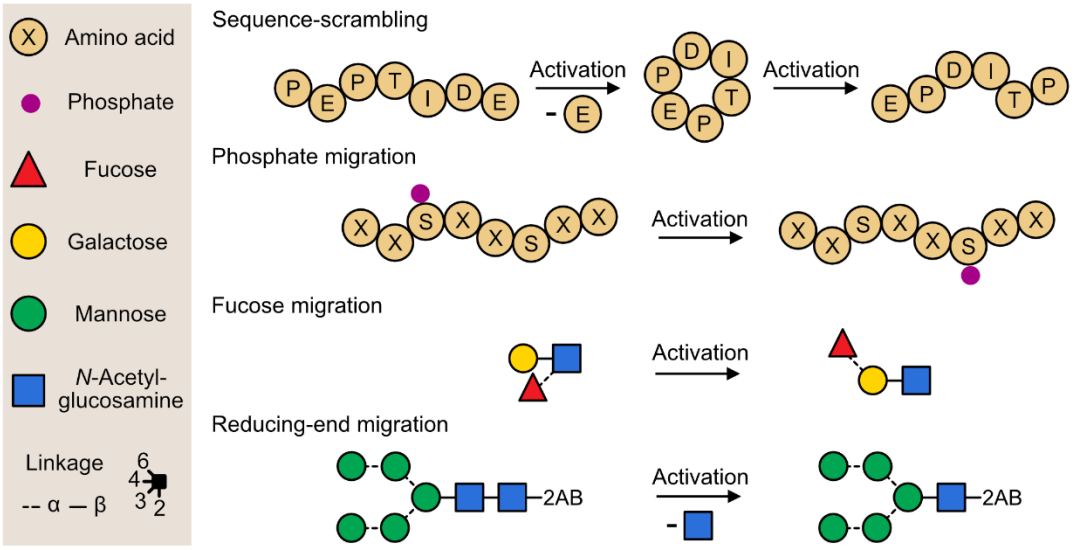

Figure 6.1: List of known biopolymer rearrangement reactions. Peptides can undergo sequence-scrambling and in the case of phosphorylated peptides, phosphate migration. For glycans, the migration of fucose and reducing-end sugars was observed.

In glycan analysis, fucose migration, also known as internal residue loss, remains a mystery to this day. Kováčik *et al.*[238] showed that during fragmentation of a fucose-containing oligosaccharide, glycans in between the fucose and the reducing-end would fragment off, leaving the fucose directly attached to the reducing-end glycan. Later it was shown that the fucose changes position during activation at much lower activation energies than classical glycosidic bond breakages.[239, 240] Neither the position of the migrated fucose nor the migration mechanism are fully understood yet and are still subjects of research.[241-243] For high mannose N-glycan structures Wuhrer *et al.*[244] showed that a reducing-end labelled GlcNAc residue can migrate onto the mannose antennas, leading to the loss of a core GlcNAc. A schematic representation of these rearrangement processes can be seen in Figure 6.1.

While none of the described mechanisms are expected during the analysis of sulfated glycans, two unique rearrangement reactions were observed for GAGs. Here we explore these isomerisation reactions specific to sulfated glycans in the gas phase, giving insight into the isomerisation products and possible rearrangement mechanisms.

6.2 Results and Discussion

6.2.1 Sulfate Migration in Sulfated Glycans

The CID fragmentation of singly charged HS2SNAc-ProA in negative MS mode results in an unexpected MS/MS spectrum (Figure 6.2a). Apart from expected fragments form such as the Y_1 fragment at *m*/*z* 439 and a cross ring $^{0,2}X_1$ fragment at *m*/*z* 579, additionally the dehydrated fragments at *m*/*z* 421 and 561 are observed respectively. An unexpected fragment at *m*/*z* 519 is formed. The mass difference of this fragment to the Y_1 fragment is ~80 Da which equals the common in GAG MS-analysis observed shift due to a sulfate modification ($+SO_3$). Since the sulfate of the used standard is linked to the *2O*-position of the uronic acid, a sulfated Y_1 fragment should not be possible under normal conditions. This unexpected fragment could be the result of a sulfate migration process, where the sulfate migrates from the uronic acid to the neighbouring GlcNAc residue. Possible sulfate acceptors are likely the hydroxyl groups, but also the amides of GlcNAc and the used label, procainamide.

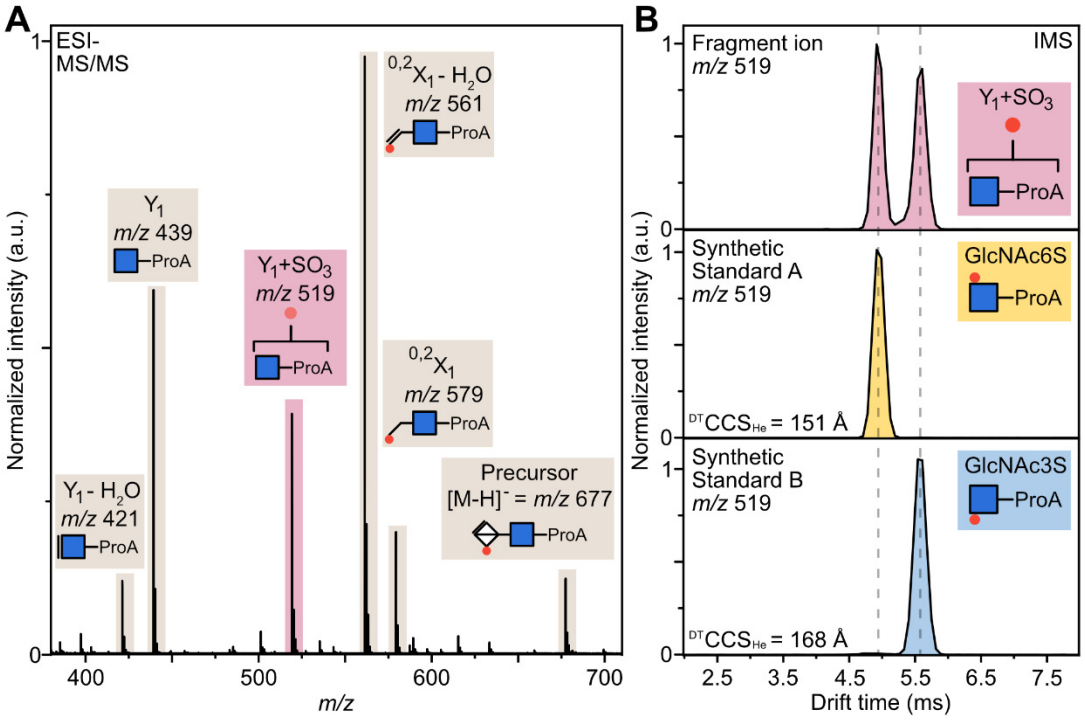

Figure 6.2: Fragmentation of HS2SNAc-ProA. **a)** CID-MS/MS of HS2SNAc-ProA. Besides expected fragment ions (grey), an unexpected Y_1+SO_3 ion (red) is formed through sulfate migration. **b)** ATDs of the Y_1+SO_3 fragment ion (red) and two standards, GlcNAc6S-ProA (yellow) and GlcNAc3S-ProA (blue).

To gain deeper insight into this fragment CID-IM-MS experiments were performed (Figure 6.2b). The ATD of the Y_1+SO_3 fragment revealed two major peaks with roughly equal intensity (Figure 6.2b, red). This indicates that several positions act as sulfate acceptors during the migration process. To reveal the sites of migration two GlcNAc-ProA standards were synthesised, which are either sulfated at the *6O*- or *3O*-position. A comparison of the ATDs of the two standards to the Y_1+SO_3 fragment of HS2SNAc-ProA shows a very good agreement. GlcNAc6S-ProA shows an exceptionally good fit to the compact peak of the Y_1+SO_3 fragment at ~4.4 ms (Figure 6.2b, yellow), while GlcNAc3S-ProA fits the extended peak at ~5.6 ms (Figure 6.2b, blue).

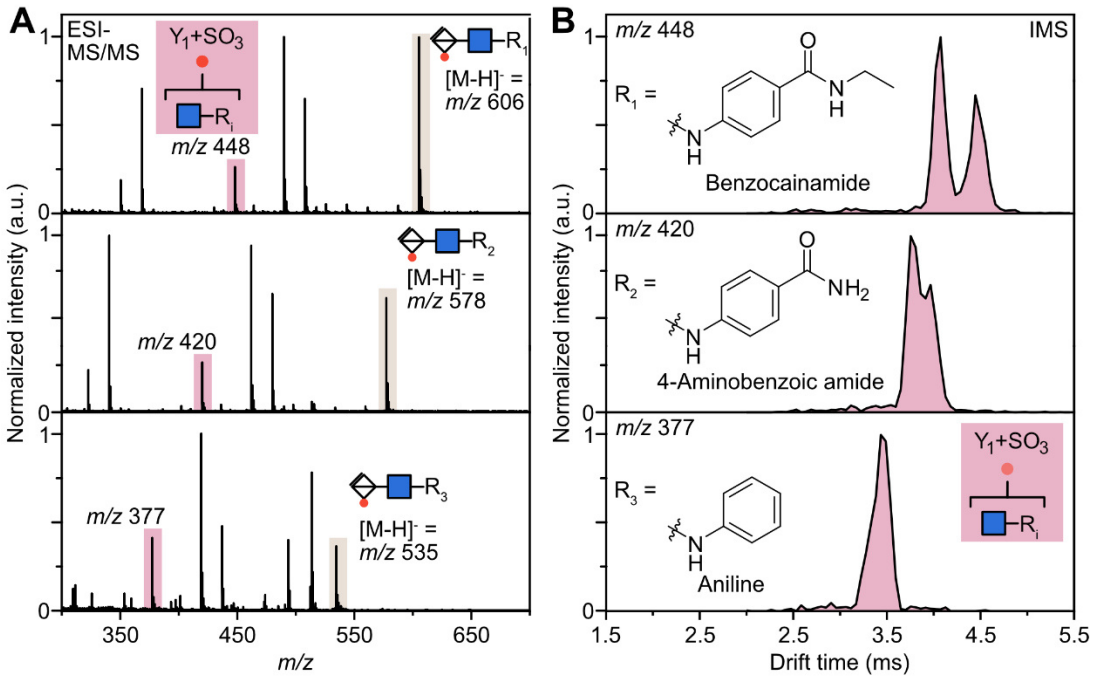

Figure 6.3: Fragmentation of HS2SNAc labelled with three alternative reducing-end labels. **a)** CID-MS/MS spectra of benzocainamide, 4-aminobenzoic amide and aniline labelled HS2SNAc. The extent of Y_1+SO_3 fragment formation is similar. **b)** ATDs of the Y_1+SO_3 fragments. Sulfate migration sites appear to be constant, but differentiability is reduced.

To investigate the influence of the label as a cause of this migration process, HS2SNAc was labelled with three additional reducing-end labels: benzocainamide, 4-aminobenzoic amide, and aniline. These labels were chosen to step-wise reduce the functionality of the label and observe any change in the extent of the possibly connected migration process. Benzocainamide is similar to procainamide, only missing the tertiary amine at the ethylamide. 4-Aminobenzoic amide is missing the ethylamide present in benzocainamide, and lastly, aniline, which is missing almost all functionalities. At identical instrumental conditions the extent of the Y_1+SO_3 migration product formation remains comparable (Figure 6.3a). Hence, the formation of the sulfated Y_1- fragment is not dependent on the type of reducing-end label. Slight changes in intensity can be explained by the mass-dependent energy transfer efficiency during the CID process, which is also visible in the relative precursor intensity. To examine a possible influence on migration sites, again CID-IM-MS

experiments were performed (Figure 6.3b). The benzocainamide labelled species showed a very similar ATD as the ProA labelled one. The peaks appear less resolved and are shifted towards lower drift times, but qualitatively match with the previous results. The 4AB labelled glycans showed a drastically reduced differentiability between the migration sites, with two peaks still clearly visible but less resolved. Lastly, the aniline-labelled glycan follows the observed trend. Merely a shoulder is visible in the ATD of the Y_1+SO_3 migration product for the second migration site. Therefore, the utilized label does not influence the migration process, neither quantitative nor qualitative but can be crucial for differentiation of migration sites.

To follow the formation of the fragment of interest, energy-resolved IMS measurements were performed (Figure 6.4a, left). The ATD of the Y_1 fragment is recorded at step-wise increasing collision voltages in the CID cell. Surprisingly, the two migration products form at slightly different rates. The formation of GlcNAc3S-ProA occurs preferably at a higher collision voltage compared to the formation of GlcNAc6S-ProA. This is especially obvious when the survival yield curves are compared (Figure 6.4a, right). At a collision voltage of 40 V the relative intensity of GlcNAc6S-ProA reaches its maximum. Compared to that, GlcNAc3S-ProA reaches its maximum at 42 V. This leads to an inversion of the relative intensities of the two migration products at 44 V, with more GlcNAc3S-ProA present than GlcNAc6S-ProA. This effect could be caused either by a difference in fragment formation or by a difference in fragment stability in the gas phase. The two synthetic standards show identical survival yields (SY_{50}) with 36.7 V for the 3S and 6S compounds. (Appendix B, Figure B1). Therefore, it can be concluded that the formation of GlcNAc3S-ProA is preferred at higher collision voltages.

This intriguing difference in fragment formation gives insight into a possible sulfate migration mechanism. The intramolecular nature of this process suggests an S_N2-type mechanism. An S_N1-type mechanism would require first a neutral loss of SO_3 and a subsequent nucleophilic attack by a hydroxyl or amine group. In high vacuum conditions, this is likely not the case, especially not in the observed extent.

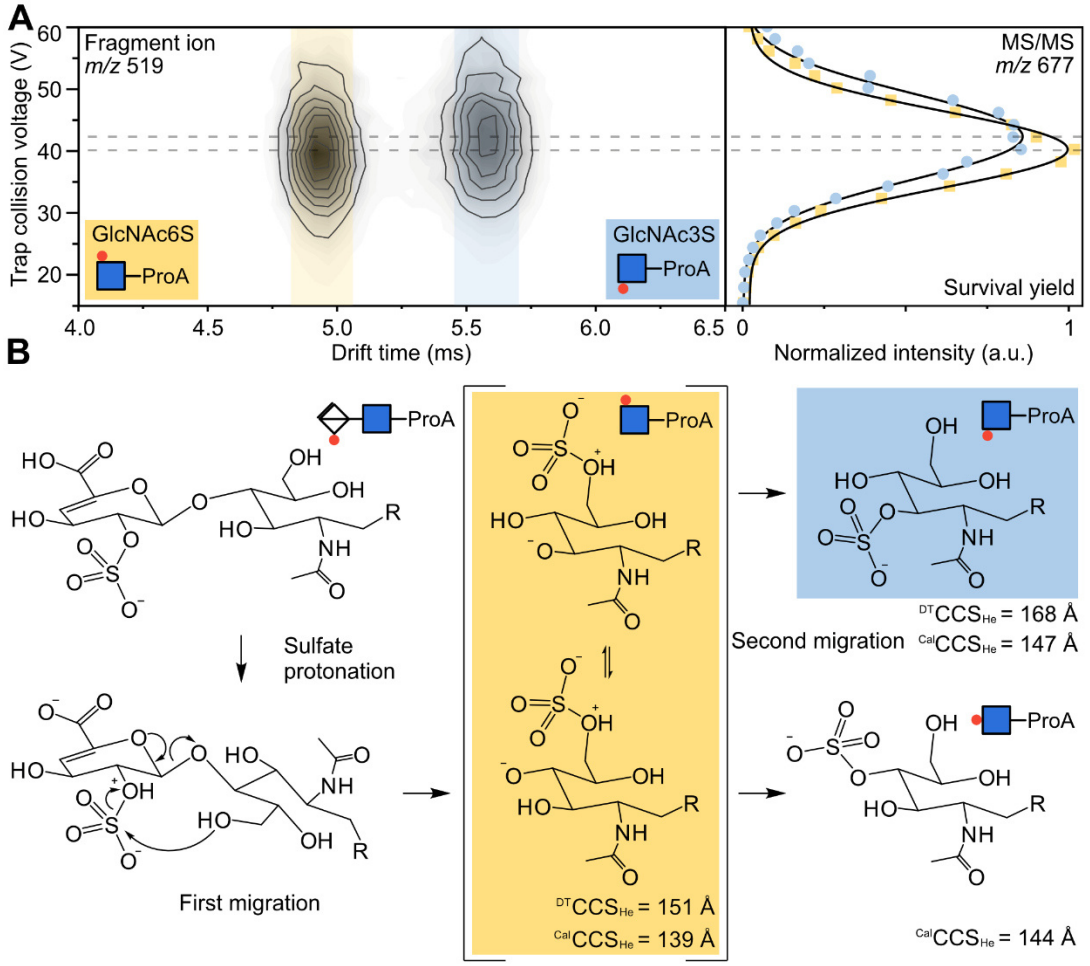

Figure 6.4: Energy resolved CID measurements of HS2SNAc-ProA. **a)** Energy resolved IMS heat-map (left), a delay in the formation of GlcNAc3S in comparison to GlcNAc6S is seen. Survival yield curves (right), highlighting the delay. **b)** Proposed sulfate migration mechanism in HS2SNAc-ProA.

An S_N2-type mechanism is proposed in Figure 6.4b. This mechanism relies on the presence of an acidic/mobile proton. Mobile protons are known to play a crucial role in other gas-phase migration processes, such as the fucose migration.[240] Additionally, the previously discussed formation energy differences of both migration products indicate a multistep process. The proposed mechanism involves a proton transfer to the sulfate group in its first step. This activated sulfate is then attacked by the flexible *6O*-position of the neighbouring glycan. Surprisingly, HS2SNAc-ProA shows no signs of migration prior to Y_1-fragment formation

(Appendix B, Figure B2), therefore a concerted mechanism is assumed, where sulfate migration and glycosidic bond breakage happen simultaneously.

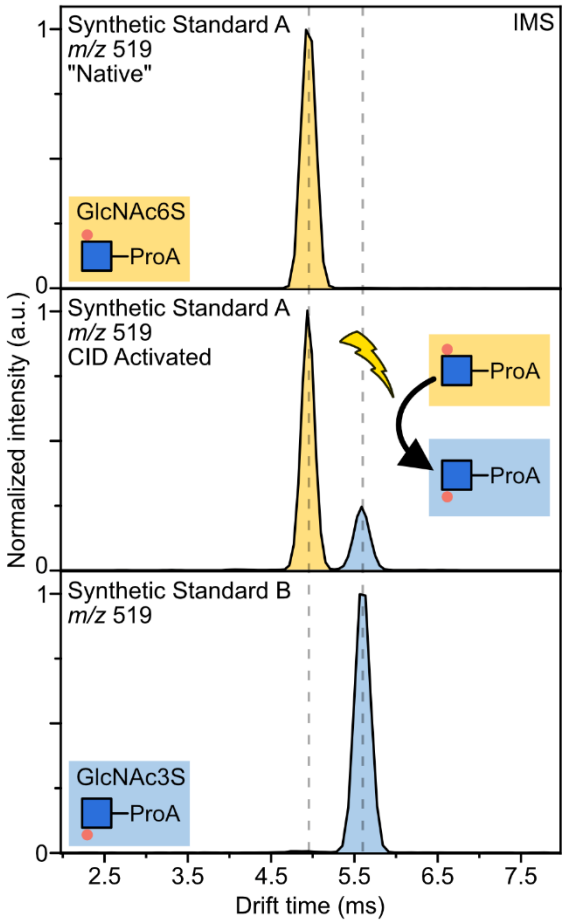

Figure 6.5: ATDs of GlcNAc6S-ProA and GlcNAc3S-ProA. Activation of the GlcNAc6S standard leads to formation of GlcNAc3S.

In the first step, glycosidic bond fragmentation and sulfate migration result in the formation of GlcNAc6S-ProA, still in its active, protonated form. In the second step, migration onto the *3O*-position can occur. A migration to the *4O*-position of the glycan was also considered but could not be identified due to the lack of a suitable standard. Therefore, the Marianski Group at Hunter College (NY, USA) performed CCS calculations on the measured and missing standards. The calculated CCS values for the three migration sites are $^{Cal}CCS_{He}(6S)$ = 139 Å, $^{Cal}CCS_{He}(3S)$ = 147 Å and $^{Cal}CCS_{He}(4S)$ = 144 Å, the CCS values from DT-IMS measurements are $^{DT}CCS_{He}(6S)$ = 151 Å and $^{DT}CCS_{He}(3S)$ = 151 Å. The calculated CCS values differ substantially from the CCS values extracted from DT-IMS measurements, but the general

trend matches. Importantly the CCS values of *3O*- and *4O*-sulfated GlcNAc-ProA are very similar. Therefore, the possible formation of GlcNAc4S-ProA cannot be dismissed.

While HS2SNAc-ProA shows no signs of migration prior to fragmentation, the step-wise nature of the migration process can be confirmed by monitoring the drift time of the GlcNAc6S-ProA standard during CID activation (Figure 6.5). The GlcNAc6S-ProA standard does not contain a classical mobile proton, a migration during activation is nevertheless observed. The mobility of protons from hydroxyl groups seems to suffice to induce migration, although to a lower extent when compared to the migration during HS2SNAc-ProA fragmentation. The overall extent of migration is CID voltage-dependent with higher voltages leading to more relative migration (Appendix B, Figure B3). The drift time of the migrated product matches the drift time of the GlcNAc3S-ProA standard, confirming the migration site.

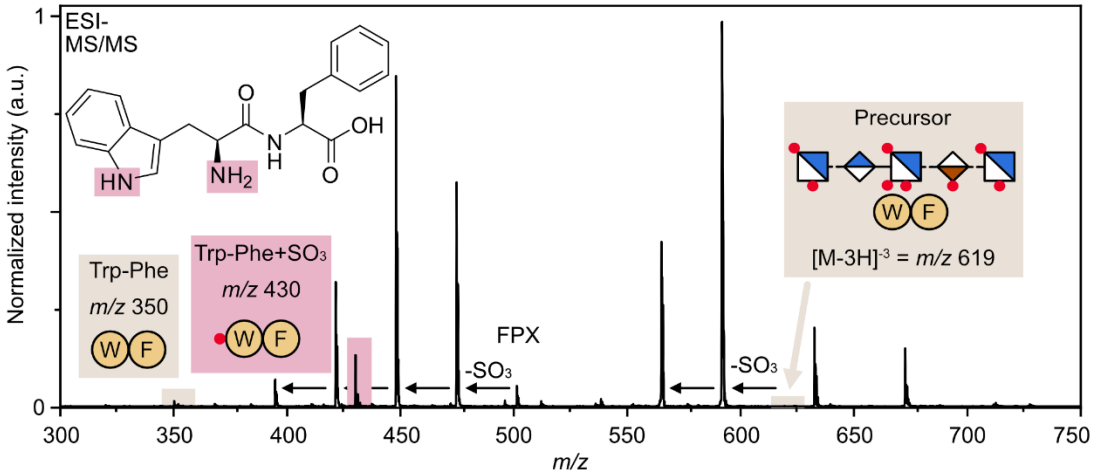

Figure 6.6: Intermolecular sulfate migration from FPX to a tryptophan-phenylalanine dipeptide. Dissociation of the non-covalent FPX-dipeptide complex leads to a migration of a sulfate group from the FPX to one of the two sulfate acceptor sites in the dipeptide.

Interestingly, sulfate migration can also occur intermolecularly. When forming a non-covalent complex between the highly sulfated pentasaccharide FPX and the dipeptide tryptophan-phenylalanine (Trp-Phe), and then dissociating it in the CID cell, a sulfate can be transferred from the FPX to the dipeptide (Figure 6.6). Remarkably, the intensity of the

sulfated dipeptide at *m*/*z* 430 is considerably higher than the intensity of the native dipeptide at *m*/*z* 350. Two expected migration sites are present in the dipeptide. IMS analysis of the sulfated dipeptide only shows a single peak in the ATD making the assignment nonconclusive. This migration in non-covalent FPX complexes is also visible in chapter 4 of this thesis. Figure 4.3d shows the dissociation of the FPX-Gadobutrol complex. Unlike the other contrast agents, Gadobutrol contains three hydroxyl groups acting as sulfate migration acceptors during dissociation. Therefore, an although small, but visible peak at *m*/*z* 529 is seen.

The high MS intensity of the sulfate-migrated peaks is likely governed by their respective tendency to hold a negative charge during formation. This is true for both intra- and intermolecular sulfate migration. Therefore, the sulfate-migrated peaks often show a higher intensity than their non-sulfated counterparts. In the case of the triply charged FPX-dipeptide complex the main fragmentation path, besides the loss of a sulfate, is the dissociation into the triply charged FPX. Most of the dipeptide formed during fragmentation, therefore holds no charge. The extent of sulfated dipeptide after migration is unknown. Nevertheless, being unaware of sulfate migration can lead to false structural assignment, when ignoring the possibility of sulfate migration during activation. This is especially true for lowly sulfated species common in e.g. *O*- or *N*-glycan analysis.

6.2.2 Gas-Phase Mutarotation of Sulfated Glycans

During the analysis of sulfated glycans, another unexpected reaction was observed in the gas phase. GlcNAc6S and GalNAc6S were investigated utilizing IMS and gas-phase IR spectroscopy. GlcNAc6S and GalNAc6S are the most common sulfated monosaccharides in complex glycans such as *O*- and *N*-glycans or GAGs, therefore a change of the structure during activation can have tremendous implications for their respective gas-phase analysis.

Measuring GlcNAc6S with TIM-MS in negative ion mode led to unexpected results. Depending on the utilized TIM-MS setting, one or two ion mobility peaks were observed (Figure 6.7a). Increasing the harshness of the TIMS cell by either increasing the accumulation or scanning time led to an increase in the relative intensity of the compact species. This is

most likely attributable to RF heating effects during both the accumulation and scanning stage of the TIMS cell. But nevertheless, the timescale for this process is remarkably slow. A near-full conversion is only achieved with an accumulation time of a second.

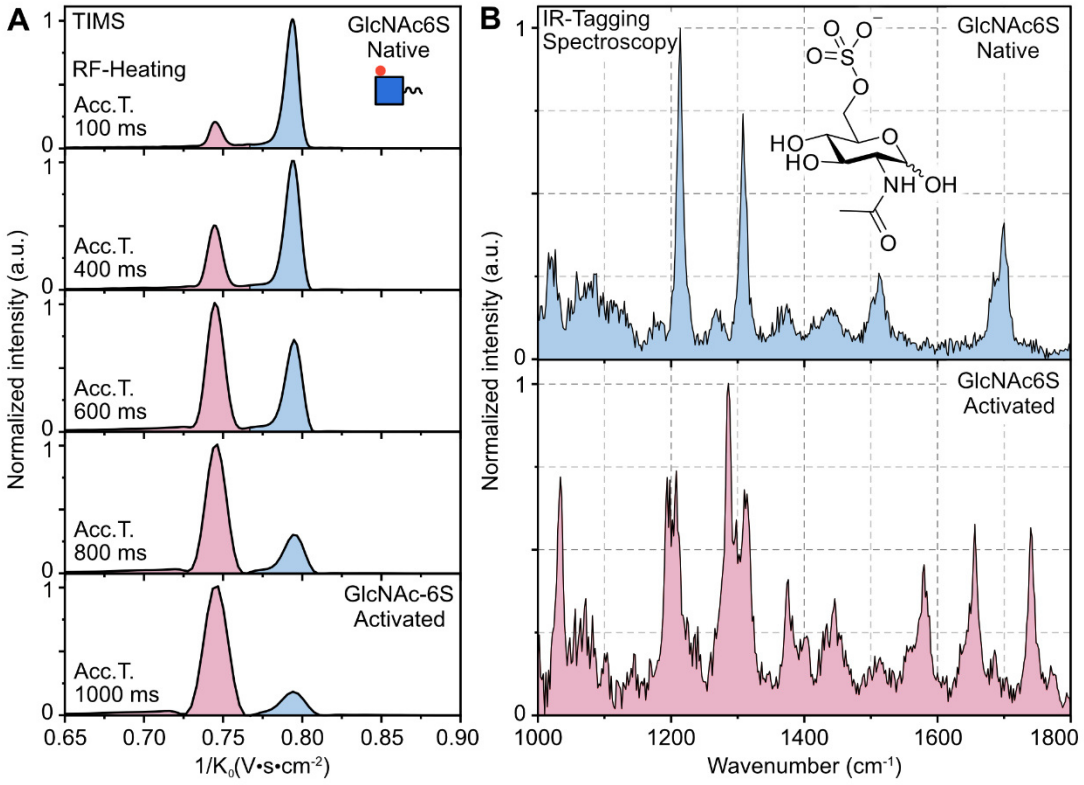

Figure 6.7: Gas-phase TIM-MS and IR measurements of GlcNAc6S. **a)** TIMS mobilogram of GlcNAc6S at different accumulation times. A slow conversion from an extended (blue) to a compact (red) species is seen. **b)** IR-tagging spectra of the size and mass selected GlcNAc6S species. The extended native (blue) and the compact activated (red) GlcNAc6S show considerable spectral differences.

Interestingly, this conversion is also observed when keeping the accumulation and scanning time constant but increasing the dry gas temperature instead (Appendix B, Figure B4).

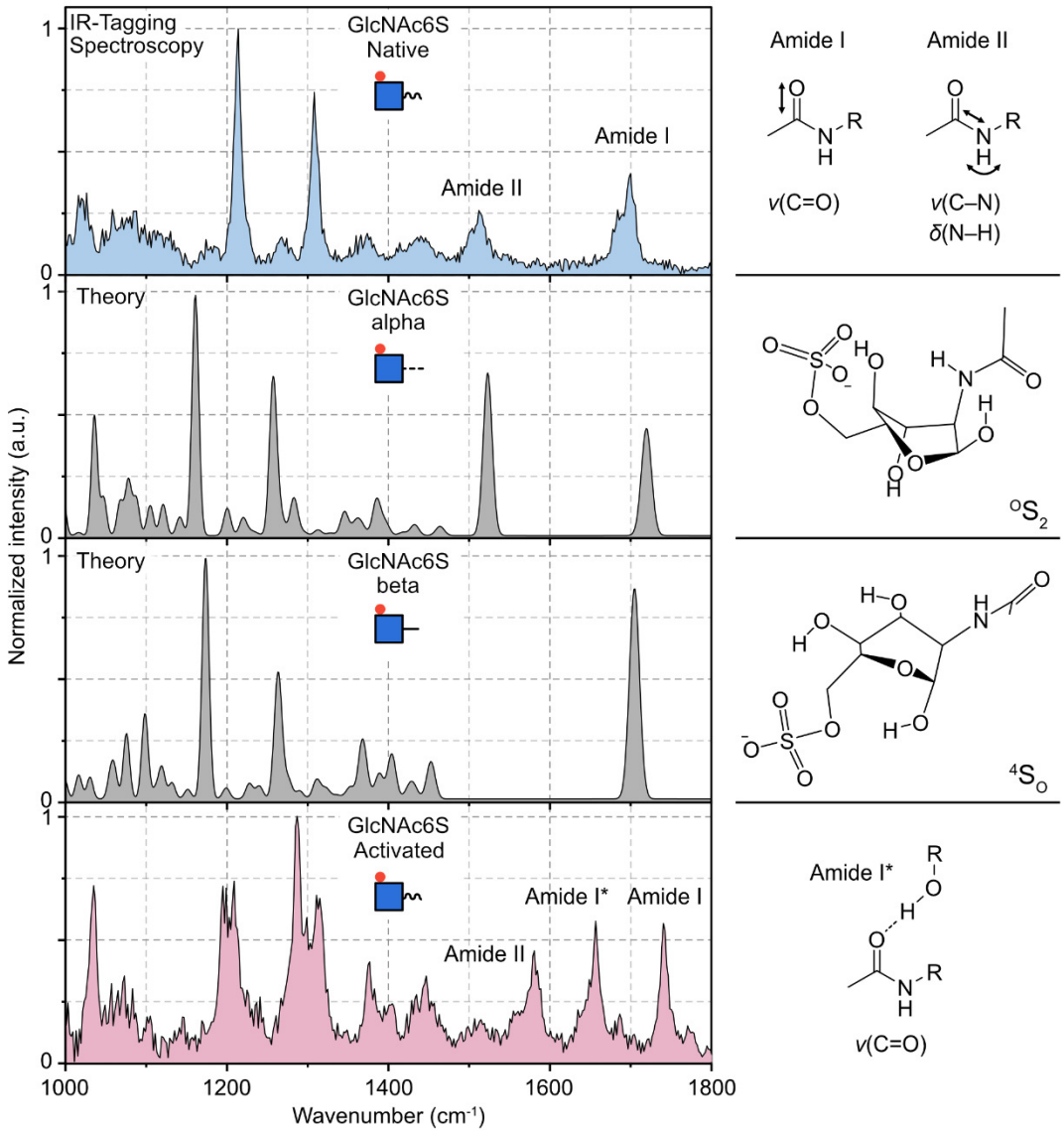

Figure 6.8: Comparison of computed IR spectra of the α and β anomer of GlcNAc6S to the measured spectra. The combination of both computed spectra matches the IR spectrum of the native GlcNAc6S. Major spectral differences to the activated GlcNAc6S are seen in the range of the amide I and II bands.

A similar conversion occurs for GalNAc6S, likely undergoing the same change in structure (Appendix B, Figure B5). It is unclear what type of conversion happens, especially since gas-phase conformers of deprotonated sugars have never been reported before. Charge isomers could be a reason, but the negative charge is likely localised to the sulfate group. The

distance between the two peaks is remarkably similar to some of the α/β anomers of GAG disaccharides observed in Figure 5.2c indicating a possible connection. To investigate the species further, gas-phase tagging IR spectroscopy was performed utilizing a DT-IM-MS instrument on the *m*/*z* and size-selected species (Figure 6.7b). Spectroscopy was performed in the wavenumber range of 1000-1800 cm^{-1}. By activating GlcNAc6S in the ion funnel before DT-IMS separation, a similar conversion as during timsTOF analysis is achieved (Appendix B, Figure B6). The IR spectra of native and activated species show considerable differences. Spectral differences are especially visible between 1500-1800 cm^{-1} where the amide bond vibrations are commonly observed.[245] Two of the main common amide bond vibrations are the amide I and amide II vibrations, mostly known from protein analysis. The Amide I band is mostly constituted from the stretching vibration of the carbon-oxygen double bond (*v*(C=O)), while the amide II band is a combination of the carbon-nitrogen stretching vibration (*v*(C-N)) and the nitrogen-hydrogen bending vibration (δ(N-H)). DFT calculations were performed by Dr. Chun-Wei Chang (FU Berlin) to elucidate the structures of the two species (Figure 6.8). Both α- and β-anomers were calculated since both are likely present in the gas phase. Interestingly, both anomers form skew-boat conformations in the gas phase, $^{O}S_{2}$ and $^{4}S_{O}$ for the α- and β-anomers respectively. The theoretical spectra of α- and β-anomers look remarkably similar to each other, major spectral differences are present in the range of the amide bond vibrations. The native GlcNAc6S spectrum seems to be a combination of the calculated α- and β-anomer spectra. Especially the relative intensity of the amide I and II bands are reproduced through this. The vibration of the sulfate group seen at 1210 and 1305 cm^{-1} respectively are red-shifted in the calculated spectra which could be due to the harmonic approximation of the oscillators. The spectrum of the activated GlcNAc6S shows two absorption bands in the range of the amide I vibration. These two vibrations indicate that more than one structure is present in the size and mass selected species. The amide I band at 1740 cm^{-1} is in an expected range, also seen in the DFT calculated spectra. The amide I* band at 1650 cm^{-1} on the other hand is significantly red-shifted. This can be a result of a weakened C-O double bound through a hydrogen bond to the carbonyl group.

IR tagging spectroscopy in combination with DFT calculation revealed the structure of the native GlcNAc6S species, but the structure of the activated GlcNAc6S species still remains

unknown. The previously discussed sulfate migration should be considered as a cause for the change in IR absorption and IMS mobility. Therefore, DFT calculations of the two possible migration products were performed, GlcNAc4S and GlcNAc3S.

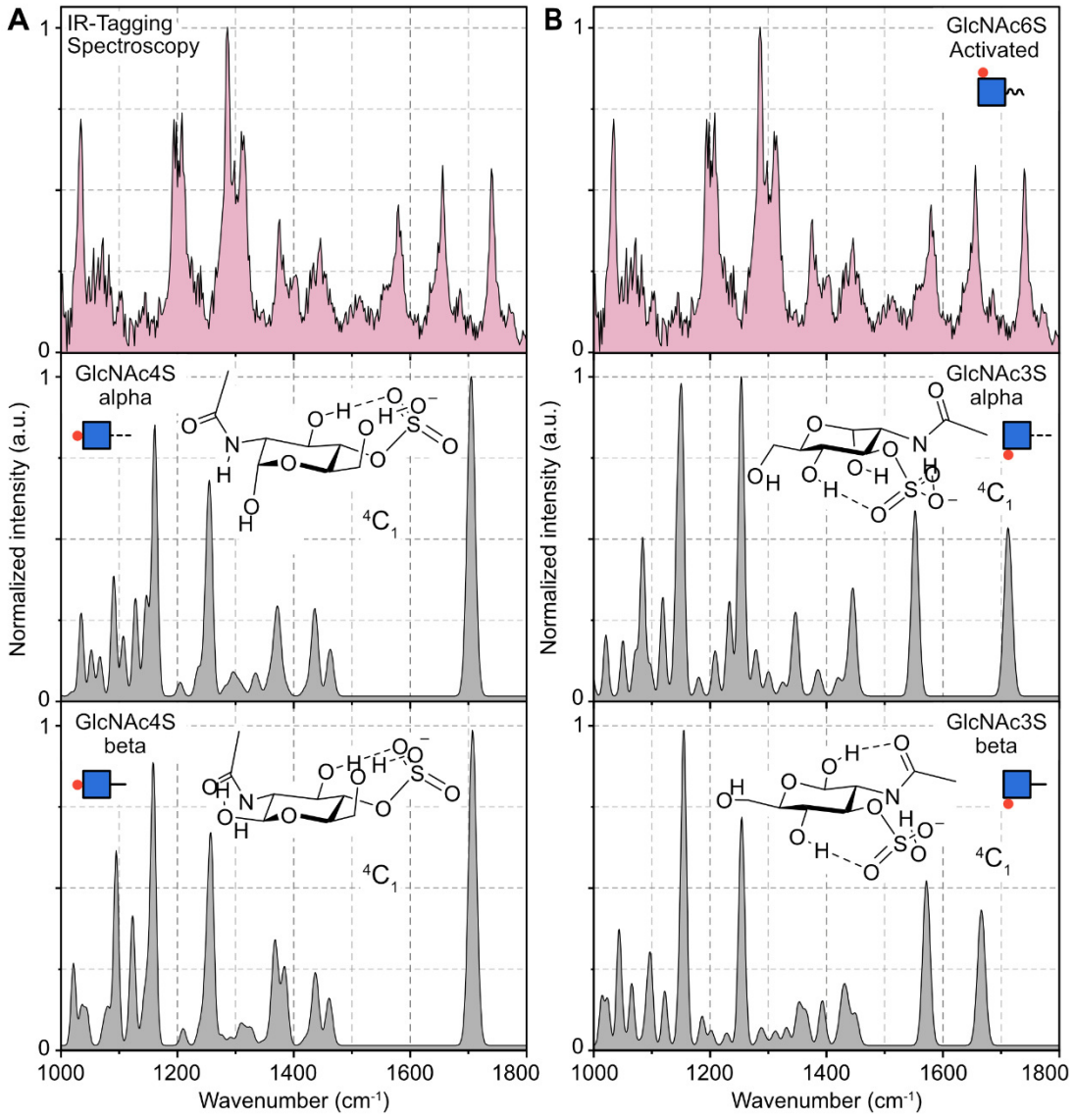

Figure 6.9: Comparison of computed spectra for the sulfate migrated products, **a)** GlcNAc4S and **b)** GlcNAc3S, to the activated GlcNAc6S spectrum. A poor spectral match is seen for GlcNAc4S, but GlcNAc3S shows a promising match in the amide band region.

The spectra were calculated for α- and β-anomers. For GlcNAc4S both anomers form a classical $^4C_1$ chair conformation, stabilized by hydrogen bonds from the hydroxyl groups at

C3 and C6 to the sulfate group. The spectral match of GlcNAc4S to the activated GlcNAc6S species is poor (Figure 6.9a). The amide bands are not replicated and the relative intensities of the sulfate vibrations at 1200 and 1300 cm^{-1} respectively are not reproduced. Additionally, the strong absorption band at 1030 cm^{-1} is not present in either spectrum. The DFT-calculated spectrum of GlcNAc3S on the other hand shows a better fit. Similar to GlcNAc4S, GlcNAc3S forms $^4C_1$ chair conformations but is instead stabilized by the hydroxyl group at C4 and the neighbouring amide to the sulfate group. This hydrogen bond twists the amide into a position which allows the β-anomer to form a hydrogen bond with the amide carbonyl group, giving an amide I* band. The α-anomer does not form this hydrogen bond and instead shows a non-shifted amide I vibration.

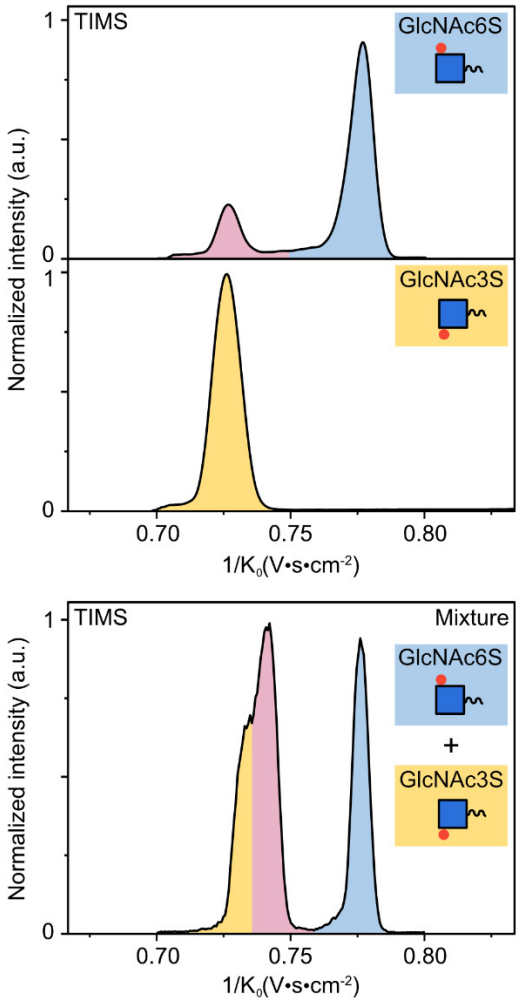

Figure 6.10: TIMS mobilograms of GlcNAc6S (blue/red) and GlcNAc3S (yellow; top). A mixture of both components shows a clear difference in mobility between the activated GlcNAc6S and GlcNAc3S (bottom).

Overall, this replicates the three amide vibrations seen in the activated GlcNAc6S spectrum. The sulfate bands while shifted as in the other cases also do not fully replicate the measured relative intensities. As with GlcNAc4S, the absorption band at 1030 cm^{-1} is not seen. Nevertheless, the partial spectral match could indicate a sulfate migration to the *3O*-position. To Investigates this further TIM-MS measurements on GlcNAc3S (Figure 6.10) were performed. Interestingly, GlcNAc3S does not show a trapping time-dependent change in mobility as GlcNAc6S does. The mobility of GlcNAc3S and the activated GlcNAc6S look remarkably similar. But when measured out of a mixture of both components, a small but noticeable difference in mobilities of activated GlcNAc6S and GlcNAc3S is seen. Therefore, it can be concluded that sulfate migration is not the cause of this rearrangement.

A different famously known glycan rearrangement reaction, in the solution phase, is the mutarotation. There, the cyclic hemiacetal, present in glycans, opens and reforms again, leading to the dynamic nature of the anomeric centre and an equilibrium between alpha, beta, and open ring form. Hexoaldoses, such as GlcNAc6S can recyclize to a six-membered pyranose and also to the less common five-membered furanose ring. It is generally accepted that mutarotation is not present in glycans isolated in the gas phase. Schindler *et al.*[246] showed that upon fragmentation of an oligosaccharide, the formed C-fragments retained their reducing-end configuration. Probed molecules exclusively consisted of hexoses. Pellegrinelli *et al.*[247] confirmed this for *N*-acetylated hexosamines. A simple glycosylation reaction, e.g. with methanol, can stop this rearrangement. To investigate a possible influence of this rearrangement, such a glycosylation was performed here under acid catalysis which is known to also promote furanose formation (Figure 6.11a).[248, 249] The TIM-MS analysis of the reaction product indeed reveals four peaks in the mobilogram, likely corresponding to the respective α- and β-anomers of pyranose and furanose form (Figure 6.11b). None of the methylated products showed activation-dependent conversion such as GlcNAc6S, confirming the involvement of the anomeric centre in the observed rearrangement reaction. The relative change in mobility seen for GlcNAc6S-Me between furanose and pyranose form also matches the difference seen for native and activated GlcNAc6S (~0.05 $V*s*cm^{-2}$). To confirm this assignment further, IR spectra were computed for the α- and β-anomer of the furanose form of GlcNAc6S (Figure 6.11c). Similar to GlcNAc3S, the structural motive of the hydrogen-

bonded amide carbonyl is replicated in the α-anomer. This leads to the shifted amide I* band seen in the recorded spectrum.

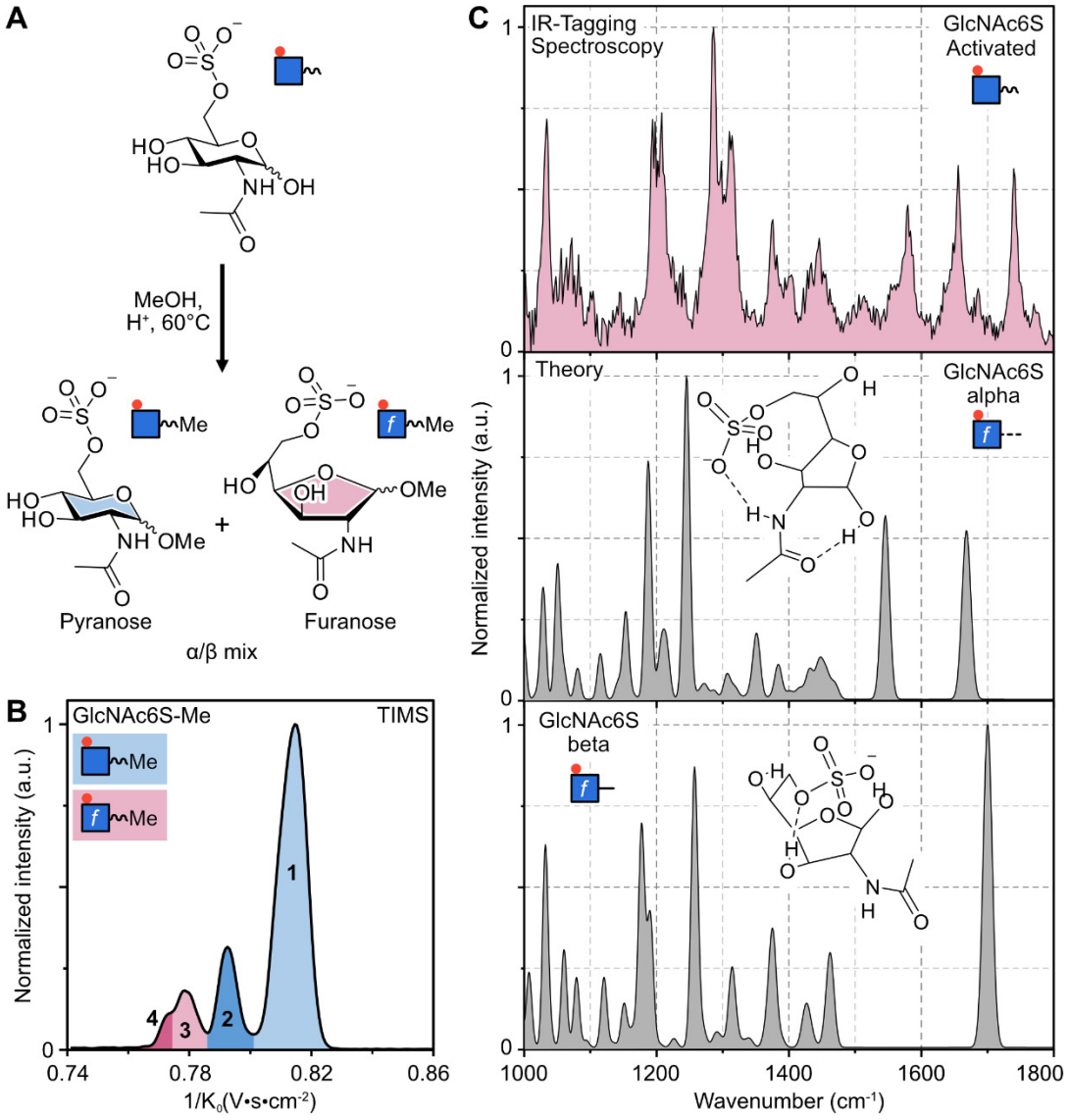

Figure 6.11: Alternate rearrangement reaction of glycans, formation of a five-membered ring, the furanose form. **a)** Glycosylation of GlcNAc6S with methanol under acid catalysis leads to a mixture of α and β anomers of the pyranose (blue) and furanose (red) form. **b)** α and β anomers of pyranose and furanose GlcNAc6S can be observed using TIMS. **c)** The spectrum of activated GlcNAc6S shows a good match with computed spectra of α and β GlcNAc6S-furanose.

This hydrogen bond is not present for the β-anomer resulting in two amide I bands assuming a mixture of both anomers. The relative intensities of the sulfate bands at 1200 and 1300 cm^{-1} are also replicated by the computed furanose spectra. In addition, the intense oscillator at 1030 cm^{-1} is seen in the β-anomer of the furanose. Overall, the spectral match is good. The additional match of relative TIMS mobilities also confirmed the conversion of pyranose GlcNAc6S to furanose GlcNAc6S in the gas phase. For this transition to occur, a ring-opening is necessary. This claim is also supported by the conversion seen in GalNAc6S, the C4 epimer of GlcNAc6S. A ring-opening during activation also implies the existence of mutarotation of GlcNAc6S and GalNAc6S in the gas phase, since a ring closure can occur through C5 of the open-chain glycan again, making the determination of the reducing-end configuration, after CID fragmentation, impossible.

6.3 Conclusion

During CID fragmentation of HS2SNAc-ProA, the migration of the sulfate group from the terminal to the reducing-end sugar was observed. Utilizing IMS, the migration site was determined by comparison to synthetic standards. Additionally, the influence of different reducing-end labels on the migration products was shown. Energy-resolved IMS measurements showed the multistage nature of the migration process, revealing a step-wise migration to the *6O*- and then *3O*-position. By forming and dissociating non-covalent complexes between a highly sulfated pentasaccharide and a dipeptide, intermolecular transfer of a sulfate from the saccharide to the peptide in the gas phase was observed.

For GlcNAc6S and GalNAc6S an unexpected, ion activation-dependent conversion between the two species was observed. Varying TIMS accumulation time led to the conversion of an extended into a compact species, due to RF heating. IR-tagging spectroscopy on the size and mass selected species was utilized to give insight into their respective structure. The IR spectrum of the native GlcNAc6S species showed a good match to the computed spectra of the pyranose GlcNAc6S α and β anomers, but no match for the activated GlcNAc6S was seen with the computed spectra. Sulfate migration as a cause for the conversion could be excluded,

through a comparison of mobilities to a synthetic standard and comparing their computed IR spectra to the measured one. To fix the configuration at the anomeric centre, GlcNAc6S was glycosylated under acid catalysis to obtain a mixture of α and β anomers of the pyranose- and furanose-form of GlcNAc6S-Me. TIMS revealed a near identical shift in ion mobilities for furanose and pyranose GlcNAc6S-Me to the measured native and activated GlcNAc6S, suggesting a conversion from pyranose the furanose GlcNAc6S in the gas-phase. To confirm this assignment, spectra were computed for the furanose GlcNAc6S and they indeed show a good match for the activated GlcNAc6S spectrum.

These experiments show two new CID-induced sulfated glycan rearrangements, which influence their respective analysis in the gas phase substantially. The migration of sulfates during activation can lead to wrong structural assignment. Additionally, sulfated glycans unexpectedly undergo mutarotation during activation in the gas phase, making the assignment of their respective configuration difficult.

6.4 Experimental Section

Chemicals

All chemicals and solvents were purchased from Sigma-Aldrich (St. Louis, USA) and used without further purification. The HS2SNAc standard was purchased from Iduron (Cheshire, UK). HPLC-grade solvents were used throughout. GlcNAc3S was synthesized by acetylation of GlcN3S. Reducing-end labelled glycans were synthesised according to established protocols (as per Ludger ProA labelling kit).[227, 228]

Glycosylation reaction

Dowex 50 W was washed with HCl (1.0 M aq.) three times. A suspension of the obtained resin (<1 mg) and GlcNAc6S (1 mg, 3 μmol) in MeOH (1 mL) was heated to 60°C overnight. After cooling to room temperature, the resin was filtered off and the filtrate concentrated to give GlcNAc6S-Me.

Computational Method

Initial geometries of GlcNAc6S candidates were constructed by chemical intuition using GaussView 6.[250] Conformational searches were performed using CREST[251] with the semiempirical method GFN2-xTB[252] using default settings. The selected structures are reoptimized and their harmonic frequencies are computed at the PBE1PBE/6-311+G(d,p) EmpiricalDispersion=GD3BJ[253, 254] level of theory using Gaussian 16.[250] The calculated harmonic vibrational frequencies have been scaled with a standard scaling factor of 0.965. CCS values for GlcNAc6S; 4S; 3S-ProA were extracted using the projection approximation of Mobcal 2.0.

MS and IM-MS measurements

For MS analysis, samples were dissolved prior to use with water:methanol:ammonium acetate (1:1:50 v:v:mM) to yield 5-10 μM analyte solutions. Sulfate migration-related measurements are performed on the Waters Synapt G2-S using nESI. A capillary voltage of 0.8 kV was used, with a source temperature of 150°C. Standard TW-IMS settings were used with a trap wave height of 40 V, velocity of 311 m/s, IMS wave height of 40 V, velocity of 450 m/s and transfer wave height of 4 V, velocity of 175 m/s. The dipeptide experiment was performed on a Bruker Amazon Speed ETD ion trap instrument using the standard CID method. Mobilities for GlcNAc6S, GalNAc6S and GlcNAc3S were measured on the Bruker timsTOF Pro utilizing the home-build nESI source. A dry gas flow of 3 L/min with a temperature of 150°C was used. Delta values (1-6) were used as follows 10; 30; -100; -100, 0; -50 V. A ramp time of 200 ms was used. For the GlcNAc3S/GlcNAc6S mixture, a ramp time of 1000 ms was utilized. A range from 0.60 to 1.00 $V*s*cm^{-2}$ was scanned. If not otherwise specified, an accumulation time of 10 ms was used.

IR-tagging spectroscopy measurements

For the IR-tagging spectroscopy, the in-house constructed drift-tube ion mobility-mass spectrometer was used. Ions are produced by nESI from a Pd/Pt-coated borosilicate capillary and are transferred and stored in the entrance funnel where activation can occur. Afterwards, the ions are released by 150 μs long pulses into a drift tube filled with helium buffer gas (~5

mbar) and travel through the drift tube under the influence of a weak electric field (10-20 V/cm). The ion mobility and *m*/*z* selected ion cloud is then irradiated by a ~1.2 mJ pulse of IR photons. Wavenumber scanning was performed by steps of 2 cm^{-1} and 50 averages were used per recorded point. The utilized laser system is a LaserVision (Bellevue, WA, USA) OPO - OPA briefly described in Chapter 3.

7| Summary and Future Perspective

The gas-phase structural analysis of sulfated glycans remains a challenge to this day. While countless proof-of-concept studies exist, no standard technique for their analysis has crystallized yet. It is plagued by unwanted fragmentation, excessive adduct formation, and a broad distribution of charge states. Therefore, an extensive instrumental tuning is vital for a clean signal, but it often comes at the cost of a lower signal intensity. Thermal fragmentation techniques such as CID as well as higher energy collision-induced dissociation struggle with the retention of sulfate groups and are unable to differentiate between uronic acid isomers present in GAG oligosaccharides. These properties make the sequencing of already a GAG tetrasaccharide extremely challenging.

IM-MS proved its usefulness in GAG analysis before, showing high potential for sequencing purposes. Furthermore, its ability to reduce sample complexity is also a strong point of this method. The replacement of LC-MS workflows by time-efficient IM-MS methods will likely continue in the coming years. State-of-the-art proteomics workflows already rely on very short LC gradients coupled with subsequent IM-MS analysis,[255, 256] with many manufacturers developing "mini-LC" systems specialized in these types of gradients.[257] However, the lack of a confident quantification method remains the highest barrier to a complete translation of LC methods into IMS. The solution for this issue often comes with unwanted additional sample preparation steps, such as the stable isotope method,[258, 259] but allows for unprecedented quantification accuracy.

The additional coupling of IMS to cold gas-phase IR spectroscopy provides unprecedented analytical capabilities for gas-phase structural analysis. Expensive computational analysis of IR spectra will likely not find wider use in industry. While still applicable for small molecules,

which are common in e.g. metabolomics, the sheer number of structures will make this task nearly impossible. The alternate fingerprinting approach is easy to apply and methodologically follows conventions already established in MS workflows. Similar to EI-MS or CID-MS/MS libraries,[260, 261] cold gas-phase IR libraries can be created. These spectroscopic libraries are already common for condensed-phase techniques and could be easily replicated.[262] The primary limitations of cold gas-phase IR spectroscopy are (1) its accessibility and (2) the time scale of the experiment. To this date, no cold gas-phase IR instrument has been commercialized. While cold tagging can be performed in common 3D-paul ion traps, advancements in laser technology have only recently allowed for comparatively easy and fast IR analysis.[263] The first commercial cold gas-phase IR instrument is already in development, and its success will likely have a high impact on the field of gas-phase structural analysis.

Integrating IMS and cold gas-phase IR spectroscopy in more analytical workflows would greatly advance glycomics and related disciplines. In this thesis, IMS-IR coupled mass spectrometry was able to give insight into the complex binding motif of gadolinium to a GAG, even without computational support. IM-MS showed its capability to replace LC-MS workflows; it was able to separate a mixture of twelve partially isomeric structures, which previously were only quantifiable by long LC-MS methods. The combination of the developed IM-MS method with LC could open the doors for high-throughput tetrasaccharide analysis, which would be the only advancement in clinical GAG analysis since the first development of the disaccharide analysis.

Lastly, IMS showed its ability to observe rearrangement reactions in the gas phase, which otherwise would be overlooked. With the support of cold gas-phase IR spectroscopy, these rearrangement processes were elucidated. While especially the furanose formation during activation may hinder gas-phase sequencing approaches, the observed sulfate migration could have use in the field of structural biology. During activation, the GAG-peptide complex dissociated into a sulfated peptide. This intermolecular migration of the sulfate could be used to elucidate GAG binding sites in proteins. To date, most GAG binding sites in proteins are identified by crystallographic approaches, where sample preparation is laborious.[264] By the thermal activation of a protein-GAG complex, with a subsequent harsh top-down protein

sequencing approach such as UVPD,[265, 266] sulfated peptides could indicate the binding site of the GAG. In principle, these experiments could be performed in a commercial Thermo Fisher UVPD Orbitrap.

I Appendix A: Ion Mobility Mass Spectrometry-based Disaccharide Analysis

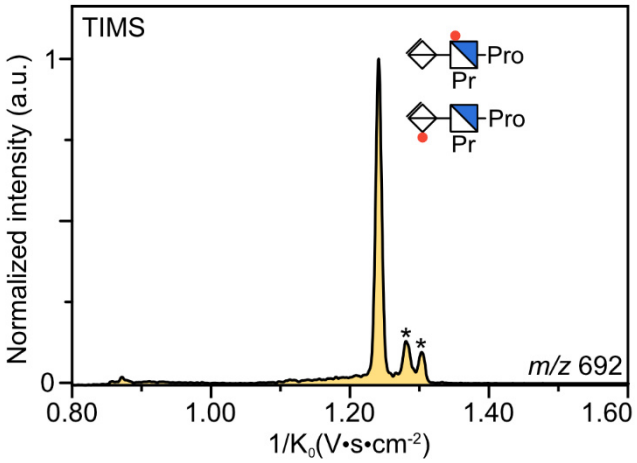

Figure A1: TIMS mobilogram of procaine (Pro) labelled HS-6SNPr and HS-2SNPr, no separation between the species visible.

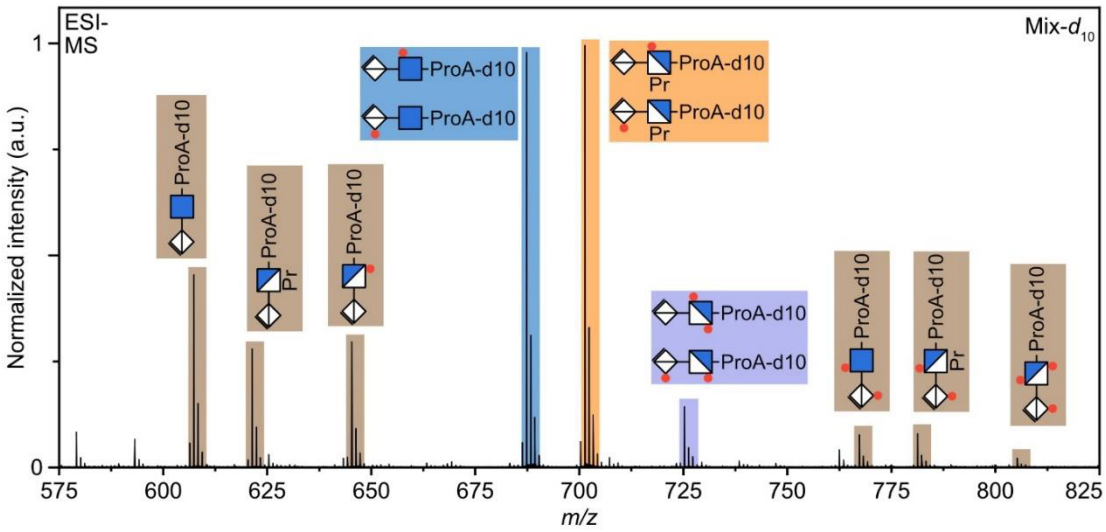

Figure A2: Mass spectrum of the used equimolar stable isotope labelled standard mixture.

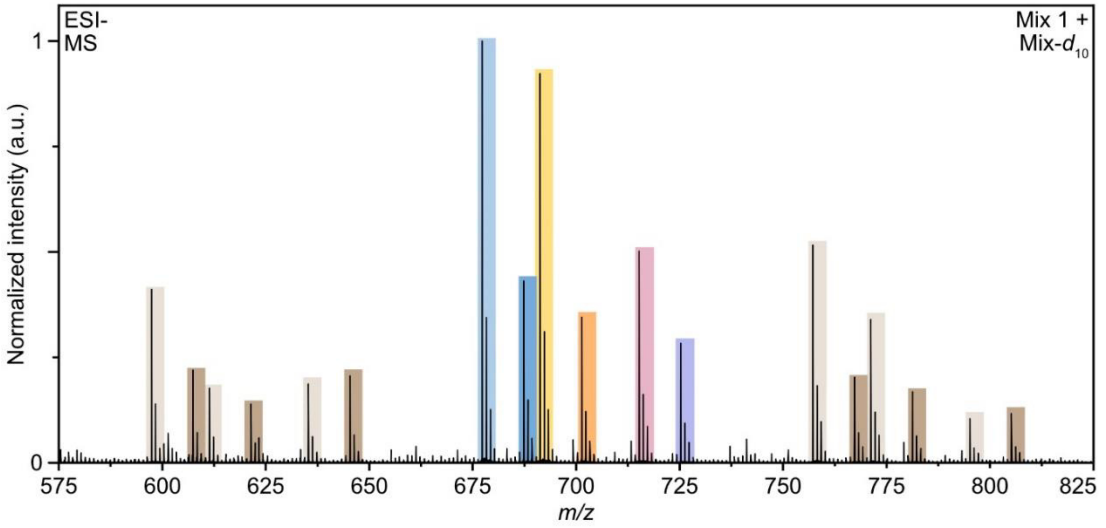

Figure A3: Mass spectrum of mixture 1 with the added stable isotope labelled standard mixture.

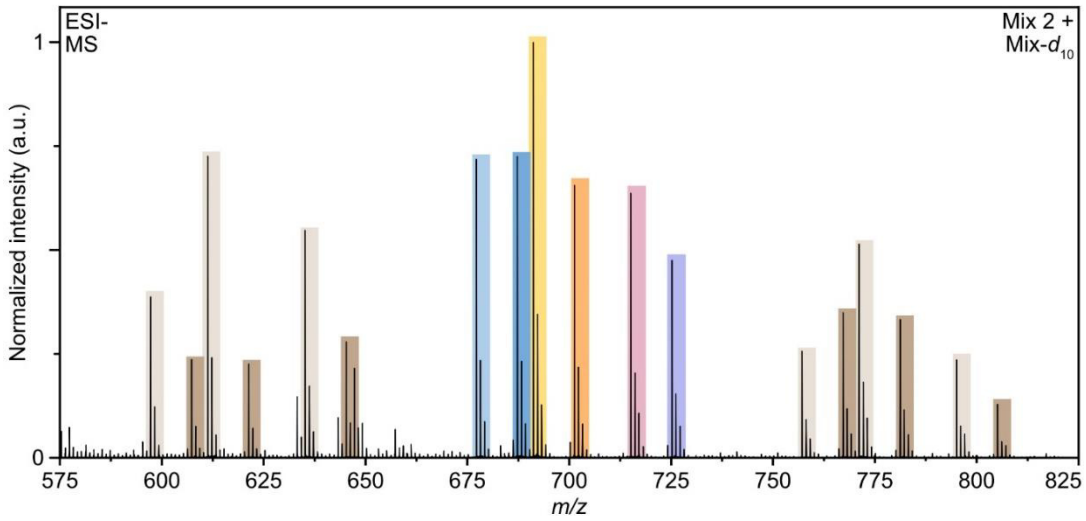

Figure A4: Mass spectrum of mixture 2 with the added stable isotope labelled standard mixture.

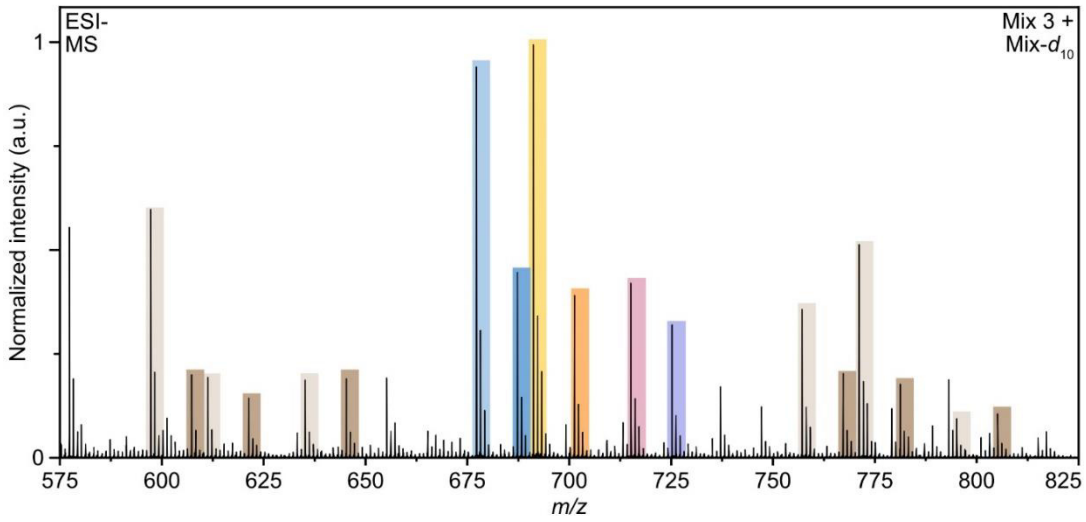

Figure A5: Mass spectrum of mixture 3 with the added stable isotope labelled standard mixture.

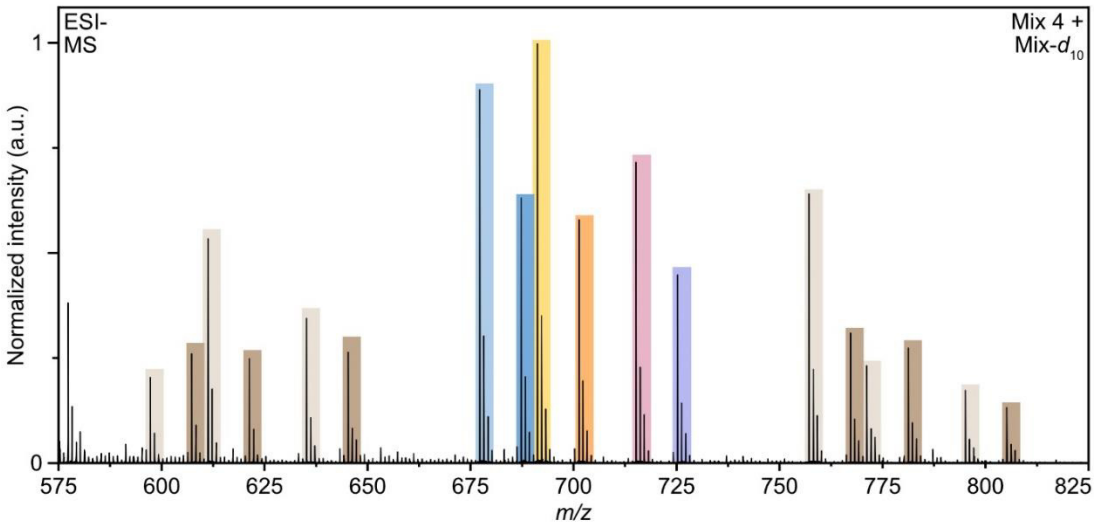

Figure A6: Mass spectrum of mixture 4 with the added stable isotope labelled standard mixture.

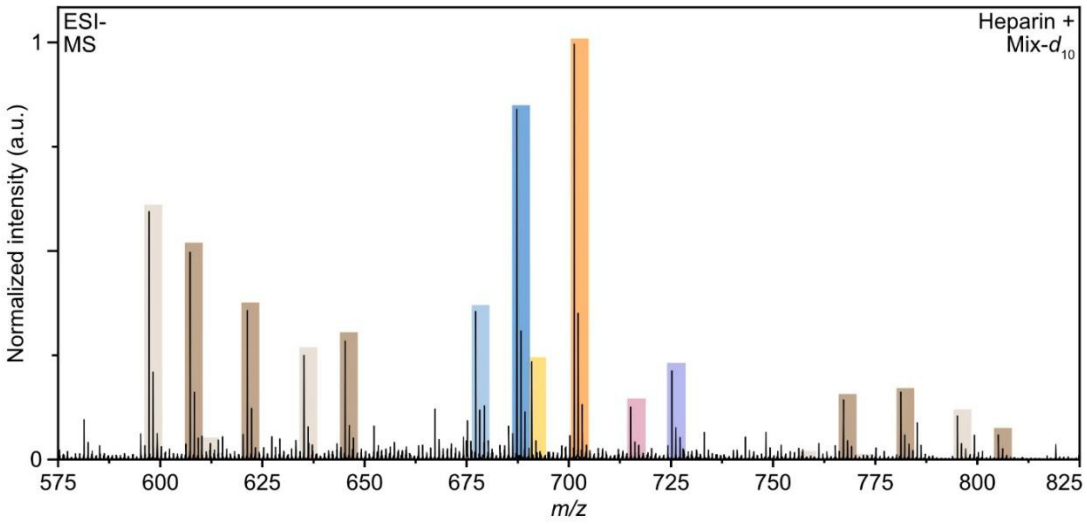

Figure A7: Mass spectrum of the digested heparin with the added stable isotope labelled standard mixture.

Table A1: reciprocal mobilities of the ProA and ProA-d10 labelled disaccharides in V*s/cm².

	ProA	ProA-d10
HS-NAc	1.149	1.153
HS-NPr	1.170	1.176
HS-NS	1.155	1.159
HS-6SNAc	1.162	1.164
HS-2SNAc	1.196	1.199
HS-6SNPr	1.189	1.190
HS-2SNPr	1.215	1.218
HS-6SNS	1.119	1.120
HS-2SNS	1.132	1.133
HS-2S6SNAc	1.180	1.181
HS-2S6SNPr	1.198	1.199
HS-2S6SNS	1.192	1.193

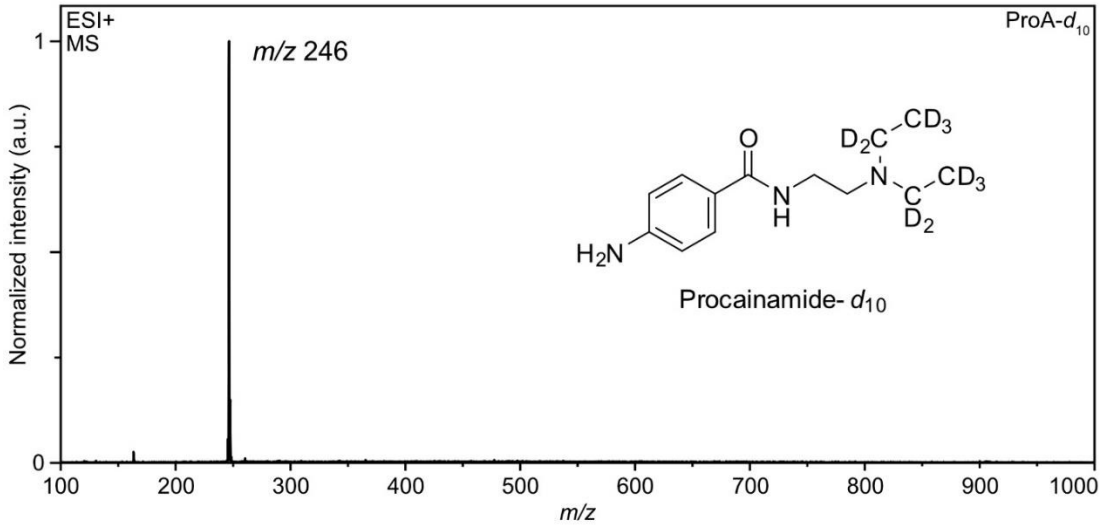

Figure A8: ESI+ Mass spectrum of Procainamide-d_{10} used for labelling after clean-up.

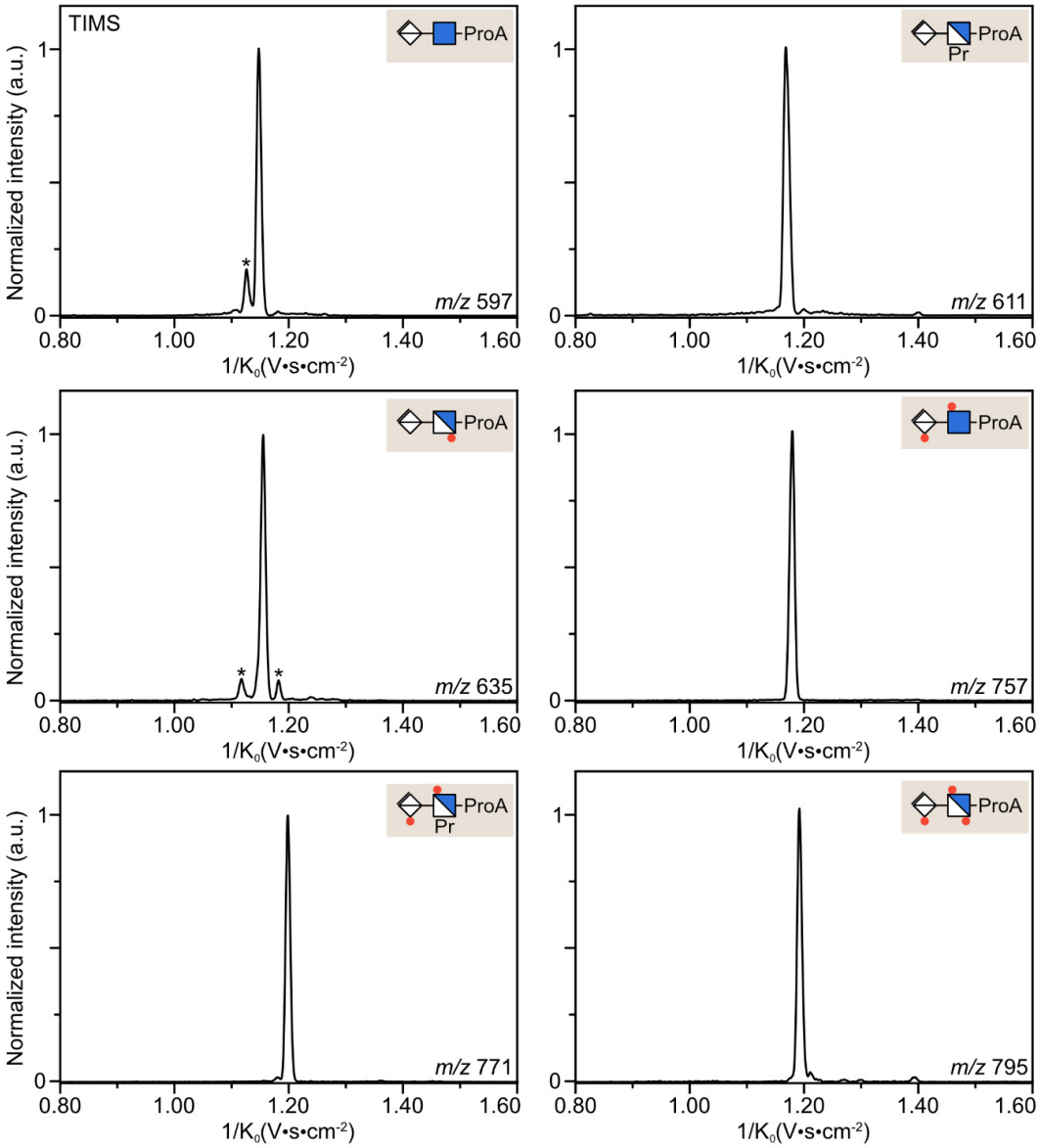

Figure A9: TIMS mobilograms of the six non-isomeric disaccharides after propionylation and procainamide labelling.

Appendix B: Intramolecular Rearrangement of Sulfated Glycans

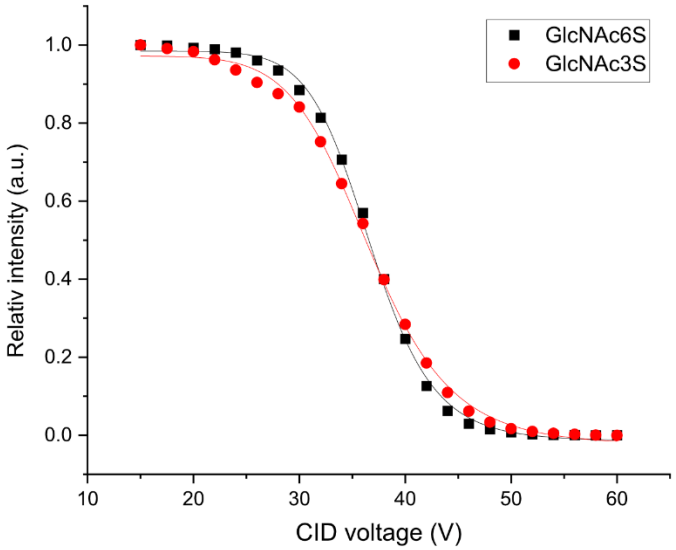

Figure B1: Survival yield curves of GlcNAc6S (black) and GlcNAc3S (red) fitted with logistic functions.

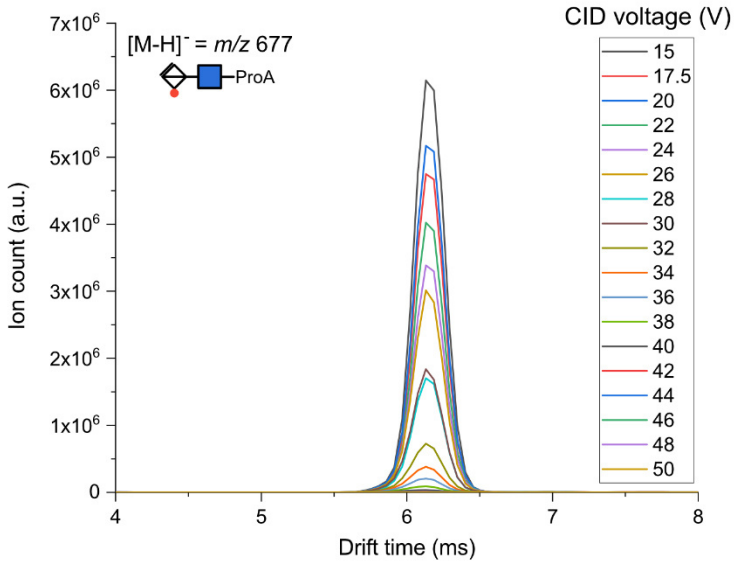

Figure B2: TW-IMS ATD of HS2SNAc-ProA after activation at different CID voltages. No change in drift time is observed.

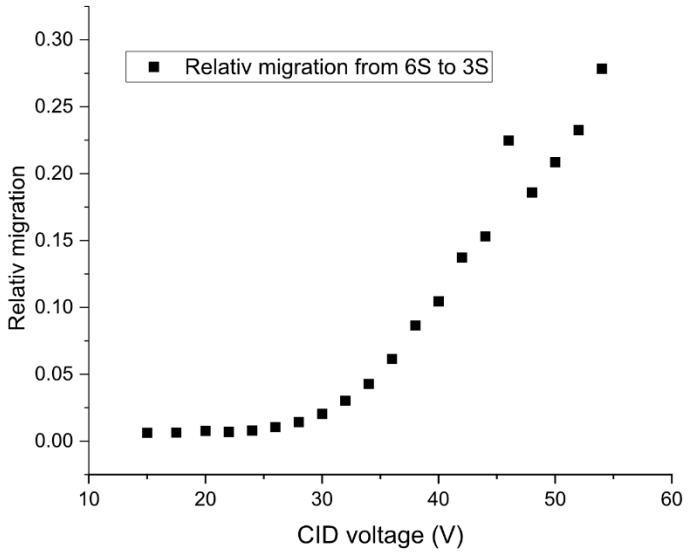

Figure B3: Relative migration from *6O-* to *3O-* during activation of the GlcNAc6S-ProA standard at different CID voltages.

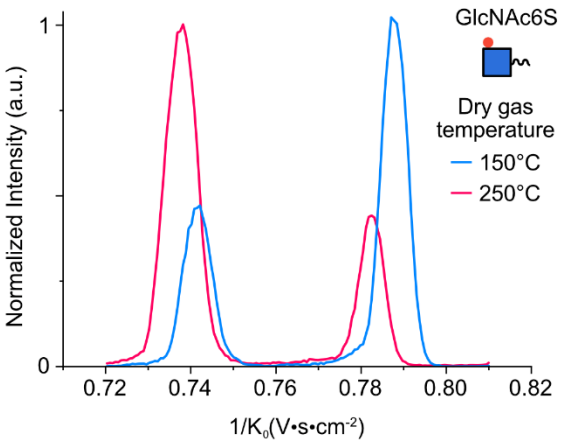

Figure B4: Mobilograms of GlcNAc6S at two different dry gas temperatures, 150 °C (blue) and 250 °C (red).

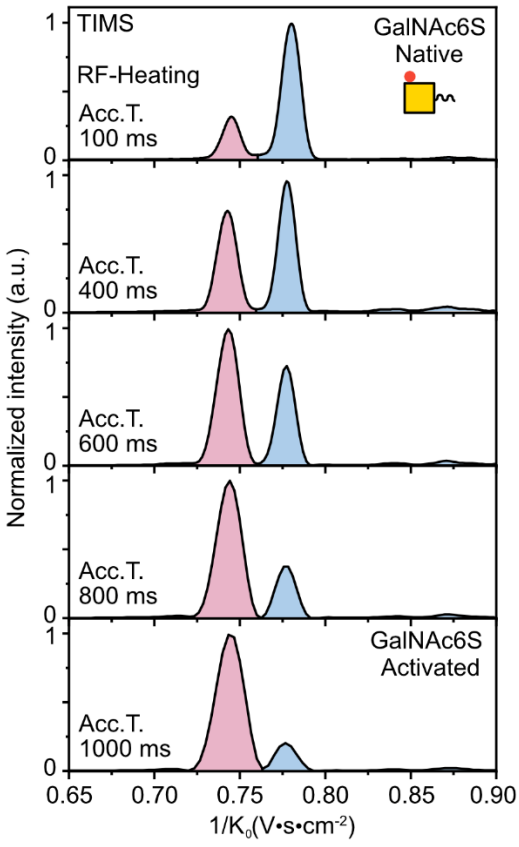

Figure B5: RF activation of GalNAc6S shows the same behaviour as GlcNAc6S, likely resulting from the same rearrangement process.

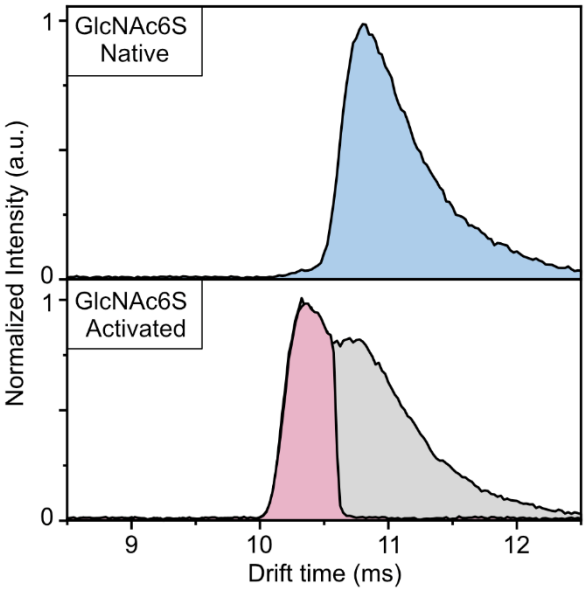

Figure B6: ATDs recorded on the IR-Tagging DT-IMS instrument. Top shows the native GlcNAc6S ATD from which the native IR spectrum was recorded. Bottom shows the activated ATD. The red inlay indicates the size-selected fraction from which the activated IR spectrum was recorded.

I List of Publications

(1) M. Lettow, M. Grabarics, E. Mucha, D. A. Thomas, L. Polewski, J. Freyse, J. Rademann, G. Meijer, G. von Helden, K. Pagel, IR action spectroscopy of glycosaminoglycan oligosaccharides, *Anal. Bioanal. Chem.* **2020**, 412, 533–537.

(2) L. Polewski, A. Springer, K. Pagel, C. Schalley, Gas-Phase Structural Analysis of Supramolecular Assemblies, *Acc. Chem. Res.* **2021**, 54, 10, 2445–2456.

(3) C. Kirschbaum, K. Greis, L. Polewski, S. Gewinner, W. Schöllkopf, G. Meijer, G. von Helden, K. Pagel, Unveiling Glycerolipid Fragmentation by Cryogenic Infrared Spectroscopy, *J. Am. Chem. Soc.* **2021**, 143, 36, 14827–14834.

(4) S. Polla, B. Maurina, A. Springer, L. Polewski, Preliminary results of the analysis of the organic residues in amphorae from the alpine castrum at Loppio- S. Andrea (Trentino, Italy), FOLD&R **2021.**

(5) C. Manz, M. Mancera-Arteu, A. Zappe, E. Hanozin, L. Polewski, E. Giménez, V. Nebot, K. Pagel, Determination of Sialic Acid Isomers from Released N-Glycans Using Ion Mobility Spectrometry, *Anal. Chem.* **2022**, 94, 39, 13323–13331.

(6) G. Szekeres, E. Hanozin, R. Diehn, J. Horlebein, L. Polewski, A. Zappe, D. Lauster, K. Pagel, Heparin increases the antibiotic efficacy of colistin, *Front. Anal. Sci.* **2023**, 3, 1154391.

(7) M. Götze, L. Polewski, L. Bechtella, K. Pagel, A 3D-Printed Offline Nano-ESI Source for Bruker MS Instruments, *J. Am. Soc. Mass Spectrom.* **2023**, 34, 10, 2403–2406.

(8) L. Bechtella, J. Chunsheng, K. Fentker, G. Ertürk, M. Safferthal, L. Polewski, M. Götze, S. Graeber, G. Vos, W. Struwe, M. Mall, P. Mertins, N. Karlsson, K. Pagel, Ion mobility-tandem mass spectrometry of mucin-type O-glycans, *Nat. Commun.* **2024**, 15, 2611.

(9) L. Polewski, E. Moon, A. Zappe, M. Götze, G. Szekeres, C. Roth, K. Pagel, Ion Mobility Mass Spectrometry-based Disaccharide Analysis of Glycosaminoglycans, *Chem. Eur. J.* **2024**, e202400783.

(10) L. Polewski, D. Dymnikova, W. Malicka, M. Lettow, G. Helden, C. Teutloff, M. Ballauff, M. Taupitz, R. Bittl, K. Pagel, Glycan-Induced Release of Gadolinium from MRI Contrast Agents, submitted.

(11) L. Polewski, M. Yaman, M. Marianski, K. Pagel, Mechanistic Study of Sulfate Migration in Glycans, in preparation.

(12) L. Polewski, J. Horlebein, G. Szekeres, C. Chang, G. Vos, M. Safferthal, G. Meijer, G. von Helden, K. Pagel, Gas-Phase Glycan Mutarotation, in preparation.

I Bibliography

1. van Rooijen, J. J. M.; Kamerling, J. P.; Vliegenthart, J. F. G., Sulfated di-, tri- and tetraantennary N-glycans in human Tamm-Horsfall glycoprotein. *European Journal of Biochemistry* **1998,** *256* (2), 471-487.
2. Yan, S.; Brecker, L.; Jin, C.; Titz, A.; Dragosits, M.; Karlsson, N. G.; Jantsch, V.; Wilson, I. B. H.; Paschinger, K., Bisecting Galactose as a Feature of N-Glycans of Wild-type and Mutant Caenorhabditis elegans*. *Molecular & Cellular Proteomics* **2015,** *14* (8), 2111-2125.
3. Wilm, M.; Shevchenko, A.; Houthaeve, T.; Breit, S.; Schweigerer, L.; Fotsis, T.; Mann, M., Femtomole sequencing of proteins from polyacrylamide gels by nano-electrospray mass spectrometry. *Nature* **1996,** *379* (6564), 466-469.
4. Bennett, H. M.; Stephenson, W.; Rose, C. M.; Darmanis, S., Single-cell proteomics enabled by next-generation sequencing or mass spectrometry. *Nature Methods* **2023,** *20* (3), 363-374.
5. Hofmann, J.; Pagel, K., Glycan Analysis by Ion Mobility–Mass Spectrometry. *Angewandte Chemie International Edition* **2017,** *56* (29), 8342-8349.
6. Manz, C.; Grabarics, M.; Hoberg, F.; Pugini, M.; Stuckmann, A.; Struwe, W. B.; Pagel, K., Separation of isomeric glycans by ion mobility spectrometry – the impact of fluorescent labelling. *Analyst* **2019,** *144* (17), 5292-5298.
7. Manz, C.; Pagel, K., Glycan analysis by ion mobility-mass spectrometry and gas-phase spectroscopy. *Current Opinion in Chemical Biology* **2018,** *42*, 16-24.
8. Mucha, E.; González Flórez, A. I.; Marianski, M.; Thomas, D. A.; Hoffmann, W.; Struwe, W. B.; Hahm, H. S.; Gewinner, S.; Schöllkopf, W.; Seeberger, P. H.; von Helden, G.; Pagel, K., Glycan Fingerprinting via Cold-Ion Infrared Spectroscopy. *Angewandte Chemie International Edition* **2017,** *56* (37), 11248-11251.
9. Mucha, E.; Stuckmann, A.; Marianski, M.; Struwe, W. B.; Meijer, G.; Pagel, K., In-depth structural analysis of glycans in the gas phase. *Chemical Science* **2019,** *10* (5), 1272-1284.
10. Lange, F. T.; Scheurer, M.; Brauch, H.-J., Artificial sweeteners—a recently recognized class of emerging environmental contaminants: a review. *Analytical and Bioanalytical Chemistry* **2012,** *403* (9), 2503-2518.
11. Reily, C.; Stewart, T. J.; Renfrow, M. B.; Novak, J., Glycosylation in health and disease. *Nature Reviews Nephrology* **2019,** *15* (6), 346-366.
12. Shivatare, S. S.; Shivatare, V. S.; Wong, C.-H., Glycoconjugates: Synthesis, Functional Studies, and Therapeutic Developments. *Chemical Reviews* **2022,** *122* (20), 15603-15671.
13. Feng, T.; Zhang, J.; Chen, Z.; Pan, W.; Chen, Z.; Yan, Y.; Dai, J., Glycosylation of viral proteins: Implication in virus–host interaction and virulence. *Virulence* **2022,** *13* (1), 670-683.
14. Li, Y.; Liu, D.; Wang, Y.; Su, W.; Liu, G.; Dong, W., The Importance of Glycans of Viral and Host Proteins in Enveloped Virus Infection. *Frontiers in Immunology* **2021,** *12*.
15. Wu, C.-Y.; Lin, C.-W.; Tsai, T.-I.; Lee, C.-C. D.; Chuang, H.-Y.; Chen, J.-B.; Tsai, M.-H.; Chen, B.-R.; Lo, P.-W.; Liu, C.-P.; Shivatare, V. S.; Wong, C.-H., Influenza A surface glycosylation and vaccine design. *Proceedings of the National Academy of Sciences* **2017,** *114* (2), 280-285.

16. Kwong, P. D.; Wyatt, R.; Robinson, J.; Sweet, R. W.; Sodroski, J.; Hendrickson, W. A., Structure of an HIV gp120 envelope glycoprotein in complex with the CD4 receptor and a neutralizing human antibody. *Nature* **1998,** *393* (6686), 648-659.
17. Acosta-Gutiérrez, S.; Buckley, J.; Battaglia, G., The Role of Host Cell Glycans on Virus Infectivity: The SARS-CoV-2 Case. *Advanced Science* **2023,** *10* (1), 2201853.
18. Gorzkiewicz, M.; Cramer, J.; Xu, H. C.; Lang, P. A., The role of glycosylation patterns of viral glycoproteins and cell entry receptors in arenavirus infection. *Biomedicine & Pharmacotherapy* **2023,** *166*, 115196.
19. Baranowski, E.; Ruiz-Jarabo, C. M.; Domingo, E., Evolution of Cell Recognition by Viruses. *Science* **2001,** *292* (5519), 1102-1105.
20. Clausen, T. M.; Sandoval, D. R.; Spliid, C. B.; Pihl, J.; Perrett, H. R.; Painter, C. D.; Narayanan, A.; Majowicz, S. A.; Kwong, E. M.; McVicar, R. N.; Thacker, B. E.; Glass, C. A.; Yang, Z.; Torres, J. L.; Golden, G. J.; Bartels, P. L.; Porell, R. N.; Garretson, A. F.; Laubach, L.; Feldman, J.; Yin, X.; Pu, Y.; Hauser, B. M.; Caradonna, T. M.; Kellman, B. P.; Martino, C.; Gordts, P. L. S. M.; Chanda, S. K.; Schmidt, A. G.; Godula, K.; Leibel, S. L.; Jose, J.; Corbett, K. D.; Ward, A. B.; Carlin, A. F.; Esko, J. D., SARS-CoV-2 Infection Depends on Cellular Heparan Sulfate and ACE2. *Cell* **2020,** *183* (4), 1043-1057.e15.
21. O'Donnell, C. D.; Shukla, D., The importance of heparan sulfate in herpesvirus infection. *Virologica Sinica* **2008,** *23* (6), 383-393.
22. Shukla, D.; Spear, P. G., Herpesviruses and heparan sulfate: an intimate relationship in aid of viral entry. *The Journal of Clinical Investigation* **2001,** *108* (4), 503-510.
23. Rini, J. M.; Moremen, K. W.; Davis, B. G.; Esko, J. D., Glycosyltransferases and Glycan-Processing Enzymes. In *Essentials of Glycobiology*, Varki, A.; Cummings, R. D.; Esko, J. D.; Stanley, P.; Hart, G. W.; Aebi, M.; Mohnen, D.; Kinoshita, T.; Packer, N. H.; Prestegard, J. H.; Schnaar, R. L.; Seeberger, P. H., Eds. Cold Spring Harbor Laboratory Press; : 2022; pp 67-78.
24. Seeberger, P. H., Monosaccharide Diversity. In *Essentials of Glycobiology*, Varki, A.; Cummings, R. D.; Esko, J. D.; Stanley, P.; Hart, G. W.; Aebi, M.; Mohnen, D.; Kinoshita, T.; Packer, N. H.; Prestegard, J. H.; Schnaar, R. L.; Seeberger, P. H., Eds. Cold Spring Harbor Laboratory Press; : 2022; pp 21-32.
25. Pazur, J. H.; Miskiel, F. J.; Liu, B., The identification of furanose and pyranose ring forms of the reducing units of oligosaccharides. *Analytical Biochemistry* **1988,** *174* (1), 46-53.
26. Varki, A.; Cummings, R. D.; Aebi, M.; Packer, N. H.; Seeberger, P. H.; Esko, J. D.; Stanley, P.; Hart, G.; Darvill, A.; Kinoshita, T.; Prestegard, J. J.; Schnaar, R. L.; Freeze, H. H.; Marth, J. D.; Bertozzi, C. R.; Etzler, M. E.; Frank, M.; Vliegenthart, J. F. G.; Lütteke, T.; Perez, S.; Bolton, E.; Rudd, P.; Paulson, J.; Kanehisa, M.; Toukach, P.; Aoki-Kinoshita, K. F.; Dell, A.; Narimatsu, H.; York, W.; Taniguchi, N.; Kornfeld, S., Symbol Nomenclature for Graphical Representations of Glycans. *Glycobiology* **2015,** *25* (12), 1323-1324.
27. Neelamegham, S.; Aoki-Kinoshita, K.; Bolton, E.; Frank, M.; Lisacek, F.; Lütteke, T.; O'Boyle, N.; Packer, N. H.; Stanley, P.; Toukach, P.; Varki, A.; Woods, R. J.; The, S. D. G., Updates to the Symbol Nomenclature for Glycans guidelines. *Glycobiology* **2019,** *29* (9), 620-624.
28. Kirschbaum, C.; Greis, K.; Mucha, E.; Kain, L.; Deng, S.; Zappe, A.; Gewinner, S.; Schöllkopf, W.; von Helden, G.; Meijer, G.; Savage, P. B.; Marianski, M.; Teyton, L.; Pagel,

K., Unravelling the structural complexity of glycolipids with cryogenic infrared spectroscopy. *Nature Communications* **2021,** *12* (1), 1201.
29. Flynn, R. A.; Pedram, K.; Malaker, S. A.; Batista, P. J.; Smith, B. A. H.; Johnson, A. G.; George, B. M.; Majzoub, K.; Villalta, P. W.; Carette, J. E.; Bertozzi, C. R., Small RNAs are modified with N-glycans and displayed on the surface of living cells. *Cell* **2021,** *184* (12), 3109-3124.e22.
30. Ma, Y.; Guo, W.; Mou, Q.; Shao, X.; Lyu, M.; Garcia, V.; Kong, L.; Lewis, W.; Ward, C.; Yang, Z.; Pan, X.; Yi, S. S.; Lu, Y., Spatial imaging of glycoRNA in single cells with ARPLA. *Nature Biotechnology* **2024,** *42* (4), 608-616.
31. Xie, Y.; Hemberger, H.; Till, N. A.; Chai, P.; Watkins, C. P.; Lebedenko, C. G.; Caldwell, R. M.; George, B. M.; Bertozzi, C. R.; Garcia, B. A.; Flynn, R. A., The modified RNA base acp3U is an attachment site for N-glycans in glycoRNA. *bioRxiv* **2023**, 2023.11.06.565735.
32. Kim, S.; Choi, Y.-g.; Janssen, K.; Büll, C.; Joshi, B. S.; Pomorski, A.; Raz, V.; Tanenbaum, M. E.; Miesen, P.; Li, Z.; Joo, C., N-glycosylated molecules act as a co-precipitant in RNA purification. *bioRxiv* **2024**, 2024.03.12.584655.
33. Xu, S.; Xu, X.; Wu, R., Deciphering the Properties and Functions of Glycoproteins Using Quantitative Proteomics. *Journal of Proteome Research* **2023,** *22* (6), 1571-1588.
34. Kukuruzinska, M. A.; Lennon, K., Protein N-Glycosylation: Molecular Genetics and Functional Significance. *Critical Reviews in Oral Biology & Medicine* **1998,** *9* (4), 415-448.
35. Yan, A.; Lennarz, W. J., Unraveling the Mechanism of Protein N-Glycosylation*. *Journal of Biological Chemistry* **2005,** *280* (5), 3121-3124.
36. Esmail, S.; Manolson, M. F., Advances in understanding N-glycosylation structure, function, and regulation in health and disease. *European Journal of Cell Biology* **2021,** *100* (7), 151186.
37. Stanley, P.; Moremen, K. W.; Lewis, N. E.; Taniguchi, N.; Aebi, M., N-Glycans. In *Essentials of Glycobiology*, Varki, A.; Cummings, R. D.; Esko, J. D.; Stanley, P.; Hart, G. W.; Aebi, M.; Mohnen, D.; Kinoshita, T.; Packer, N. H.; Prestegard, J. H.; Schnaar, R. L.; Seeberger, P. H., Eds. Cold Spring Harbor Laboratory Press; : 2022; pp 103-16.
38. Tran, D. T.; Ten Hagen, K. G., Mucin-type O-Glycosylation during Development*. *Journal of Biological Chemistry* **2013,** *288* (10), 6921-6929.
39. Robbe, C.; Capon, C.; Coddeville, B.; Michalski, J.-C., Structural diversity and specific distribution of O-glycans in normal human mucins along the intestinal tract. *Biochemical Journal* **2004,** *384* (2), 307-316.
40. Brockhausen, I.; Stanley, P., O-GalNAc Glycans. In *Essentials of Glycobiology*, Varki, A.; Cummings, R. D.; Esko, J. D.; Stanley, P.; Hart, G. W.; Aebi, M.; Darvill, A. G.; Kinoshita, T.; Packer, N. H.; Prestegard, J. H.; Schnaar, R. L.; Seeberger, P. H., Eds. Cold Spring Harbor Laboratory Press: 2015; pp 113-23.
41. Brockhausen, I., Pathways of O-glycan biosynthesis in cancer cells. *Biochimica et Biophysica Acta (BBA) - General Subjects* **1999,** *1473* (1), 67-95.
42. Gemmill, T. R.; Trimble, R. B., Overview of N- and O-linked oligosaccharide structures found in various yeast species. *Biochimica et Biophysica Acta (BBA) - General Subjects* **1999,** *1426* (2), 227-237.
43. Brockhausen, I., Sulphotransferases acting on mucin-type oligosaccharides. *Biochemical Society Transactions* **2003,** *31* (2), 318-325.

44. James, M. O., Enzyme Kinetics of PAPS-Sulfotransferase. In *Enzyme Kinetics in Drug Metabolism: Fundamentals and Applications*, Nagar, S.; Argikar, U. A.; Tweedie, D., Eds. Springer US: New York, NY, 2021; pp 285-300.
45. Xia, B.; Royall, J. A.; Damera, G.; Sachdev, G. P.; Cummings, R. D., Altered O-glycosylation and sulfation of airway mucins associated with cystic fibrosis. *Glycobiology* **2005,** *15* (8), 747-775.
46. Sun, L.; Konstantinidi, A.; Ye, Z.; Nason, R.; Zhang, Y.; Büll, C.; Kahl-Knutson, B.; Hansen, L.; Leffler, H.; Vakhrushev, S. Y.; Yang, Z.; Clausen, H.; Narimatsu, Y., Installation of O-glycan sulfation capacities in human HEK293 cells for display of sulfated mucins. *Journal of Biological Chemistry* **2022,** *298* (2), 101382.
47. Couchman, J. R.; Pataki, C. A., An Introduction to Proteoglycans and Their Localization. *Journal of Histochemistry & Cytochemistry* **2012,** *60* (12), 885-897.
48. Schaefer, L.; Schaefer, R. M., Proteoglycans: from structural compounds to signaling molecules. *Cell and Tissue Research* **2010,** *339* (1), 237-246.
49. Kiani, C.; Chen, L.; Wu, Y. J.; Yee, A. J.; Yang, B. B., Structure and function of aggrecan. *Cell Research* **2002,** *12* (1), 19-32.
50. Maloney, F. P.; Kuklewicz, J.; Corey, R. A.; Bi, Y.; Ho, R.; Mateusiak, L.; Pardon, E.; Steyaert, J.; Stansfeld, P. J.; Zimmer, J., Structure, substrate recognition and initiation of hyaluronan synthase. *Nature* **2022,** *604* (7904), 195-201.
51. Siiskonen, H.; Oikari, S.; Pasonen-Seppänen, S.; Rilla, K., Hyaluronan Synthase 1: A Mysterious Enzyme with Unexpected Functions. *Frontiers in Immunology* **2015,** *6*.
52. Weigel, P. H.; DeAngelis, P. L., Hyaluronan Synthases: A Decade-plus of Novel Glycosyltransferases*. *Journal of Biological Chemistry* **2007,** *282* (51), 36777-36781.
53. Plaas, A. H.; Neame, P. J.; Nivens, C. M.; Reiss, L., Identification of the keratan sulfate attachment sites on bovine fibromodulin. *Journal of Biological Chemistry* **1990,** *265* (33), 20634-20640.
54. Choi, H. U.; Meyer, K., The structure of keratan sulphates from various sources. *Biochemical Journal* **1975,** *151* (3), 543-553.
55. Krusius, T.; Finne, J.; Margolis, R. K.; Margolis, R. U., Identification of an O-glycosidic mannose-linked sialylated tetrasaccharide and keratan sulfate oligosaccharides in the chondroitin sulfate proteoglycan of brain. *Journal of Biological Chemistry* **1986,** *261* (18), 8237-8242.
56. Funderburgh, J. L., Keratan Sulfate Biosynthesis. *IUBMB Life* **2002,** *54* (4), 187-194.
57. Mikami, T.; Kitagawa, H., Biosynthesis and function of chondroitin sulfate. *Biochimica et Biophysica Acta (BBA) - General Subjects* **2013,** *1830* (10), 4719-4733.
58. Chen, Y.-H.; Narimatsu, Y.; Clausen, T. M.; Gomes, C.; Karlsson, R.; Steentoft, C.; Spliid, C. B.; Gustavsson, T.; Salanti, A.; Persson, A.; Malmström, A.; Willén, D.; Ellervik, U.; Bennett, E. P.; Mao, Y.; Clausen, H.; Yang, Z., The GAGOme: a cell-based library of displayed glycosaminoglycans. *Nature Methods* **2018,** *15* (11), 881-888.
59. Briggs, D. C.; Hohenester, E., Structural Basis for the Initiation of Glycosaminoglycan Biosynthesis by Human Xylosyltransferase 1. *Structure* **2018,** *26* (6), 801-809.e3.
60. Seidler, D. G.; Breuer, E.; Grande-Allen, K. J.; Hascall, V. C.; Kresse, H., Core Protein Dependence of Epimerization of Glucuronosyl Residues in Galactosaminoglycans *. *Journal of Biological Chemistry* **2002,** *277* (44), 42409-42416.

61. Sammon, D.; Krueger, A.; Busse-Wicher, M.; Morgan, R. M.; Haslam, S. M.; Schumann, B.; Briggs, D. C.; Hohenester, E., Molecular mechanism of decision-making in glycosaminoglycan biosynthesis. *Nature Communications* **2023,** *14* (1), 6425.
62. Kreuger, J.; Kjellén, L., Heparan Sulfate Biosynthesis: Regulation and Variability. *Journal of Histochemistry & Cytochemistry* **2012,** *60* (12), 898-907.
63. Leisico, F.; Omeiri, J.; Le Narvor, C.; Beaudouin, J.; Hons, M.; Fenel, D.; Schoehn, G.; Couté, Y.; Bonnaffé, D.; Sadir, R.; Lortat-Jacob, H.; Wild, R., Structure of the human heparan sulfate polymerase complex EXT1-EXT2. *Nature Communications* **2022,** *13* (1), 7110.
64. Li, H.; Chapla, D.; Amos, R. A.; Ramiah, A.; Moremen, K. W.; Li, H., Structural basis for heparan sulfate co-polymerase action by the EXT1–2 complex. *Nature Chemical Biology* **2023,** *19* (5), 565-574.
65. Aebersold, R.; Mann, M., Mass spectrometry-based proteomics. *Nature* **2003,** *422* (6928), 198-207.
66. Rampler, E.; Abiead, Y. E.; Schoeny, H.; Rusz, M.; Hildebrand, F.; Fitz, V.; Koellensperger, G., Recurrent Topics in Mass Spectrometry-Based Metabolomics and Lipidomics—Standardization, Coverage, and Throughput. *Analytical Chemistry* **2021,** *93* (1), 519-545.
67. Grabarics, M.; Lettow, M.; Kirschbaum, C.; Greis, K.; Manz, C.; Pagel, K., Mass Spectrometry-Based Techniques to Elucidate the Sugar Code. *Chemical Reviews* **2022,** *122* (8), 7840-7908.
68. Poulsen, S.-A., Direct Screening of a Dynamic Combinatorial Library Using Mass Spectrometry. *Journal of the American Society for Mass Spectrometry* **2006,** *17* (8), 1074-1080.
69. Termopoli, V.; Torrisi, E.; Famiglini, G.; Palma, P.; Zappia, G.; Cappiello, A.; Vandergrift, G. W.; Zvekic, M.; Krogh, E. T.; Gill, C. G., Mass Spectrometry Based Approach for Organic Synthesis Monitoring. *Analytical Chemistry* **2019,** *91* (18), 11916-11922.
70. Bossio, R. E.; Marshall, A. G., Baseline Resolution of Isobaric Phosphorylated and Sulfated Peptides and Nucleotides by Electrospray Ionization FTICR MS: Another Step toward Mass Spectrometry-Based Proteomics. *Analytical Chemistry* **2002,** *74* (7), 1674-1679.
71. Hoegg, E. D.; Godin, S.; Szpunar, J.; Lobinski, R.; Koppenaal, D. W.; Marcus, R. K., Ultra-High Resolution Elemental/Isotopic Mass Spectrometry ($m/\Delta m > 1{,}000{,}000$): Coupling of the Liquid Sampling-Atmospheric Pressure Glow Discharge with an Orbitrap Mass Spectrometer for Applications in Biological Chemistry and Environmental Analysis. *Journal of the American Society for Mass Spectrometry* **2019,** *30* (7), 1163-1168.
72. Zhou, X.; Wang, Z.; Li, S.; Rong, X.; Bu, J.; Liu, Q.; Ouyang, Z., Differentiating enantiomers by directional rotation of ions in a mass spectrometer. *Science* **2024,** *383* (6683), 612-618.
73. Zhou, X.; Wang, Z.; Fan, J.; Ouyang, Z., High-resolution separation of bioisomers using ion cloud profiling. *Nature Communications* **2023,** *14* (1), 1535.
74. Lanucara, F.; Holman, S. W.; Gray, C. J.; Eyers, C. E., The power of ion mobility-mass spectrometry for structural characterization and the study of conformational dynamics. *Nature Chemistry* **2014,** *6* (4), 281-294.
75. Thomson, J. J.; Rutherford, E., XL. On the passage of electricity through gases exposed to Röntgen rays. *The London, Edinburgh, and Dublin Philosophical Magazine and Journal of Science* **1896,** *42* (258), 392-407.

76. Zhou, Z.; Luo, M.; Chen, X.; Yin, Y.; Xiong, X.; Wang, R.; Zhu, Z.-J., Ion mobility collision cross-section atlas for known and unknown metabolite annotation in untargeted metabolomics. *Nature Communications* **2020,** *11* (1), 4334.
77. Celma, A.; Sancho, J. V.; Schymanski, E. L.; Fabregat-Safont, D.; Ibáñez, M.; Goshawk, J.; Barknowitz, G.; Hernández, F.; Bijlsma, L., Improving Target and Suspect Screening High-Resolution Mass Spectrometry Workflows in Environmental Analysis by Ion Mobility Separation. *Environmental Science & Technology* **2020,** *54* (23), 15120-15131.
78. Picache, J. A.; Rose, B. S.; Balinski, A.; Leaptrot, Katrina L.; Sherrod, S. D.; May, J. C.; McLean, J. A., Collision cross section compendium to annotate and predict multi-omic compound identities. *Chemical Science* **2019,** *10* (4), 983-993.
79. Haack, A.; Ieritano, C.; Hopkins, W. S., MobCal-MPI 2.0: an accurate and parallelized package for calculating field-dependent collision cross sections and ion mobilities. *Analyst* **2023,** *148* (14), 3257-3273.
80. Mason, E. A.; McDaniel, E. W., Kinetic Theory of Mobility and Diffusion: Sections 5.1 – 5.2. In *Transport Properties of Ions in Gases*, 1988; pp 137-193.
81. Stow, S. M.; Causon, T. J.; Zheng, X.; Kurulugama, R. T.; Mairinger, T.; May, J. C.; Rennie, E. E.; Baker, E. S.; Smith, R. D.; McLean, J. A.; Hann, S.; Fjeldsted, J. C., An Interlaboratory Evaluation of Drift Tube Ion Mobility–Mass Spectrometry Collision Cross Section Measurements. *Analytical Chemistry* **2017,** *89* (17), 9048-9055.
82. Young, M. N.; Bleiholder, C., Molecular Structures and Momentum Transfer Cross Sections: The Influence of the Analyte Charge Distribution. *Journal of the American Society for Mass Spectrometry* **2017,** *28* (4), 619-627.
83. Lalli, P. M.; Corilo, Y. E.; Fasciotti, M.; Riccio, M. F.; de Sa, G. F.; Daroda, R. J.; Souza, G. H. M. F.; McCullagh, M.; Bartberger, M. D.; Eberlin, M. N.; Campuzano, I. D. G., Baseline resolution of isomers by traveling wave ion mobility mass spectrometry: investigating the effects of polarizable drift gases and ionic charge distribution. *Journal of Mass Spectrometry* **2013,** *48* (9), 989-997.
84. Simón-Manso, Y., Ion-Neutral Collision Cross Section as a Function of the Static Dipole Polarizability and the Ionization Energy of the Ion. *The Journal of Physical Chemistry A* **2023,** *127* (15), 3274-3280.
85. Haynes, W. M., CRC Handbook of Chemistry and Physics, 95th Edition. 95th ed ed.; CRC Press: Hoboken, 2014. http://search.ebscohost.com/login.aspx?direct=true&scope=site&db=nlebk&db=nlabk&AN=1631986.
86. Gabelica, V.; Marklund, E., Fundamentals of ion mobility spectrometry. *Current Opinion in Chemical Biology* **2018,** *42*, 51-59.
87. Warnke, S.; Seo, J.; Boschmans, J.; Sobott, F.; Scrivens, J. H.; Bleiholder, C.; Bowers, M. T.; Gewinner, S.; Schöllkopf, W.; Pagel, K.; von Helden, G., Protomers of Benzocaine: Solvent and Permittivity Dependence. *Journal of the American Chemical Society* **2015,** *137* (12), 4236-4242.
88. Giles, K.; Pringle, S. D.; Worthington, K. R.; Little, D.; Wildgoose, J. L.; Bateman, R. H., Applications of a travelling wave-based radio-frequency-only stacked ring ion guide. *Rapid Communications in Mass Spectrometry* **2004,** *18* (20), 2401-2414.
89. Pringle, S. D.; Giles, K.; Wildgoose, J. L.; Williams, J. P.; Slade, S. E.; Thalassinos, K.; Bateman, R. H.; Bowers, M. T.; Scrivens, J. H., An investigation of the mobility

separation of some peptide and protein ions using a new hybrid quadrupole/travelling wave IMS/oa-ToF instrument. *International Journal of Mass Spectrometry* **2007,** *261* (1), 1-12.
90. Thalassinos, K.; Slade, S. E.; Jennings, K. R.; Scrivens, J. H.; Giles, K.; Wildgoose, J.; Hoyes, J.; Bateman, R. H.; Bowers, M. T., Ion mobility mass spectrometry of proteins in a modified commercial mass spectrometer. *International Journal of Mass Spectrometry* **2004,** *236* (1), 55-63.
91. Shaffer, S. A.; Prior, D. C.; Anderson, G. A.; Udseth, H. R.; Smith, R. D., An Ion Funnel Interface for Improved Ion Focusing and Sensitivity Using Electrospray Ionization Mass Spectrometry. *Analytical Chemistry* **1998,** *70* (19), 4111-4119.
92. Ibrahim, Y.; Belov, M. E.; Tolmachev, A. V.; Prior, D. C.; Smith, R. D., Ion Funnel Trap Interface for Orthogonal Time-of-Flight Mass Spectrometry. *Analytical Chemistry* **2007,** *79* (20), 7845-7852.
93. Wyttenbach, T.; Kemper, P. R.; Bowers, M. T., Design of a new electrospray ion mobility mass spectrometer. *International Journal of Mass Spectrometry* **2001,** *212* (1), 13-23.
94. Yousef, A.; Shrestha, S.; Viehland, L. A.; Lee, E. P. F.; Gray, B. R.; Ayles, V. L.; Wright, T. G.; Breckenridge, W. H., Interaction potentials and transport properties of coinage metal cations in rare gases. *The Journal of Chemical Physics* **2007,** *127* (15), 154309.
95. Morsa, D.; Gabelica, V.; De Pauw, E., Fragmentation and Isomerization Due to Field Heating in Traveling Wave Ion Mobility Spectrometry. *Journal of the American Society for Mass Spectrometry* **2014,** *25* (8), 1384-1393.
96. Giles, K.; Williams, J. P.; Campuzano, I., Enhancements in travelling wave ion mobility resolution. *Rapid Communications in Mass Spectrometry* **2011,** *25* (11), 1559-1566.
97. Smith, D. P.; Knapman, T. W.; Campuzano, I.; Malham, R. W.; Berryman, J. T.; Radford, S. E.; Ashcroft, A. E., Deciphering Drift Time Measurements from Travelling Wave Ion Mobility Spectrometry-Mass Spectrometry Studies. *European Journal of Mass Spectrometry* **2009,** *15* (2), 113-130.
98. Hofmann, J.; Struwe, W. B.; Scarff, C. A.; Scrivens, J. H.; Harvey, D. J.; Pagel, K., Estimating Collision Cross Sections of Negatively Charged N-Glycans using Traveling Wave Ion Mobility-Mass Spectrometry. *Analytical Chemistry* **2014,** *86* (21), 10789-10795.
99. Loboda, A., Novel ion mobility setup combined with collision cell and time-of-flight mass spectrometer. *Journal of the American Society for Mass Spectrometry* **2006,** *17* (5), 691-699.
100. Michelmann, K.; Silveira, J. A.; Ridgeway, M. E.; Park, M. A., Fundamentals of Trapped Ion Mobility Spectrometry. *Journal of the American Society for Mass Spectrometry* **2015,** *26* (1), 14-24.
101. Hernandez, D. R.; DeBord, J. D.; Ridgeway, M. E.; Kaplan, D. A.; Park, M. A.; Fernandez-Lima, F., Ion dynamics in a trapped ion mobility spectrometer. *Analyst* **2014,** *139* (8), 1913-1921.
102. Morsa, D.; Hanozin, E.; Eppe, G.; Quinton, L.; Gabelica, V.; Pauw, E. D., Effective Temperature and Structural Rearrangement in Trapped Ion Mobility Spectrometry. *Analytical Chemistry* **2020,** *92* (6), 4573-4582.
103. Bleiholder, C.; Liu, F. C.; Chai, M., Comment on Effective Temperature and Structural Rearrangement in Trapped Ion Mobility Spectrometry. *Analytical Chemistry* **2020,** *92* (24), 16329-16333.

104. Morsa, D.; Hanozin, E.; Gabelica, V.; De Pauw, E., Response to Comment on Effective Temperature and Structural Rearrangement in Trapped Ion Mobility Spectrometry. *Analytical Chemistry* **2020,** *92* (24), 16334-16337.
105. George, A. C.; Schmitz, I.; Colsch, B.; Afonso, C.; Fenaille, F.; Loutelier-Bourhis, C., Impact of Source Conditions on Collision Cross Section Determination by Trapped Ion Mobility Spectrometry. *Journal of the American Society for Mass Spectrometry* **2024,** *35* (4), 696-704.
106. Morsa, D.; Gabelica, V.; De Pauw, E., Effective Temperature of Ions in Traveling Wave Ion Mobility Spectrometry. *Analytical Chemistry* **2011,** *83* (14), 5775-5782.
107. Silveira, J. A.; Michelmann, K.; Ridgeway, M. E.; Park, M. A., Fundamentals of Trapped Ion Mobility Spectrometry Part II: Fluid Dynamics. *Journal of The American Society for Mass Spectrometry* **2016,** *27* (4), 585-595.
108. Olson, K. L.; Rinehart Jr, K. L.; Cook Jr, J. C., Phosphazenes: High molecular weight reference compounds for field desorption mass spectrometry. *Biomedical Mass Spectrometry* **1977,** *4* (5), 284-290.
109. Parks, J. H.; Szöke, A., Simulation of collisional relaxation of trapped ion clouds in the presence of space charge fields. *J. Chem. Phys.* **1995,** *103* (4), 1422-1439.
110. Oomens, J.; Sartakov, B. G.; Meijer, G.; von Helden, G., Gas-phase infrared multiple photon dissociation spectroscopy of mass-selected molecular ions. *Int. J. Mass Spectrom.* **2006,** *254* (1), 1-19.
111. Seo, J.; Warnke, S.; Pagel, K.; Bowers, M. T.; von Helden, G., Infrared spectrum and structure of the homochiral serine octamer–dichloride complex. *Nat. Chem.* **2017,** *9* (12), 1263-1268.
112. Seo, J.; Hoffmann, W.; Warnke, S.; Huang, X.; Gewinner, S.; Schöllkopf, W.; Bowers, M. T.; von Helden, G.; Pagel, K., An infrared spectroscopy approach to follow β-sheet formation in peptide amyloid assemblies. *Nat. Chem.* **2017,** *9* (1), 39-44.
113. Rizzo, T. R.; Boyarkin, O. V., Cryogenic Methods for the Spectroscopy of Large, Biomolecular Ions. In *Gas-Phase IR Spectroscopy and Structure of Biological Molecules*, Rijs, A. M.; Oomens, J., Eds. Springer International Publishing: Cham, 2015; pp 43-97.
114. Yatsyna, V.; Abikhodr, A. H.; Ben Faleh, A.; Warnke, S.; Rizzo, T. R., High-Throughput Multiplexed Infrared Spectroscopy of Ion Mobility-Separated Species Using Hadamard Transform. *Anal. Chem.* **2022,** *94* (6), 2912-2917.
115. Li, Y.-K.; Babin, M. C.; Debnath, S.; Iwasa, T.; Kumar, S.; Taketsugu, T.; Asmis, K. R.; Lyalin, A.; Neumark, D. M., Structural Characterization of Nickel-Doped Aluminum Oxide Cations by Cryogenic Ion Trap Vibrational Spectroscopy. *J. Phys. Chem. A* **2021,** *125* (43), 9527-9535.
116. Goebbert, D. J.; Wende, T.; Bergmann, R.; Meijer, G.; Asmis, K. R., Messenger-Tagging Electrosprayed Ions: Vibrational Spectroscopy of Suberate Dianions. *J. Phys. Chem. A* **2009,** *113* (20), 5874-5880.
117. Filsinger, F.; Ahn, D.-S.; Meijer, G.; von Helden, G., Photoexcitation of mass/charge selected hemin+, caught in helium nanodroplets. *Phys. Chem. Chem. Phys.* **2012,** *14* (38), 13370-13377.
118. Mucha, E.; González Flórez, A. I.; Marianski, M.; Thomas, D. A.; Hoffmann, W.; Struwe, W. B.; Hahm, H. S.; Gewinner, S.; Schöllkopf, W.; Seeberger, P. H.; von Helden,

G.; Pagel, K., Glycan Fingerprinting via Cold-Ion Infrared Spectroscopy. *Angew. Chem. Int. Ed.* **2017,** *56* (37), 11248-11251.
119. Thomas, D. A.; Mucha, E.; Lettow, M.; Meijer, G.; Rossi, M.; von Helden, G., Characterization of a trans–trans Carbonic Acid–Fluoride Complex by Infrared Action Spectroscopy in Helium Nanodroplets. *J. Am. Chem. Soc.* **2019,** *141* (14), 5815-5823.
120. Domon, B.; Costello, C. E., A systematic nomenclature for carbohydrate fragmentations in FAB-MS/MS spectra of glycoconjugates. *Glycoconjugate Journal* **1988,** *5* (4), 397-409.
121. Zaia, J., Glycosaminoglycan Glycomics Using Mass Spectrometry*. *Mol. Cell. Proteom.* **2013,** *12* (4), 885-892.
122. Shi, X.; Huang, Y.; Mao, Y.; Naimy, H.; Zaia, J., Tandem Mass Spectrometry of Heparan Sulfate Negative Ions: Sulfate Loss Patterns and Chemical Modification Methods for Improvement of Product Ion Profiles. *Journal of the American Society for Mass Spectrometry* **2012,** *23* (9), 1498-1511.
123. Attygalle, A. B.; García-Rubio, S.; Ta, J.; Meinwald, J., Collisionally-induced dissociation mass spectra of organic sulfate anions. *Journal of the Chemical Society, Perkin Transactions 2* **2001,** (4), 498-506.
124. Prabhu, G. R. D.; Williams, E. R.; Wilm, M.; Urban, P. L., Mass spectrometry using electrospray ionization. *Nature Reviews Methods Primers* **2023,** *3* (1), 23.
125. Murray, K. K., In defense of the quasimolecular ion. *Journal of Mass Spectrometry* **2021,** *56* (2), e4700.
126. Mitchell Wells, J.; McLuckey, S. A., Collision-Induced Dissociation (CID) of Peptides and Proteins. In *Methods in Enzymology*, Academic Press: 2005; Vol. 402, pp 148-185.
127. Johnson, A. R.; Carlson, E. E., Collision-Induced Dissociation Mass Spectrometry: A Powerful Tool for Natural Product Structure Elucidation. *Analytical Chemistry* **2015,** *87* (21), 10668-10678.
128. Sleno, L.; Volmer, D. A., Ion activation methods for tandem mass spectrometry. *Journal of Mass Spectrometry* **2004,** *39* (10), 1091-1112.
129. Kailemia, M. J.; Li, L.; Ly, M.; Linhardt, R. J.; Amster, I. J., Complete Mass Spectral Characterization of a Synthetic Ultralow-Molecular-Weight Heparin Using Collision-Induced Dissociation. *Analytical Chemistry* **2012,** *84* (13), 5475-5478.
130. Kang, P.; Mechref, Y.; Klouckova, I.; Novotny, M. V., Solid-phase permethylation of glycans for mass spectrometric analysis. *Rapid Communications in Mass Spectrometry* **2005,** *19* (23), 3421-3428.
131. Kang, P.; Mechref, Y.; Novotny, M. V., High-throughput solid-phase permethylation of glycans prior to mass spectrometry. *Rapid Communications in Mass Spectrometry* **2008,** *22* (5), 721-734.
132. Lei, M.; Mechref, Y.; Novotny, M. V., Structural analysis of sulfated glycans by sequential double-permethylation using methyl iodide and deuteromethyl iodide. *Journal of the American Society for Mass Spectrometry* **2009,** *20* (9), 1660-1671.
133. Huang, R.; Liu, J.; Sharp, J. S., An Approach for Separation and Complete Structural Sequencing of Heparin/Heparan Sulfate-like Oligosaccharides. *Analytical Chemistry* **2013,** *85* (12), 5787-5795.

134. Huang, R.; Pomin, V. H.; Sharp, J. S., LC-MSnAnalysis of Isomeric Chondroitin Sulfate Oligosaccharides Using a Chemical Derivatization Strategy. *Journal of The American Society for Mass Spectrometry* **2011,** *22* (9), 1577-1587.
135. Huang, R.; Zong, C.; Venot, A.; Chiu, Y.; Zhou, D.; Boons, G.-J.; Sharp, J. S., De Novo Sequencing of Complex Mixtures of Heparan Sulfate Oligosaccharides. *Analytical Chemistry* **2016,** *88* (10), 5299-5307.
136. Liu, H.; Liang, Q.; Sharp, J. S., Peracylation Coupled with Tandem Mass Spectrometry for Structural Sequencing of Sulfated Glycosaminoglycan Mixtures without Depolymerization. *Journal of the American Society for Mass Spectrometry* **2020,** *31* (10), 2061-2072.
137. Miller, R. L.; Guimond, S. E.; Schwörer, R.; Zubkova, O. V.; Tyler, P. C.; Xu, Y.; Liu, J.; Chopra, P.; Boons, G.-J.; Grabarics, M.; Manz, C.; Hofmann, J.; Karlsson, N. G.; Turnbull, J. E.; Struwe, W. B.; Pagel, K., Shotgun ion mobility mass spectrometry sequencing of heparan sulfate saccharides. *Nature Communications* **2020,** *11* (1), 1481.
138. Miller, R. L.; Wei, W.; Schwörer, R.; Zubkova, O. V.; Tyler, P. C.; Turnbull, J. E.; Leary, J. A., Composition, Sequencing and Ion Mobility Mass Spectrometry of Heparan Sulfate-like Octasaccharide Isomers Differing in Glucuronic and Iduronic Acid Content. *European Journal of Mass Spectrometry* **2015,** *21* (3), 245-254.
139. Agyekum, I.; Zong, C.; Boons, G.-J.; Amster, I. J., Single Stage Tandem Mass Spectrometry Assignment of the C-5 Uronic Acid Stereochemistry in Heparan Sulfate Tetrasaccharides using Electron Detachment Dissociation. *Journal of The American Society for Mass Spectrometry* **2017,** *28* (9), 1741-1750.
140. Leach, F. E.; Xiao, Z.; Laremore, T. N.; Linhardt, R. J.; Amster, I. J., Electron detachment dissociation and infrared multiphoton dissociation of heparin tetrasaccharides. *International Journal of Mass Spectrometry* **2011,** *308* (2), 253-259.
141. Oh, H. B.; Leach, F. E., III; Arungundram, S.; Al-Mafraji, K.; Venot, A.; Boons, G.-J.; Amster, I. J., Multivariate Analysis of Electron Detachment Dissociation and Infrared Multiphoton Dissociation Mass Spectra of Heparan Sulfate Tetrasaccharides Differing Only in Hexuronic acid Stereochemistry. *Journal of the American Society for Mass Spectrometry* **2011,** *22* (3), 582-590.
142. Wolff, J. J.; Chi, L.; Linhardt, R. J.; Amster, I. J., Distinguishing Glucuronic from Iduronic Acid in Glycosaminoglycan Tetrasaccharides by Using Electron Detachment Dissociation. *Analytical Chemistry* **2007,** *79* (5), 2015-2022.
143. Wolff, J. J.; Laremore, T. N.; Busch, A. M.; Linhardt, R. J.; Amster, I. J., Influence of charge state and sodium cationization on the electron detachment dissociation and infrared multiphoton dissociation of glycosaminoglycan oligosaccharides. *Journal of the American Society for Mass Spectrometry* **2008,** *19* (6), 790-798.
144. Wolff, J. J.; Laremore, T. N.; Leach, F. E.; Linhardt, R. J.; Amster, I. J., Electron Capture Dissociation, Electron Detachment Dissociation and Infrared Multiphoton Dissociation of Sucrose Octasulfate. *European Journal of Mass Spectrometry* **2009,** *15* (2), 275-281.
145. Huang, Y.; Yu, X.; Mao, Y.; Costello, C. E.; Zaia, J.; Lin, C., De novo sequencing of heparan sulfate oligosaccharides by electron-activated dissociation. *Anal Chem* **2013,** *85* (24), 11979-86.

146. Leach, F. E., 3rd; Ly, M.; Laremore, T. N.; Wolff, J. J.; Perlow, J.; Linhardt, R. J.; Amster, I. J., Hexuronic acid stereochemistry determination in chondroitin sulfate glycosaminoglycan oligosaccharides by electron detachment dissociation. *J Am Soc Mass Spectrom* **2012,** *23* (9), 1488-97.
147. Agyekum, I.; Patel, A. B.; Zong, C.; Boons, G. J.; Amster, J., Assignment Of Hexuronic Acid Stereochemistry In Synthetic Heparan Sulfate Tetrasaccharides With 2-O-Sulfo Uronic Acids Using Electron Detachment Dissociation. *Int J Mass Spectrom* **2015,** *390*, 163-169.
148. Kailemia, M. J.; Park, M.; Kaplan, D. A.; Venot, A.; Boons, G. J.; Li, L.; Linhardt, R. J.; Amster, I. J., High-field asymmetric-waveform ion mobility spectrometry and electron detachment dissociation of isobaric mixtures of glycosaminoglycans. *J Am Soc Mass Spectrom* **2014,** *25* (2), 258-68.
149. Leach, F. E.; Riley, N. M.; Westphall, M. S.; Coon, J. J.; Amster, I. J., Negative Electron Transfer Dissociation Sequencing of Increasingly Sulfated Glycosaminoglycan Oligosaccharides on an Orbitrap Mass Spectrometer. *Journal of The American Society for Mass Spectrometry* **2017,** *28* (9), 1844-1854.
150. Wolff, J. J.; Leach, F. E., III; Laremore, T. N.; Kaplan, D. A.; Easterling, M. L.; Linhardt, R. J.; Amster, I. J., Negative Electron Transfer Dissociation of Glycosaminoglycans. *Analytical Chemistry* **2010,** *82* (9), 3460-3466.
151. Stickney, M.; Sanderson, P.; Leach, F. E.; Zhang, F.; Linhardt, R. J.; Amster, I. J., Online capillary zone electrophoresis negative electron transfer dissociation tandem mass spectrometry of glycosaminoglycan mixtures. *International Journal of Mass Spectrometry* **2019,** *445*, 116209.
152. Racaud, A.; Antoine, R.; Dugourd, P.; Lemoineb, J., Photoinduced dissociation of heparin-derived oligosaccharides controlled by charge location. *Journal of the American Society for Mass Spectrometry* **2010,** *21* (12), 2077-2084.
153. Klein, D. R.; Leach, F. E.; Amster, I. J.; Brodbelt, J. S., Structural Characterization of Glycosaminoglycan Carbohydrates Using Ultraviolet Photodissociation. *Analytical Chemistry* **2019,** *91* (9), 6019-6026.
154. Schindler, B.; Renois-Predelus, G.; Bagdadi, N.; Melizi, S.; Barnes, L.; Chambert, S.; Allouche, A.-R.; Compagnon, I., MS/IR, a new MS-based hyphenated method for analysis of hexuronic acid epimers in glycosaminoglycans. *Glycoconj. J.* **2017,** *34* (3), 421-425.
155. Schindler, B.; Barnes, L.; Gray, C. J.; Chambert, S.; Flitsch, S. L.; Oomens, J.; Daniel, R.; Allouche, A. R.; Compagnon, I., IRMPD Spectroscopy Sheds New (Infrared) Light on the Sulfate Pattern of Carbohydrates. *J. Phys. Chem. A* **2017,** *121* (10), 2114-2120.
156. Schindler, B.; Renois-Predelus, G.; Bagdadi, N.; Melizi, S.; Barnes, L.; Chambert, S.; Allouche, A.-R.; Compagnon, I., MS/IR, a new MS-based hyphenated method for analysis of hexuronic acid epimers in glycosaminoglycans. *Glycoconjugate Journal* **2017,** *34* (3), 421-425.
157. Renois-Predelus, G.; Schindler, B.; Compagnon, I., Analysis of Sulfate Patterns in Glycosaminoglycan Oligosaccharides by MSn Coupled to Infrared Ion Spectroscopy: the Case of GalNAc4S and GalNAc6S. *Journal of the American Society for Mass Spectrometry* **2018,** *29* (6), 1242-1249.

158. Khanal, N.; Masellis, C.; Kamrath, M. Z.; Clemmer, D. E.; Rizzo, T. R., Glycosaminoglycan Analysis by Cryogenic Messenger-Tagging IR Spectroscopy Combined with IMS-MS. *Anal. Chem.* **2017,** *89* (14), 7601-7606.
159. Lettow, M.; Greis, K.; Grabarics, M.; Horlebein, J.; Miller, R. L.; Meijer, G.; von Helden, G.; Pagel, K., Chondroitin Sulfate Disaccharides in the Gas Phase: Differentiation and Conformational Constraints. *J. Phys. Chem. A* **2021,** *125* (20), 4373-4379.
160. Lettow, M.; Grabarics, M.; Mucha, E.; Thomas, D. A.; Polewski, Ł.; Freyse, J.; Rademann, J.; Meijer, G.; von Helden, G.; Pagel, K., IR action spectroscopy of glycosaminoglycan oligosaccharides. *Anal. Bioanal. Chem.* **2020,** *412* (3), 533-537.
161. Lettow, M.; Grabarics, M.; Greis, K.; Mucha, E.; Thomas, D. A.; Chopra, P.; Boons, G.-J.; Karlsson, R.; Turnbull, J. E.; Meijer, G.; Miller, R. L.; von Helden, G.; Pagel, K., Cryogenic Infrared Spectroscopy Reveals Structural Modularity in the Vibrational Fingerprints of Heparan Sulfate Diastereomers. *Anal. Chem.* **2020,** *92* (15), 10228-10232.
162. Allen, S. J.; Giles, K.; Gilbert, T.; Bush, M. F., Ion mobility mass spectrometry of peptide, protein, and protein complex ions using a radio-frequency confining drift cell. *Analyst* **2016,** *141* (3), 884-891.
163. Pagel, K.; Harvey, D. J., Ion Mobility–Mass Spectrometry of Complex Carbohydrates: Collision Cross Sections of Sodiated N-linked Glycans. *Analytical Chemistry* **2013,** *85* (10), 5138-5145.
164. Haack, A.; Crouse, J.; Schlüter, F.-J.; Benter, T.; Hopkins, W. S., A First Principle Model of Differential Ion Mobility: the Effect of Ion-Solvent Clustering. *Journal of the American Society for Mass Spectrometry* **2019,** *30* (12), 2711-2725.
165. Haack, A.; Hopkins, W. S., Kinetics in DMS: Modeling Clustering and Declustering Reactions. *Journal of the American Society for Mass Spectrometry* **2022,** *33* (12), 2250-2262.
166. Götze, M.; Polewski, L.; Bechtella, L.; Pagel, K., A 3D-Printed Offline Nano-ESI Source for Bruker MS Instruments. *Journal of the American Society for Mass Spectrometry* **2023,** *34* (10), 2403-2406.
167. Warnke, S.; von Helden, G.; Pagel, K., Analyzing the higher order structure of proteins with conformer-selective ultraviolet photodissociation. *PROTEOMICS* **2015,** *15* (16), 2804-2812.
168. Wieland, S.; Sandy, G.; Heinz, J.; Alexander, P.; Gert von, H.; Hans, P. B.; Alan, M. M. T. In *The new IR and THz FEL facility at the Fritz Haber Institute in Berlin*, Proc.SPIE, 2015; p 95121L.
169. Szomolanyi, P.; Frenzel, T.; Noebauer-Huhmann, I. M.; Rohrer, M.; Trattnig, S.; Pietsch, H.; Endrikat, J., Impact of concentration and dilution of three macrocyclic gadolinium-based contrast agents on MRI signal intensity at 1.5T and 3T and different pulse sequences: results of a phantom study in human plasma. *Acta Radiologica* **2021,** *62* (1), 51-57.
170. Blumfield, E.; Swenson, D. W.; Iyer, R. S.; Stanescu, A. L., Gadolinium-based contrast agents — review of recent literature on magnetic resonance imaging signal intensity changes and tissue deposits, with emphasis on pediatric patients. *Pediatric Radiology* **2019,** *49* (4), 448-457.
171. Bussi, S.; Coppo, A.; Celeste, R.; Fanizzi, A.; Fringuello Mingo, A.; Ferraris, A.; Botteron, C.; Kirchin, M. A.; Tedoldi, F.; Maisano, F., Macrocyclic MR contrast agents: evaluation of multiple-organ gadolinium retention in healthy rats. *Insights into Imaging* **2020,** *11* (1), 11.

172. Robert, P.; Violas, X.; Grand, S.; Lehericy, S.; Idée, J.-M.; Ballet, S.; Corot, C., Linear Gadolinium-Based Contrast Agents Are Associated With Brain Gadolinium Retention in Healthy Rats. *Investigative Radiology* **2016,** *51* (2), 73-82.
173. Radbruch, A.; Weberling, L. D.; Kieslich, P. J.; Eidel, O.; Burth, S.; Kickingereder, P.; Heiland, S.; Wick, W.; Schlemmer, H.-P.; Bendszus, M., Gadolinium Retention in the Dentate Nucleus and Globus Pallidus Is Dependent on the Class of Contrast Agent. *Radiology* **2015,** *275* (3), 783-791.
174. Ryu, Y. J.; Choi, Y. H.; Cheon, J.-E.; Lee, W.-J.; Park, S.; Park, J. E.; Kim, W. S.; Kim, I.-O., Pediatric Brain: Gadolinium Deposition in Dentate Nucleus and Globus Pallidus on Unenhanced T1-Weighted Images Is Dependent on the Type of Contrast Agent. *Investigative Radiology* **2018,** *53* (4).
175. Sherry, A. D.; Caravan, P.; Lenkinski, R. E., Primer on gadolinium chemistry. *Journal of Magnetic Resonance Imaging* **2009,** *30* (6), 1240-1248.
176. Zou, Z.; Zhang, H. L.; Roditi, G. H.; Leiner, T.; Kucharczyk, W.; Prince, M. R., Nephrogenic Systemic Fibrosis: Review of 370 Biopsy-Confirmed Cases. *JACC: Cardiovascular Imaging* **2011,** *4* (11), 1206-1216.
177. McDonald, R. J.; Weinreb, J. C.; Davenport, M. S., Symptoms Associated with Gadolinium Exposure (SAGE): A Suggested Term. *Radiology* **2021,** *302* (2), 270-273.
178. Aime, S.; Caravan, P., Biodistribution of gadolinium-based contrast agents, including gadolinium deposition. *Journal of Magnetic Resonance Imaging* **2009,** *30* (6), 1259-1267.
179. Boyken, J.; Frenzel, T.; Lohrke, J.; Jost, G.; Pietsch, H., Gadolinium Accumulation in the Deep Cerebellar Nuclei and Globus Pallidus After Exposure to Linear but Not Macrocyclic Gadolinium-Based Contrast Agents in a Retrospective Pig Study With High Similarity to Clinical Conditions. *Invest Radiol* **2018,** *53* (5), 278-285.
180. Laurent, S.; Elst, L. V.; Copoix, F.; Muller, R. N., Stability of MRI paramagnetic contrast media: a proton relaxometric protocol for transmetallation assessment. *Invest Radiol* **2001,** *36* (2), 115-22.
181. Rabiet, M.; Letouzet, M.; Hassanzadeh, S.; Simon, S., Transmetallation of Gd-DTPA by Fe3+, Cu2+ and Zn2+ in water: Batch experiments and coagulation–flocculation simulations. *Chemosphere* **2014,** *95*, 639-642.
182. Taupitz, M.; Stolzenburg, N.; Ebert, M.; Schnorr, J.; Hauptmann, R.; Kratz, H.; Hamm, B.; Wagner, S., Gadolinium-containing magnetic resonance contrast media: investigation on the possible transchelation of Gd3+ to the glycosaminoglycan heparin. *Contrast Media & Molecular Imaging* **2013,** *8* (2), 108-116.
183. Werner, P.; Taupitz, M.; Schröder, L.; Schuenke, P., An NMR relaxometry approach for quantitative investigation of the transchelation of gadolinium ions from GBCAs to a competing macromolecular chelator. *Scientific Reports* **2021,** *11* (1), 21731.
184. Pomin, V. H.; Mulloy, B., Glycosaminoglycans and Proteoglycans. *Pharmaceuticals* **2018,** *11* (1), 27.
185. Chevalier, F.; Angulo, J.; Lucas, R.; Nieto, Pedro M.; Martín-Lomas, M., The Heparin−Ca2+ Interaction: Structure of the Ca2+ Binding Site. *European Journal of Organic Chemistry* **2002,** *2002* (14), 2367-2376.
186. Remko, M.; Van Duijnen, P. T.; Broer, R., Effect of metal ions (Li+, Na+, K+, Mg2+ and Ca2+) and water on the conformational changes of glycosidic bonds in heparin oligosaccharides. *RSC Advances* **2013,** *3* (25), 9843-9853.

187. Remko, M.; Broer, R.; Remková, A.; Van Duijnen, P. T., How strong are Ca2+–heparin and Zn2+–heparin interactions? *Chemical Physics Letters* **2015,** *621*, 12-17.
188. Stevic, I.; Parmar, N.; Paredes, N.; Berry, L. R.; Chan, A. K. C., Binding of Heparin to Metals. *Cell Biochemistry and Biophysics* **2011,** *59* (3), 171-178.
189. Ferro, D. R.; Provasoli, A.; Ragazzi, M.; Casu, B.; Torri, G.; Bossennec, V.; Perly, B.; Sinaÿ, P.; Petitou, M.; Choay, J., Conformer populations of l-iduronic acid residues in glycosaminoglycan sequences. *Carbohydrate Research* **1990,** *195* (2), 157-167.
190. Seo, Y.; Schenauer, M. R.; Leary, J. A., Biologically relevant metal-cation binding induces conformational changes in heparin oligosaccharides as measured by ion mobility mass spectrometry. *International Journal of Mass Spectrometry* **2011,** *303* (2), 191-198.
191. Szekeres, G. P.; Krekic, S.; Miller, R. L.; Mero, M.; Pagel, K.; Heiner, Z., The interaction of chondroitin sulfate with a lipid monolayer observed by using nonlinear vibrational spectroscopy. *Physical Chemistry Chemical Physics* **2021,** *23* (23), 13389-13395.
192. Steffan, G.; Wulff, S.; Galla, H.-J., Divalent cation-dependent interaction of sulfated polysaccharides with phosphatidylcholine and mixed phosphatidylcholine/phosphatidylglycerol liposomes. *Chemistry and Physics of Lipids* **1994,** *74* (2), 141-150.
193. Ricard-Blum, S.; Féraud, O.; Lortat-Jacob, H.; Rencurosi, A.; Fukai, N.; Dkhissi, F.; Vittet, D.; Imberty, A.; Olsen, B. R.; van der Rest, M., Characterization of Endostatin Binding to Heparin and Heparan Sulfate by Surface Plasmon Resonance and Molecular Modeling: ROLE OF DIVALENT CATIONS*. *Journal of Biological Chemistry* **2004,** *279* (4), 2927-2936.
194. Bauer, K. A.; Hawkins, D. W.; Peters, P. C.; Petitou, M.; Herbert, J.-M.; van Boeckel, C. A. A.; Meuleman, D. G., Fondaparinux, a Synthetic Pentasaccharide: The First in a New Class of Antithrombotic Agents — The Selective Factor Xa Inhibitors. *Cardiovascular Drug Reviews* **2002,** *20* (1), 37-52.
195. Olson, S. T.; Björk, I.; Sheffer, R.; Craig, P. A.; Shore, J. D.; Choay, J., Role of the antithrombin-binding pentasaccharide in heparin acceleration of antithrombin-proteinase reactions. Resolution of the antithrombin conformational change contribution to heparin rate enhancement. *Journal of Biological Chemistry* **1992,** *267* (18), 12528-12538.
196. McGhee, J. D.; von Hippel, P. H., Theoretical aspects of DNA-protein interactions: Co-operative and non-co-operative binding of large ligands to a one-dimensional homogeneous lattice. *Journal of Molecular Biology* **1974,** *86* (2), 469-489.
197. Dunbar, R. C.; Martens, J.; Berden, G.; Oomens, J., Binding of Divalent Metal Ions with Deprotonated Peptides: Do Gas-Phase Anions Parallel the Condensed Phase? *The Journal of Physical Chemistry A* **2018,** *122* (25), 5589-5596.
198. Corinti, D.; Paciotti, R.; Re, N.; Coletti, C.; Chiavarino, B.; Crestoni, M. E.; Fornarini, S., Binding motifs of cisplatin interaction with simple biomolecules and aminoacid targets probed by IR ion spectroscopy. *Pure and Applied Chemistry* **2020,** *92* (1), 3-13.
199. Polewski, L.; Springer, A.; Pagel, K.; Schalley, C. A., Gas-Phase Structural Analysis of Supramolecular Assemblies. *Accounts of Chemical Research* **2021,** *54* (10), 2445-2456.
200. Dunbar, R. C.; Polfer, N. C.; Oomens, J., Gas-Phase Zwitterion Stabilization by a Metal Dication. *Journal of the American Chemical Society* **2007,** *129* (47), 14562-14563.
201. Kapota, C.; Lemaire, J.; Maître, P.; Ohanessian, G., Vibrational Signature of Charge Solvation vs Salt Bridge Isomers of Sodiated Amino Acids in the Gas Phase. *Journal of the American Chemical Society* **2004,** *126* (6), 1836-1842.

202. Lettow, M.; Grabarics, M.; Mucha, E.; Thomas, D. A.; Polewski, Ł.; Freyse, J.; Rademann, J.; Meijer, G.; von Helden, G.; Pagel, K., IR action spectroscopy of glycosaminoglycan oligosaccharides. *Analytical and Bioanalytical Chemistry* **2020,** *412* (3), 533-537.
203. Lettow, M.; Greis, K.; Grabarics, M.; Horlebein, J.; Miller, R. L.; Meijer, G.; von Helden, G.; Pagel, K., Chondroitin Sulfate Disaccharides in the Gas Phase: Differentiation and Conformational Constraints. *The Journal of Physical Chemistry A* **2021,** *125* (20), 4373-4379.
204. Mazák, K.; Beecher, C. N.; Kraszni, M.; Larive, C. K., The interaction of enoxaparin and fondaparinux with calcium. *Carbohydrate Research* **2014,** *384*, 13-19.
205. Rajamäki, K.; Nordström, T.; Nurmi, K.; Åkerman, K. E. O.; Kovanen, P. T.; Öörni, K.; Eklund, K. K., Extracellular Acidosis Is a Novel Danger Signal Alerting Innate Immunity via the NLRP3 Inflammasome. *Journal of Biological Chemistry* **2013,** *288* (19), 13410-13419.
206. Wang, H.; Bo, K.; Gao, Y.; Zhou, Z.; Xu, L., Prognosis evaluation of chronic inflammatory cardiomyopathy with ring-like late gadolinium enhancement. *ESC Heart Failure* **2023,** *10* (3), 1735-1744.
207. Martinez, R.; Pavon, A.-G.; Arangalage, D.; Colombier, S.; Rotman, S.; Monney, P.; Kirsch, M.; Schwitter, J.; Rutz, T., Prevalence of pericardial late gadolinium enhancement in patients after cardiac surgery: clinical and histological correlation. *European Heart Journal - Cardiovascular Imaging* **2021,** *22* (Supplement_2).
208. Wilson, H.; Norris, M. D.; Frosch, O.; Agarwal, P. P., Late Gadolinium Enhancement after COVID-19 Vaccination. *Radiology: Cardiothoracic Imaging* **2021,** *3* (5), e210199.
209. Bishop, J. R.; Schuksz, M.; Esko, J. D., Heparan sulphate proteoglycans fine-tune mammalian physiology. *Nature* **2007,** *446* (7139), 1030-1037.
210. Couchman, J. R., Transmembrane Signaling Proteoglycans. *Annual Review of Cell and Developmental Biology* **2010,** *26* (1), 89-114.
211. Mencio, C. P.; Hussein, R. K.; Yu, P.; Geller, H. M., The Role of Chondroitin Sulfate Proteoglycans in Nervous System Development. *Journal of Histochemistry & Cytochemistry* **2020,** *69* (1), 61-80.
212. Gandhi, N. S.; Mancera, R. L., The Structure of Glycosaminoglycans and their Interactions with Proteins. *Chemical Biology & Drug Design* **2008,** *72* (6), 455-482.
213. Parish, C. R., The role of heparan sulphate in inflammation. *Nature Reviews Immunology* **2006,** *6* (9), 633-643.
214. Lin, X., Functions of heparan sulfate proteoglycans in cell signaling during development. *Development* **2004,** *131* (24), 6009-6021.
215. Beurskens, D. M. H.; Huckriede, J. P.; Schrijver, R.; Hemker, H. C.; Reutelingsperger, C. P.; Nicolaes, G. A. F., The Anticoagulant and Nonanticoagulant Properties of Heparin. *Thromb Haemost* **2020,** *120* (10), 1371-1383.
216. Patel, V. N.; Pineda, D. L.; Hoffman, M. P., The function of heparan sulfate during branching morphogenesis. *Matrix Biology* **2017,** *57-58*, 311-323.
217. Lindahl, U.; Bäckström, G.; Malmström, A.; Fransson, L.-Å., Biosynthesis of L-iduronic acid in heparin: Epimerization of D-glucuronic acid on the polymer level. *Biochemical and Biophysical Research Communications* **1972,** *46* (2), 985-991.

218. Maddineni, J.; Jeske, W. P.; Iqbal, O.; Hoppensteadt, D. A.; Fareed, J., Differential Digestion of Different LMWHs by Heparinase-I and Heparinase-II: Drug Developmental Implications. *Blood* **2004,** *104* (11), 4084-4084.
219. Gill, V. L.; Aich, U.; Rao, S.; Pohl, C.; Zaia, J., Disaccharide Analysis of Glycosaminoglycans Using Hydrophilic Interaction Chromatography and Mass Spectrometry. *Analytical Chemistry* **2013,** *85* (2), 1138-1145.
220. Yang, B.; Chang, Y.; Weyers, A. M.; Sterner, E.; Linhardt, R. J., Disaccharide analysis of glycosaminoglycan mixtures by ultra-high-performance liquid chromatography–mass spectrometry. *Journal of Chromatography A* **2012,** *1225*, 91-98.
221. Yang, B.; Weyers, A.; Baik, J. Y.; Sterner, E.; Sharfstein, S.; Mousa, S. A.; Zhang, F.; Dordick, J. S.; Linhardt, R. J., Ultra-performance ion-pairing liquid chromatography with on-line electrospray ion trap mass spectrometry for heparin disaccharide analysis. *Analytical Biochemistry* **2011,** *415* (1), 59-66.
222. Deakin, J. A.; Lyon, M., A simplified and sensitive fluorescent method for disaccharide analysis of both heparan sulfate and chondroitin/dermatan sulfates from biological samples. *Glycobiology* **2008,** *18* (6), 483-491.
223. Grabarics, M.; Lettow, M.; Kirk, A. T.; von Helden, G.; Causon, T. J.; Pagel, K., Plate-height model of ion mobility-mass spectrometry. *Analyst* **2020,** *145* (19), 6313-6333.
224. Grabarics, M.; Lettow, M.; Kirk, A. T.; von Helden, G.; Causon, T. J.; Pagel, K., Plate-height model of ion mobility-mass spectrometry: Part 2—Peak-to-peak resolution and peak capacity. *Journal of Separation Science* **2021,** *44* (14), 2798-2813.
225. Warnke, S.; Ben Faleh, A.; Scutelnic, V.; Rizzo, T. R., Separation and Identification of Glycan Anomers Using Ultrahigh-Resolution Ion-Mobility Spectrometry and Cryogenic Ion Spectroscopy. *Journal of The American Society for Mass Spectrometry* **2019,** *30* (11), 2204-2211.
226. Ujma, J.; Ropartz, D.; Giles, K.; Richardson, K.; Langridge, D.; Wildgoose, J.; Green, M.; Pringle, S., Cyclic Ion Mobility Mass Spectrometry Distinguishes Anomers and Open-Ring Forms of Pentasaccharides. *Journal of the American Society for Mass Spectrometry* **2019,** *30* (6), 1028-1037.
227. Kozak, R. P.; Tortosa, C. B.; Fernandes, D. L.; Spencer, D. I. R., Comparison of procainamide and 2-aminobenzamide labeling for profiling and identification of glycans by liquid chromatography with fluorescence detection coupled to electrospray ionization–mass spectrometry. *Analytical Biochemistry* **2015,** *486*, 38-40.
228. Keser, T.; Pavić, T.; Lauc, G.; Gornik, O., Comparison of 2-Aminobenzamide, Procainamide and RapiFluor-MS as Derivatizing Agents for High-Throughput HILIC-UPLC-FLR-MS N-glycan Analysis. *Frontiers in Chemistry* **2018,** *6*.
229. Cengiz, G.; Kerstin, A. K. L.; Karen, H.; Elena, L.-R.; Vladimir, G.; Anne, V.; Sandra, K.; Andreas, Z.; Sara, T.; Alina, N.; Sebastian, M. K. S.; Christian, M. Z.; Kevin, P.; Achim, D. G.; Matthias, O.; Martin, W.; Geraldine, N., Enzymatic modulation of the pulmonary glycocalyx alters susceptibility to <em>Streptococcus pneumoniae</em&gt. *bioRxiv* **2024**, 2024.01.03.573996.
230. McLafferty, F. W., Mass Spectrometric Analysis. Molecular Rearrangements. *Analytical Chemistry* **1959,** *31* (1), 82-87.
231. van Tetering, L.; Spies, S.; Wildeman, Q. D. K.; Houthuijs, K. J.; van Outersterp, R. E.; Martens, J.; Wevers, R. A.; Wishart, D. S.; Berden, G.; Oomens, J., A spectroscopic test

suggests that fragment ion structure annotations in MS/MS libraries are frequently incorrect. *Communications Chemistry* **2024,** *7* (1), 30.
232. Yagüe, J.; Paradela, A.; Ramos, M.; Ogueta, S.; Marina, A.; Barahona, F.; López de Castro, J. A.; Vázquez, J., Peptide Rearrangement during Quadrupole Ion Trap Fragmentation: Added Complexity to MS/MS Spectra. *Analytical Chemistry* **2003,** *75* (6), 1524-1535.
233. Paizs, B.; Suhai, S., Fragmentation pathways of protonated peptides. *Mass Spectrometry Reviews* **2005,** *24* (4), 508-548.
234. Polfer, N. C.; Oomens, J.; Suhai, S.; Paizs, B., Infrared Spectroscopy and Theoretical Studies on Gas-Phase Protonated Leu-enkephalin and Its Fragments: Direct Experimental Evidence for the Mobile Proton. *Journal of the American Chemical Society* **2007,** *129* (18), 5887-5897.
235. Yakubu, R. R.; Nieves, E.; Weiss, L. M., The Methods Employed in Mass Spectrometric Analysis of Posttranslational Modifications (PTMs) and Protein–Protein Interactions (PPIs). In *Advancements of Mass Spectrometry in Biomedical Research*, Woods, A. G.; Darie, C. C., Eds. Springer International Publishing: Cham, 2019; pp 169-198.
236. Aguiar, M.; Haas, W.; Beausoleil, S. A.; Rush, J.; Gygi, S. P., Gas-Phase Rearrangements Do Not Affect Site Localization Reliability in Phosphoproteomics Data Sets. *Journal of Proteome Research* **2010,** *9* (6), 3103-3107.
237. Palumbo, A. M.; Reid, G. E., Evaluation of Gas-Phase Rearrangement and Competing Fragmentation Reactions on Protein Phosphorylation Site Assignment Using Collision Induced Dissociation-MS/MS and MS3. *Analytical Chemistry* **2008,** *80* (24), 9735-9747.
238. Kováčik, V.; Hirsch, J.; Kováč, P.; Heerma, W.; Thomas-Oates, J.; Haverkamp, J., Oligosaccharide characterization using collision-induced dissociation fast atom bombardment mass spectrometry: Evidence for internal monosaccharide residue loss. *Journal of Mass Spectrometry* **1995,** *30* (7), 949-958.
239. Mucha, E.; Lettow, M.; Marianski, M.; Thomas, D. A.; Struwe, W. B.; Harvey, D. J.; Meijer, G.; Seeberger, P. H.; von Helden, G.; Pagel, K., Fucose Migration in Intact Protonated Glycan Ions: A Universal Phenomenon in Mass Spectrometry. *Angewandte Chemie International Edition* **2018,** *57* (25), 7440-7443.
240. Lettow, M.; Mucha, E.; Manz, C.; Thomas, D. A.; Marianski, M.; Meijer, G.; von Helden, G.; Pagel, K., The role of the mobile proton in fucose migration. *Analytical and Bioanalytical Chemistry* **2019,** *411* (19), 4637-4645.
241. Lettow, M.; Greis, K.; Mucha, E.; Lambeth, T. R.; Yaman, M.; Kontodimas, V.; Manz, C.; Hoffmann, W.; Meijer, G.; Julian, R. R.; von Helden, G.; Marianski, M.; Pagel, K., Decoding the Fucose Migration Product during Mass-Spectrometric analysis of Blood Group Epitopes. *Angewandte Chemie International Edition* **2023,** *62* (24), e202302883.
242. Harvey, D. J.; Mattu, T. S.; Wormald, M. R.; Royle, L.; Dwek, R. A.; Rudd, P. M., "Internal Residue Loss": Rearrangements Occurring during the Fragmentation of Carbohydrates Derivatized at the Reducing Terminus. *Analytical Chemistry* **2002,** *74* (4), 734-740.
243. Moge, B.; Schindler, B.; Yeni, O.; Compagnon, I., Fucose Migration Pathways Identified Using Infrared Spectroscopy**. *Angewandte Chemie International Edition* **2023,** *62* (17), e202300538.

244. Wuhrer, M.; Koeleman, C. A. M.; Deelder, A. M., Hexose Rearrangements upon Fragmentation of N-Glycopeptides and Reductively Aminated N-Glycans. *Analytical Chemistry* **2009,** *81* (11), 4422-4432.
245. Ji, Y.; Yang, X.; Ji, Z.; Zhu, L.; Ma, N.; Chen, D.; Jia, X.; Tang, J.; Cao, Y., DFT-Calculated IR Spectrum Amide I, II, and III Band Contributions of N-Methylacetamide Fine Components. *ACS Omega* **2020,** *5* (15), 8572-8578.
246. Schindler, B.; Barnes, L.; Renois, G.; Gray, C.; Chambert, S.; Fort, S.; Flitsch, S.; Loison, C.; Allouche, A.-R.; Compagnon, I., Anomeric memory of the glycosidic bond upon fragmentation and its consequences for carbohydrate sequencing. *Nature Communications* **2017,** *8* (1), 973.
247. Pellegrinelli, R. P.; Yue, L.; Carrascosa, E.; Warnke, S.; Ben Faleh, A.; Rizzo, T. R., How General Is Anomeric Retention during Collision-Induced Dissociation of Glycans? *Journal of the American Chemical Society* **2020,** *142* (13), 5948-5951.
248. Seo, Y.; Lowe, J. M.; Romano, N.; Gagné, M. R., Switching between X-Pyrano-, X-Furano-, and Anhydro-X-pyranoside Synthesis (X = C, N) under Lewis acid Catalyzed Conditions. *Organic Letters* **2021,** *23* (15), 5636-5640.
249. Ko, Y.-C.; Tsai, C.-F.; Wang, C.-C.; Dhurandhare, V. M.; Hu, P.-L.; Su, T.-Y.; Lico, L. S.; Zulueta, M. M. L.; Hung, S.-C., Microwave-Assisted One-Pot Synthesis of 1,6-Anhydrosugars and Orthogonally Protected Thioglycosides. *Journal of the American Chemical Society* **2014,** *136* (41), 14425-14431.
250. Gaussian 16, Revision C.01, M. J. Frisch, G. W. Trucks, H. B. Schlegel, G. E. Scuseria, M. A. Robb, J. R. Cheeseman, G. Scalmani, V. Barone, G. A. Petersson, H. Nakatsuji, X. Li, M. Caricato, A. V. Marenich, J. Bloino, B. G. Janesko, R. Gomperts, B. Mennucci, H. P. Hratchian, J. V. Ortiz, A. F. Izmaylov, J. L. Sonnenberg, D. Williams-Young, F. Ding, F. Lipparini, F. Egidi, J. Goings, B. Peng, A. Petrone, T. Henderson, D. Ranasinghe, V. G. Zakrzewski, J. Gao, N. Rega, G. Zheng, W. Liang, M. Hada, M. Ehara, K. Toyota, R. Fukuda, J. Hasegawa, M. Ishida, T. Nakajima, Y. Honda, O. Kitao, H. Nakai, T. Vreven, K. Throssell, J. A. Montgomery, Jr., J. E. Peralta, F. Ogliaro, M. J. Bearpark, J. J. Heyd, E. N. Brothers, K. N. Kudin, V. N. Staroverov, T. A. Keith, R. Kobayashi, J. Normand, K. Raghavachari, A. P. Rendell, J. C. Burant, S. S. Iyengar, J. Tomasi, M. Cossi, J. M. Millam, M. Klene, C. Adamo, R. Cammi, J. W. Ochterski, R. L. Martin, K. Morokuma, O. Farkas, J. B. Foresman, and D. J. Fox, Gaussian, Inc., Wallingford CT. **2016**.
251. Pracht, P.; Bohle, F.; Grimme, S., Automated Exploration of the Low-energy Chemical Space with Fast Quantum Chemical Methods. *Phys. Chem. Chem. Phys.* **2020,** *22* (14), 7169-7192.
252. Bannwarth, C.; Ehlert, S.; Grimme, S., GFN2-xTB—An Accurate and Broadly Parametrized Self-Consistent Tight-Binding Quantum Chemical Method with Multipole Electrostatics and Density-Dependent Dispersion Contributions. *J. Chem. Theory Comput.* **2019,** *15* (3), 1652-1671.
253. Adamo, C.; Barone, V., Toward reliable density functional methods without adjustable parameters: The PBE0 model. *J. Chem. Phys.* **1999,** *110* (13), 6158-6170.
254. Grimme, S.; Antony, J.; Ehrlich, S.; Krieg, H., A consistent and accurate ab initio parametrization of density functional dispersion correction (DFT-D) for the 94 elements H-Pu. *J. Chem. Phys.* **2010,** *132* (15), 154104.

255. Meier, F.; Beck, S.; Grassl, N.; Lubeck, M.; Park, M. A.; Raether, O.; Mann, M., Parallel Accumulation–Serial Fragmentation (PASEF): Multiplying Sequencing Speed and Sensitivity by Synchronized Scans in a Trapped Ion Mobility Device. *Journal of Proteome Research* **2015,** *14* (12), 5378-5387.
256. Skowronek, P.; Meier, F., High-Throughput Mass Spectrometry-Based Proteomics with dia-PASEF. In *Proteomics in Systems Biology: Methods and Protocols*, Geddes-McAlister, J., Ed. Springer US: New York, NY, 2022; pp 15-27.
257. Bache, N.; Geyer, P. E.; Bekker-Jensen, D. B.; Hoerning, O.; Falkenby, L.; Treit, P. V.; Doll, S.; Paron, I.; Müller, J. B.; Meier, F.; Olsen, J. V.; Vorm, O.; Mann, M., A Novel LC System Embeds Analytes in Pre-formed Gradients for Rapid, Ultra-robust Proteomics*. *Molecular & Cellular Proteomics* **2018,** *17* (11), 2284-2296.
258. Wang, X.-Y.; Chen, C.-J.; He, Y.-H.; Ding, L.-S.; Wu, Y.-F.; Huang, C.-T.; Wu, J.; Ding, R.; Xue, Y.-H.; Lin, Z.-W.; Xu, P.-X.; Wu, Y.-L.; Liu, W.; Li, J.-J.; Chen, S.-M.; Zhao, Y.-F.; Dong, J.-Y.; Zhou, Q.; Gao, X., Isobaric Stable Isotope N-Phosphorylation Labeling (iSIPL) for Ultrasensitive Proteome Quantification. *Angewandte Chemie International Edition* **2023,** *62* (22), e202303656.
259. Baccolini, C.; Arrivault, S., Stable Isotope Labeling and Quantification of Photosynthetic Metabolites. In *Photosynthesis : Methods and Protocols*, Covshoff, S., Ed. Springer US: New York, NY, 2024; pp 439-466.
260. Lee, S.; Hwang, S.; Seo, M.; Shin, K. B.; Kim, K. H.; Park, G. W.; Kim, J. Y.; Yoo, J. S.; No, K. T., BMDMS-NP: A comprehensive ESI-MS/MS spectral library of natural compounds. *Phytochemistry* **2020,** *177*, 112427.
261. Ma, Y.; Kind, T.; Vaniya, A.; Gennity, I.; Fahrmann, J. F.; Fiehn, O., An in silico MS/MS library for automatic annotation of novel FAHFA lipids. *J Cheminform* **2015,** *7*, 53.
262. Chu, P. M.; Guenther, F. R.; Rhoderick, G. C.; Lafferty, W. J., *The NIST Quantitative Infrared Database*. J Res Natl Inst Stand Technol.: 1999.
263. Jin, C.; Patel, A.; Peters, J.; Hodawadekar, S.; Kalyanaraman, R., Quantum Cascade Laser Based Infrared Spectroscopy: A New Paradigm for Protein Secondary Structure Measurement. *Pharmaceutical Research* **2023,** *40* (6), 1507-1517.
264. Xu, D.; Esko, J. D., Demystifying Heparan Sulfate–Protein Interactions. *Annual Review of Biochemistry* **2014,** *83* (Volume 83, 2014), 129-157.
265. Madsen, J. A.; Xu, H.; Robinson, M. R.; Horton, A. P.; Shaw, J. B.; Giles, D. K.; Kaoud, T. S.; Dalby, K. N.; Trent, M. S.; Brodbelt, J. S., High-throughput Database Search and Large-scale Negative Polarity Liquid Chromatography–Tandem Mass Spectrometry with Ultraviolet Photodissociation for Complex Proteomic Samples*. *Molecular & Cellular Proteomics* **2013,** *12* (9), 2604-2614.
266. Riley, N. M.; Rush, M. J.; Rose, C. M.; Richards, A. L.; Kwiecien, N. W.; Bailey, D. J.; Hebert, A. S.; Westphall, M. S.; Coon, J. J., The Negative Mode Proteome with Activated Ion Negative Electron Transfer Dissociation (AI-NETD). *Mol Cell Proteomics* **2015,** *14* (10), 2644-60.

I Acknowledgment

My journey into the field of mass spectrometry started already in 2018. Back then I went through the instrumental analytics course here at the Freie Universität held by Andreas Springer, Kevin Pagel and Andreas Schäfer. Through this course, I was introduced to Jan Wollschläger and Christoph Schalley with whom I then ventured first into Ion mobility spectrometry which shaped me as a scientist quite substantially and for which I'm also very grateful (and also of course for agreeing to act as a second reviewer of this thesis). With the experience gained, I joined the group of Kevin Pagel for an internship, master thesis and then subsequent doctoral dissertation, for which I'm very grateful that he supervised me. Here Christian Manz acted as the first anchor point in the group and as a great coffee mate. I enjoyed my time at the FHI at the beginning of my thesis very much, and for this, I want to thank Carla, Eike, Gergo, Maike, Marko, Kim and Rayoon. The breakout of COVID-19 beginning in 2020 sadly led to a split of the group between FHI and FU and with that also a break-up of the coffee crew, mainly composed of Christian, Rayoon and me. But new group members joined the FU, and the coffee crew extended again! Thanks here goes to Andreas the HPLC expert, Michael the cross-linking expert (a dead field of science), Anna our guinea pig-loving ex-secretary, Leila who I am still not sure what she did exactly before joining the group and Chun-Wei who suspiciously often walks around with Winnie the Pooh clothing. Special thanks also go to Emeline from whom I learned so much about harmonical rural living with Belgium donkeys and cows. In ~~2021~~ 2022 the group finally moved into the new SupraFAB facility (the fourth lab move during my thesis) and with it a couple of new group members joined. My stay at the SupraFAB was very enjoyable, mainly due to my office mates whom I want to thank, my direct neighbour Michael, whose office desk is only marginally cleaner than mine, Wesley whose desk is considerably cleaner than mine, and the Eiglers, Alex and Jan, for whom I've graciously been measuring mass spectra nearly free of charge. I also thank the newer group members Dana, Eunice, Gael, Marc, Nicklas, and Tom who also contributed to the excellent working atmosphere in the group, even though I'm quite disturbed by Gael's tendency to form Human-based dairy products in the lab. Eunice especially contributed to my mental well-being during the last year.

I want to thank the FHI enclave of the Pagel group consisting of Gergo, Jerome and Rakesh who will soonish also transition into full FU members (maybe?). Besides the Pagel group members, I also want to thank the group members of the von Helden group at the FHI, Jan, Katja, and America. They provided access to some of the used instruments and always listened to my complaints when I was there for measurements. Of course, I also want to thank Gert, I always have been a big fan of your humorous comments. My gratitude also extends to Sebastian Kray and Malerz from the MP department of the FHI, who always helped out when I was looking for a specific tool. I also want to thank the DFG who funded my thesis through the CRC 1340 Matrix in Vision. Last but not least I want to thank my family and friends who supported me throughout the thesis, with most of them not even really knowing what I have been doing.